KEMI
Swedish Chemicals Agency

Uptake and biodistribution of nanoparticles

– a review

REPORT 12/16

kemikalieinspektionen.se

KEMI
Swedish Chemicals Agency

The Swedish Chemicals Agency is supervisory authority under the Government. We work in Sweden, the EU and internationally to develop legislation and other incentives to promote good health and improved environment. We monitor compliance of applicable rules on chemical products, pesticides and substances in articles and carry out inspections. We also provide guidance regarding enforcement and inspections to municipalities and county administrative boards. We review and authorise pesticides before they can be used. Our environmental quality objective is A Non-toxic Environment.

ISSN 0284-1185. Article number: 361 217.

Preface

The Swedish Chemicals Agency has been assigned by the Swedish Government to produce a national action plan for a toxic-free everyday environment: Action plan for a toxic-free everyday environment 2011 – 2014 – protect the children better. The work on the action plan has been extended until 2020.

Efforts are now going on in several areas, both in Sweden, within the EU and internationally and often in cooperation with other authorities. Reducing chemical risks in the everyday environment is one step towards attaining the Swedish Parliament´s environment quality objective A Non-Toxic Environment, which is the objective that we are responsible for.

Within the framework of the action plan, the Swedish Chemicals Agency compiles knowledge in our report and PM series elaborated by experienced colleagues, researchers or consultants. In this way, we present new and essential knowledge in publications which can be downloaded from the website www.kemikalieinspektionen.se

This report/PM has been produced within the framework of the government assignment to carry out the strategy on a non-toxic everyday environment and reaching the environmental quality objective A Non-Toxic Environment 2015–2017.

This review addresses what is known about uptake and biodistribution of nanoparticles (NP) with relevance for human exposure. The work was commissioned by the Swedish Chemicals Agency. The report was written by Professor Gunnar Johanson and MSc Ulrika Carlander at the Institute of Environmental Medicine, Karolinska Institutet, Stockholm. From the Swedish Chemicals Agency Lena Hellmér and Lisa Anfalt, have been responsible for the report.

The review is mainly based on original scientific papers and to a small extent on review articles and reports from organizations and institutions. The articles were retrieved by extensive searches in the PubMed and Web of Science databases (final searches 30 June 2016). As the title indicates, the review is limited to NPs, *ie* particles with at least one dimension below 100 nm. In exceptional cases, results with bigger particles were included as they were considered to contribute to the understanding of the behavior of the NPs.

Table of Contents

Abbreviations

AAS	Atomic absorption spectrometry
ALI	Air-liquid interface (cell culture)
ARPE-19	Human retinal pigment epithelial cell line
AUC	Area under the curve
AUMC	Area under the moment curve
BSA	Bovine serum albumin
bw	Body weight
Caco-2	Human epithelial colorectal adenocarcinoma cell line
CHO	Chinese hamster ovary (cells)
Cmax	Maximum concentration (after administration)
CNT	Carbon nanotube
CND	Composite nanodevice
COPD	Chronic obstructive pulmonary disease
CT	Computational tomography
d	Day(s)
D5	Decamethylcyclopentasiloxane
DLS	Dynamic light scattering
DMAB	Didodecyl dimethylammonium bromide
DSPE-PEG	N-(aminopropyl polyethyleneglycol)carbamyl-distearoylphosphatidyl-ethanolamine
EDX	Energy-dispersive X-ray (analysis)
ENM	Engineered nanomaterial
FITC	Fluorescein isothiocyanate
GI	Gastrointestinal (tract)
h	Hour(s)
HDL	High density lipoprotein
HeLa	Henrietta Lacks, a cervix adenocarcinoma immortal cell line
HUVEC	Human umbilical vein endothelial cells
HPLC	High-performance liquid chromatography
ICP-AES	Inductively coupled plasma atomic emission spectroscopy
ICP-MS	Inductively coupled plasma mass spectrometry
ICP-OES	Inductively coupled plasma optical emission spectroscopy
ip	Intraperitoneal(ly)
iv	Intravenous(ly)
it	Intratracheal(ly)
Kp	(Dermal) permeability coefficient
LALN	Lung-associated lymph nodes
Log K	Log octanol:water partition coefficient
MCMC	Markov chain Monte Carlo (simulation)
min	Minute(s)
MMAD	Mass median aerodynamic diameter
MPPD	Multiple path particle dosimetry (model)
MRI	Magnetic resonance imaging
MWCNT	Multi-walled carbon nanotube(s)
NAA	Neutron activation analysis

NP	Nanoparticle
OECD	The Organisation for Economic Co-operation and Development
PBPK	Physiologically-based pharmacokinetic (model)
PEG	Polyethylene glycol
PEGylated	Coated with PEG
PET	Positron emission tomography
PHCA	Polyhexylcyanoacrylate
PIXE	Particle induced X-ray emission (spectroscopy)
PLA	Poly-dl-lactic acid
PLGA	Polylactic glycolic acid
PMA	Phorbol-12-myristate-13-acetate, a phorbol ester, also named 12-O-tetradecanoylphorbol-13-acetate (TPA)
PMMA	Polymethylmethacrylate
PVP	Polyvinylpyrrolidone
QD	Quantum dot
RAW	(or RAW 264.7) macrophage-like, Abelson leukemia virus transformed cell line derived from BALB/c mice mouse macrophages
RBS	Rutherford backscattering
S-D	Sprague-Dawley (rat)
SDS-PAGE	Sodium dodecyl sulfate polyacrylamide gel electroforesis
SEM	Scanning electron microscopy
STIM	Scanning transmission ion microscopy
TEM	Transmission electron microscopy
Tmax	Time to maximum concentration (after administration)
UV	Ultraviolet (light)
UVA	Long-wave ultraviolet (315–400 nm)
UVB	Medium-wave ultraviolet (280-315 nm)
VIS	Visible light
vs	Versus
WK	Human monocytic cell line derived from an acute monocytic leukemia patient
wk	Week(s)

Summary

Nanoparticles (NPs) in the environment may potentially be absorbed by all absorption pathways, including the skin, gastrointestinal (GI) tract and lungs. The skin's outermost layers prevent effective absorption of viruses, fungal spores, bacteria and other harmful substances from the environment and the loss of water from the body. This barrier function makes it difficult for small molecules to diffuse through the skin and for NPs, being considerably larger, it is even more difficult. Experiments have shown that intact NPs can penetrate into epidermis and the smaller the NPs, the longer they penetrate. Significant systemic absorption of intact NPs has not been demonstrated. However, intact NPs penetrate damaged skin with impaired barrier function. Molecules or ions released from degradable NPs (*eg* silver) can also be absorbed through the skin.

The GI tract and lungs are designed (large total surface area, few cell layers separating blood from gut content and air) to efficiently absorb food and oxygen. Meanwhile, the protection against microorganisms also hinders NPs absorption and the uptake of NPs is generally low also via these routes. For example, the oral and inhalation uptake of gold NPs is less than 1% of the dose in animal experiments. Small NPs tend to be taken up to a greater extent than large NPs. Irritated / damaged mucous membrane may result in higher uptake. The uptake of molecules from soluble or degradable NPs (*eg* silver, zinc oxide) can be much higher.

Other routes include direct uptake to the brain via the olfactory bulb. Carbon-13 NP exposure of rats showed that 50% of the inhaled dose was deposited in the nasopharyngeal tract, whereof 20% was translocated to the olfactory bulb. Elevated NP levels were seen also in other parts of the brain.

All organs in the body are supplied with blood via a dense network of capillaries. The capillaries have only a thin layer of cells (endothelium) that separates them from surrounding tissue, this facilitates for oxygen and carbon dioxide as well as other nutrients and waste products to pass easily. Meanwhile, the capillary wall constitutes a barrier for proteins, microorganisms and NPs. The barrier against the NPs is not perfect as the NPs can pass through the capillary wall through small pores (fenestra) and via phagocytosis / exocytosis. Generally speaking, it is more difficult for large NPs to cross the capillary wall and they distribute more slowly to the organs than small NPs. Passage of the blood-brain barrier and uptake in various regions of the brain have been demonstrated for a variety of NP types. The uptake in brain is generally small (≤0.1% of the systemic dose), but may still be of toxicological importance.

It has been shown that the corona, a protein layer rapidly formed around NPs in contact with blood or other body fluids, plays an important role in phagocytosis and membrane passage. Thus, in vitro experiments showed three times higher cellular uptake of "naked" compared with protein-clad NPs. As the corona is formed after the NPs has entered the body and as corona composition changes over time, it is likely that the distribution and excretion of the NPs also change over time. Other examples of dynamic (time-dependent) processes that may affect the biokinetics are formation and disintegration of NP-agglomerates and NP-induced activation and migration of phagocytes.

Non-soluble NPs generally have a low degree of biotransformation, this is reflected by long half-times in many organs. Depending on the NP dose, type, size etc, a short initial half-time in blood is commonly seen, mainly related to organ in organs mediated by phagocytosis. Depending on the shape and size some excretion via urine and bile may occur. Factors that may affect the uptake and biodistribution are thus, *eg* dose, particle size, agglomeration, lipophilicity, charge, corona formation and composition. The quantitative importance of these factors is not well known.

A promising approach to understand and describe the biokinetics of NPs is by so-called physiologically based pharmacokinetic (PBPK) modeling. PBPK models have been successfully applied to a variety of pharmaceutical drugs and industrial chemicals, and models for NPs have been published in recent years. However, many questions about the basic physiological processes (*eg* phagocytosis) and their quantitative impact on NP biokinetics still remain to be answered.

Sammanfattning

Nanopartiklar (NP) i miljön kan potentiellt tas upp i kroppen via alla upptagsvägar inklusive hud, magtarmkanal, lungor. Hudens yttersta skikt, hornlagret (stratum corneum) förhindrar effektivt upptag av virus, svampsporer, bakterier och andra skadliga ämnen från omgivningen och förlust av vatten från kroppen. Det gör att molekyler har svårt att diffundera igenom huden och för NP, som är avsevärt större, är det ännu svårare. Försök har dock visat att intakta NP kan tränga in en liten bit i hornlagret och ju mindre NP desto längre tränger de in. Signifikant systemiskt upptag av intakta NP har inte påvisats. Dock kan intakta NP tränga igenom skadad hud med försämrad barriärfunktion. Molekyler eller joner som frigörs från degraderbara NP (t.ex. silver, zinkoxid) kan också tas upp genom huden.

Magtarmkanalen och lungorna är konstruerade (mycket stor total yta, få cellager mellan blod och tarminnehåll respektive luft) för att effektivt ta upp födoämnen respektive syre. Samtidigt måste kroppen skyddas mot mikroorganismer och detta medför ett visst skydd även mot NP. Generellt sett är upptaget av NP lågt. För exempelvis guld-NP är upptaget lägre än 1 procent av dosen i djurförsök både oralt och via inhalation. Små NP tenderar att tas upp i högre grad än stora NP. Irriterade/skadade slemhinnor kan resultera i högre upptag. Degraderbara NP (t.ex. silver, zinkoxid) kan tas upp i högre omfattning.

Andra exponeringsvägar som studerats är bl.a. upptag direkt till hjärnan via luktbulben. Ett försök med kol-13 NP på råtta visade att 50 procent av den inhalerade dosen deponerades i näsa-svalg och 20 procent av den deponerade dosen translokerades till luktbulben. Förhöjda kol-13-nivåer sågs även i övriga delar av hjärnan förses med blod via ett finmaskigt nätverk av kapillärer. Kapillärerna har endast ett tunt cellager (endotel) som separerar blodet från omgivande vävnad, detta gör att syre, koldioxid och andra näringsämnen/ slaggprodukter lätt passerar. Samtidigt utgör kapillärväggen en barriär mot proteiner, mikroorganismer och NP. Barriären mot NP är inte total, utan NP kan passera genom kapillärväggen via små porer (fenestra) och via fagocytos/ exocytos. Generellt kan sägas att stora NP har svårare att passera kapillärväggen och distribueras därför långsammare till kroppens organ än små NP.

Man har visat att koronan, ett proteinskikt som snabbt bildas runt NP i kontakt med blod eller andra kroppsvätskor, spelar en viktig roll för fagocytos och membranpassage. Sålunda har provrörsförsök visat på tre gånger högre upptag i celler av ”nakna” jämfört med proteinklädda NP. Eftersom koronan bildas efter att NP kommit in i kroppen, och dessutom förändras över tid, är det troligt att distribution och utsöndring också förändras över tid. Andra exempel på dynamiska (tidsberoende) förlopp som kan påverka toxikokinetiken är bildning eller uppluckring av NP-agglomerat samt NP-inducerad aktivering och migrering av fagocyter.

Stabila (ej biodegraderbara) NP uppvisar generellt en låg grad av biotransformation eller metabolism, vilket bl.a. avspeglas som lång halveringstid i många organ. Beroende på dos och NP-typ ses ofta en kort initial halveringstid i blod, detta beror då på upptag i andra organ medierat av fagocytos. Beroende på form och storlek sker en viss utsöndring via urin och galla.

Faktorer som kan påverka upptag och biodistribution är således bl.a. partikelstorlek, agglomerering, lipofilicitet, laddning, koronabildning och sammansättning samt mängd NP (dos). Den kvantitativa betydelsen av dessa faktorer för upptagets storlek är ej klarlagd.

En lovande ansats för att försöka förstå och beskriva toxikokinetiken av NP går via s.k. fysiologiskt baserad farmakokinetisk (PBPK) modellering. PBPK-modeller har framgångsrikt använts för en rad läkemedel och industrikemikalier och ett flertal modeller för NP har publicerats under de senaste åren. Dock återstår flera frågetecken kring basala fysiologiska processer (t.ex. fagocytos) och hur dessa kvantitativt inverkar på NP-toxikokinetik.

1 Introduction

According to the EU recommendation (Commission 2011) a nanomaterial is:

> " A natural, incidental or manufactured material containing particles, in an unbound state or as an aggregate or as an agglomerate and where, for 50 % or more of the particles in the number size distribution, one or more external dimensions is in the size range 1 nm - 100 nm.
>
> In specific cases and where warranted by concerns for the environment, health, safety or competitiveness the number size distribution threshold of 50 % may be replaced by a threshold between 1 and 50 %.
>
> By derogation from the above, fullerenes, graphene flakes and single wall carbon nanotubes with one or more external dimensions below 1 nm should be considered as nanomaterials. "

Engineered (man-made) nanomaterials (ENM, see page 4 for list of abbreviations) are increasingly used, or projected for use, in society, including industry, medicine, construction and consumer products. This results in new or increased exposure of humans as well as the environment. Humans may be deliberately exposed to ENMs by applying sunscreen formulations on skin, or by receiving nanomaterial-based drug treatment. They may also be unintentionally exposed to ENMs, either directly, for example during the manufacturing process, or indirectly via the environment, for example from material aging or waste. A third exposure category is that of naturally or unintentionally formed nanomaterials such as nanoparticles (NPs) formed during combustion, *eg* fullerenes and carbon nanotubes (CNTs) in candle flames and NPs in engine exhaust (often called ultrafine particles).

The most prominent environmental exposure of humans is likely via inhalation of airborne NPs. Humans may also be exposed via skin, either from deposition of airborne NPs or from direct skin contact with nanomaterials. An important example of the latter is exposure to titanium dioxide or zinc oxide in sunscreens, where the whole body may be deliberately exposed to comparatively amounts of NPs.

The increased use and exposure to ENMs/NPs causes concern for potential health effects. A particular reason for concern is the nanometer size itself. In general, we know far more about the uptake and biodistribution (biokinetics) and toxicity of smaller molecules ("chemicals") and larger, "classical" particles. Meanwhile, it is well known that NPs have unique physical and chemical properties that may be very different from that of the bulk material.

Obviously, to cause adverse effects, the NPs need to reach to the target of toxic action, be it local (*eg* skin, eyes and respiratory airways) or systemic (deeper tissues). In order to evaluate and predict the target dose for different exposure routes and exposure scenarios, it is essential to understand the biokinetics and how it depends on the NP properties.

This report describes what is known about uptake and biodistribution (biokinetics) of NPs with relevance for human exposure. In exceptional cases, results with bigger particles were included as they were considered to contribute to the understanding of the

NP behavior. The report reviews biokinetic mechanisms such as corona formation and phagocytosis, uptake via different exposure routes, biodistribution, physiologically-based pharmacokinetic (PBPK) models, and factors that influence the biokinetics. The emphasis is on exposure routes.

The biokinetics are likely heavily dependent on NP composition, size, shape and surface charge (zeta potential). It would be a never-ending task to describe these aspects in detail. For these details, the reader is referred to the original papers.

There is no obvious way to group biokinetic studies of NPs as they differ in many aspects (exposure route and duration, NP core composition, surface modification, size and shape, etc). To facilitate reading, the different studies were arranged according to the following hierarchy:

- Exposure route
- NP core composition
- Chronology (year of publication)

NP size is given as a single metric, *ie* average diameter (or width x length) in rounded numbers. For several reasons this metric is by no means exact and can only be used for rough comparisons. Thus, the average size has been reported in different ways (arithmetic mean, geometric mean, median) and sometimes refers to the core and sometimes the entire NP including surface ligands. Further, the average does not reflect the spread in size or the degree of agglomeration. The NP size was measured with different methods in the various studies, these methods give different results.

The NP surface charge is given in qualitative terms (+ or -). Numerical values are often not presented as in the original paper, but rounded-off and/or converted to common units. Many values, for example per cent uptake values, were not reported in the original papers, but were calculated by us from graphs or tables therein.

One aspect that makes comparison and interpretation of biokinetic studies challenging is that a wide variety of methods are used, ranging from indirect whole body imaging by *eg* computational tomography (CT), positron emission tomography (PET) and fluorescence imaging, to direct measurements in tissue samples *eg* by atomic absorption spectrometry (AAS) and inductively coupled plasma mass spectrometry (ICP-MS). Each one of these methods has its advantages and limitations in terms of temporal and spatial resolution, sensitivity (detection limit), specificity, cost, accessibility etc (Rinaldo, Andujar *et al* 2015).

2 Biokinetic mechanisms

2.1 Endocytosis and exocytosis

Endocytosis (cellular uptake) and exocytosis (cellular excretion) are complex, inter-dependent processes of vesicular systems that are used to add and remove membrane proteins, to take up and excrete large molecules, to communicate with other cells via hormones and to repair the plasma membrane. In general, foreign material, including NPs, can enter the cell via several mechanisms such as clathrin-, caveolae-, RhoA-,

CDC42-, ARF6-, or flotillin-mediated endocytosis. Some of the endocytosed material, situated in early endosomes, is recycled back to the plasma membrane or delivered to the Golgi apparatus. The remaining material moves slowly along microtubules toward the interior and fuses with late endosomes and later by lysosomes. Some of the material may escape from the vesicular systems to the cytosol. Also, some of the lysosomes can undergo exocytosis and release their content (Sakhtianchi, Minchin *et al* 2013).

Theoretical and experimental studies show that the optimum size for endocytosis of NPs is 40-60 nm. However, several other factors may affect the uptake and excretion, such as membrane-NP binding energy, protein or ligand density (*ie* corona) on the NP surface, and NP curvature (Sakhtianchi, Minchin *et al* 2013).

To illustrate how these principles apply to NPs, select NP cellular uptake and excretion studies are presented in the following.

The cellular uptake processes of polylactic glycolic acid (PLGA) NPs (97 nm) was studied using human arterial vascular smooth muscle cells (VSMCs) with bovine serum albumin (BSA) as model protein and 6-coumarin as fluorescent marker. Endocytosis, exocytosis and retention were studied qualitatively by confocal microscopy and high-performance liquid chromatography (HPLC). The NPs were rapidly internalized and seen inside the cells within 1 min after incubation. Internalization continued over several hours and levelled off after about 4 h, suggesting that equilibrium between endocytosis and exocytosis had been reached. With NPs present in the medium, the uptake increased over time, however, when extracellular NPs were removed, about 65% of the internalized fraction underwent exocytosis in 30 min. The exocytosis was reduced after the treatment with sodium azide and deoxyglucose, suggesting that exocytosis of NPs is energy-dependent. The exocytosis was almost completely inhibited when the medium was depleted of serum, however, addition of BSA in the serum free medium induced exocytosis of NPs (Panyam and Labhasetwar 2003).

Chithrani and colleagues tudied the intracellular uptake of colloidal gold NPs of different sizes and shapes. The uptake half-times of approximately 2 h were very similar between sizes, whereas the maximum uptake was clearly size-dependent with an optimum at 50 nm (14 nm 3000, 30 nm 4200, 50 nm 6200, 74 nm 4000, 100 nm 1700 NPs per cell) (Chithrani, Ghazani *et al* 2006).

Chithrani *et al* also investigated the effect of NP shape (spherical 14 and 50 nm, rod-shaped 20x30, 14x50 and 7x42 nm) on endocytosis and exocytosis rates of transferrin-coated gold NPs in HeLa (ovarian cancer cells), SNB 19 (brain tumor cells) and STO (fibroblasts) cell lines. In HeLa and SNB 19 cells, the fraction of released rod-shaped NPs was much higher than that of spherical-shaped NPs, with no such difference in STO cells. The differences in exocytosis pattern between cell lines can be explained by the cell type (Chithrani and Chan 2007).

Cationic monodisperse fluorescein isothiocyanate (FITC)-labeled polyethylene glycol (PEG) micro- and nanoparticles (100 nm – 5 μm) with different shapes (cubic, cylindrical) were fabricated and their internalization in HeLa cells was studied by transmission electron microscopy (TEM), confocal laser scanning microscopy and fluorescence flow cytometry. The cells readily internalized these nonspherical particles

by several endocytic mechanisms. The uptake rates were higher, the smaller the particles. The cylindrical particles had higher uptake rates (Gratton, Ropp *et al* 2008).

The uptake of anionic magnetic (citrate chelated maghemite, γ-Fe2O3, 7.5 nm) NPs by WK monocytes and derived macrophages was investigated by electron microscopy and quantitated as a function of incubation time and extracellular iron. A two-step binding internalization model allowed estimation of affinity, maximum adsorbed mass, and internalization time constant and capacity. Similar to the study by Wilhelm *et al* (Wilhelm, Gazeau *et al* 2002), the adsorption was comparable for monocytes and macrophages, whereas the latter had more than ten times higher endocytic activity (Luciani, Gazeau *et al* 2009).

The internalization 13-nm silica-coated fluorescent (CdSe-CdS) NPs in human lung carcinoma (A549) cells was studied using fluorescence microscopy after coating with different proteins. The uptake of NPs continued during the 9 h of observation and was approximately 3-fold higher from a protein-free medium, compared to a complete medium including serum. The exocytic process was slower than the uptake and did not near completion within 24 h (Stayton, Winiarz *et al* 2009).

The uptake of positively and negatively charged fluorescein-labeled (2 nm gold core, 6 nm overall with ligand) and doxorubicin-conjugated gold NPs carrying either fluorescein or doxorubicin molecules was studied in vitro in a three-dimensional tumor model. Fluorescence microscopy and mathematical modelling showed that uptake, not diffusion, is the dominant mechanism in particle delivery to the cells and that positive NPs are taken up to a greater extent by proliferating cells. On the other hand, negative gold NPs, which diffused slightly faster when studied in a cell-free gel (Kim, Han *et al* 2010).

The endocytosis and exocytosis of positively charged FITC-labeled maltodextrin NPs (60 nm) in human bronchial epithelial cell line (16HBE14o-) was studied by fluorescence confocal microscopy. The NPs were rapidly endocytosed after as little as 3 min of incubation, and endocytosis appeared faster than binding since most of the NPs were found in the middle of the cells around the nuclei. No further increase was observed after 40 min, probably due to equilibrium between endocytosis and exocytosis. The endocytosis was dramatically reduced at 4°C compared to 37°C and by sodium azide treatment, suggesting an energy dependent process. Protamine pretreatment of the cells inhibited NP uptake suggesting that the NPs are endocytosed via the clathrin pathway. Cholesterol depletion caused a 3-fold increase in NP uptake blocking of exocytosis (Dombu, Kroubi *et al* 2010).

The cellular uptake during 1 h of differently sized polyvinylpyrrolidone (PVP) coated iron oxide NPs (core sizes 8, 23, 37 and 65 nm, corresponding hydrodynamic diameter 32, 71 102 and 118 nm) was studied in vitro using RAW mouse macrophages. Iron in cells was measured by inductively coupled plasma atomic emission spectroscopy (ICP-AES) after nitric acid dissolution. The 37-nm NPs hade the highest cellular uptake (expressed as amount of iron) which was 1.3, 2.8 and 5.3 times higher than the uptake the 65-nm, 23-nm and 8- nm NPs, respectively (Huang, Bu *et al* 2010).

The uptake and intracellular transport of D-penicillamine coated 4-nm quantum dots (CDSe-ZnS) by HeLa cells was investigated live by spinning disk confocal laser microscopy. A large proportion of QDs accumulated at the plasma membrane prior to internalization. By using specific inhibitors it was shown that the QDs were predominantly internalized via clathrin-mediated endocytosis and to smaller extent by micropinocytosis. Further, the uptake efficiency scaled nonlinearly with the NP concentration. Both observations indicate that a critical threshold density has to be exceeded for triggering the internalization process Clusters of QDs were found in endosomes, which were actively transported along microtubules toward the perinuclear region. A significant fraction of endocytosed QDs were found in lysosomes, while others were actively transported to the cell periphery and excreted with a half-time of 21 min (Jiang, Rocker *et al* 2010).

The endocytosis, exocytosis and breakdown of non-coated (hydrodynamic diameter 16 nm), PEG-coated (23 nm) and BSA-coated (35 nm) polyacrylic acid QDs (ZnS-capped CdSe, core size 5 nm) was studied using rat liver Kupffer cells and fluorescence imaging. The uptake was fitted to a sigmoidal curve, reflecting a two-stage phagocytosis process of initial membrane receptor binding followed by internalization. PEG-coated QDs had the lowest and BSA-coated the highest uptake. About one third of the uncoated and BSA-coated QDs were excreted after 6 h of incubation in QD-free media. In contrast, no exocytosis of PEG-coated QDs was observed. After 6 h, 0.15% (non-coated), 0.05% (PEG-coated) and 0.5% (BSA-coated) of the maximum QD cadmium content in cells was found as Cd2+ in the medium, suggesting slight breakdown (Fischer, Hauck *et al* 2010).

The effect of serum proteins on the uptake of negatively charged red fluorescent polystyrene NPs (49 nm and 100 nm) in porcine aortic endothelial cells was studied by TEM, confocal fluorescence microscopy and multiple particle tracking. The NPs were rapidly internalized by cells in serum-free medium, but much slower in 10% fetal bovine serum-enriched medium. The authors concluded that unspecific protein adsorption on NP surface can affect the internalization kinetics, but it is not effective in controlling active and cellular-mediated uptake mechanisms of NPs and their intracellular routes (Guarnieri, Guaccio *et al* 2011).

A range of fluorescent carboxyl-modified polystyrene NPs (40, 100, 200, and 500 nm, 1 and 2 μm) were incubated with a series of cell types (HeLa and A549 epithelial cells, 1321N1 astrocytes, HCMEC D3 endothelial cells, RAW 264.7). Confocal microscopy and flow cytometry were used to study particle uptake and subcellular localization. The internalization was highly size-dependent for all studied cell lines, the smaller the NP, the higher the uptake. Further, the uptake kinetics for the same type of NP varied between cell types. Cells not specialized for phagocytosis were also able to internalize the larger NPs. Intracellular uptake of all sizes of particles was highest in the RAW 264.7 cells (a specialized phagocytic cell line) and the lowest in the HeLa cells. The authors concluded that NP uptake might not follow commonly defined size limits for uptake processes (dos Santos, Varela *et al* 2011).

The cellular uptake of a series of quaternary ammonium salt didodecyl dimethylammonium bromide (DMAB) -modified PLGA NPs (50-300 nm) by human

epithelial colorectal adenocarcinoma cells (Caco-2) and human colon adenocarcinoma cells (HT-29) was investigated by confocal laser scanning microscopy. The surface modification with DMAB notably improved the cellular uptake. The uptake had an optimum particle size of 100 nm (Xu, Yao *et al* 2012).

The exocytosis profile of two types of peptide-coated gold NPs with similar charge and size (15 nm) but different functionality was studied using human umbilical vein endothelial cells (HUVEC) grown in a monolayer. Analysis by ICP-AES showed that about 40% of the NPs were excreted after 6 h. However, while one kind of NPs appeared to progressively exocytose, the other one had a profile suggesting that some of the particles were taken up de novo (Bartczak, Nitti *et al* 2012).

Yu *et al* (Yu, Lau *et al* 2012) studied the influence of NP size and charge on uptake by WK monocytes using a variety of PEGylated polypropylene sulfide-coated iron oxide micelles (30 to 100 nm, -23 to +9 mV) and magnetic resonance imaging (MRI). NP size and charge both contributed towards non-specific uptake, with size being the more important factor (Yu, Lau *et al* 2012).

The uptake by SWCNTs (1.0 x 145 nm) dispersed with BSA by NIH-3T3 cells was studied as functions of concentration of (1-100 μg/ml) and time (seconds-days) by determining the mass of SWCNTs per cell with Raman spectroscopy. The rate of cellular uptake was rapid, reaching steady state within approximately 1 min. At concentrations above 1 μg/ml the internalization was saturated. The cells recovered from the SWCNTs over approximately 30 h, regardless of dosage level and exposure duration (Holt, Dahl *et al* 2012).

Different cell types (human Saos-2 osteoblasts, murine MC3T3-E1 preosteoblasts, murine L929 fibroblasts and murine RAW-264.7 macrophages) were incubated with 75 μg/ml of PEG-FITC-coated graphene oxide 100-nm nanosheets. The uptake kinetics, analyzed by fluorescence flow cytometry, revealed differences in uptake depending on cell type, with higher and faster uptake by osteoblast-like cells. The PEG structure (number of branches) also influenced the cellular uptake (Vila, Portoles *et al* 2012).

Endocytosis, intracellular trafficking, exocytosis and transcytosis of PLGA NPs (80 nm) were studied in intestinal epithelial Caco-2 cells. The transport processes were characterized as being governd by nonspecific nano-bio interactions. The clathrin-dependent pathway, lipid raft/caveolae and macropinocytosis as well as co-involvement of different proteins like actins, protein tyrosine kinase and cyclooxygenase (COX) were involved in the endocytosis. Both ER/Golgi and Golgi/REC/plasma membrane pathways were involved in the exocytosis. The transcytosis across the cell monolayer was low (<5%). The consistency between surface binding and internalization at the two temperatures studied (both were considerably higher at 37°C than at 4°C), suggests that cell binding was the precondition and key step for endocytosis. The involvement of both energy dependent and independent mechanisms was observed in the endocytosis, exocytosis and transcytosis processes (He, Lin *et al* 2013).

A co-culture of epithelial human epithelial (NCI-H441) and endothelial (ISO-HAS1) cell lines (an in vitro model of the alveolar barrier) was used to evaluate the effects and uptake of amorphous silicon dioxide NPs (unlabeled 15, 35 and 80 nm, and fluorescent

80 nm, the latter used for NP uptake measurements), in the presence or absence of WK monocytes. NP exposure induced an inflammatory response and oxidative stress resulting in damage of the "alveolar barrier" as measured by trans-epithelial resistance (TEER) and increased uptake of the 80-nm NPs. When measured in monocultures, the NP uptake was high in PMA-activated monocytes and in endothelial cells (560 and 510 pg/cell, respectively, after 24 h), and low in non-activated monocytes and in epithelial cells (Farcal, Uboldi *et al* 2013).

The uptake kinetics and intracellular localization of carboxyl-coated QDs (CdSe/ZnS, core 5.2 nm, hydrodynamic radius 13–18 nm) in different cells (NIH3T3, MCF-7, HepG2) was analyzed by confocal and steady-state fluorescence spectroscopy. The uptake of was dramatically reduced at 4°C compared to 37°C, indicating energy-dependence. Four morphological phases were identified: (1) adherence to the cell membrane, (2) formation of granulated clusters throughout the cytoplasm; (3) granulated clusters in the perinuclear region; and (4) formation and redistribution of multivesicular body-like structures in the cytoplasm. The cellular distribution contrasted that seen with microinjected QDs which remained uniformly distributed in the cytosol for at least 24 h. The authors concluded that the findings support that QDs are taken up by endocytosis (Damalakiene, Karabanovas *et al* 2013).

The endocytosis and exocytosis of titanium dioxide NPs in neural stem cells was investigated by ICP-AES and confocal microscopy. Irrespective of the type (30 nm, 50 nm, 100x4-6 nm) and dose, approximately 30% of the total applied dose was taken up by cells 48 h. When changing to NP-free medium, about 40% of the intracellular NPs was excreted in 24 h. Exocytosis did not occur during cell division. The results suggested that both endocytosis and exocytosis were energy-dependent processes, and that the NP uptake was influenced by serum proteins (Wang, Wu *et al* 2013).

Methoxy-polyethylene glycol -b-polycaprolactone NPs with and without folate-functionalization were synthesized at sizes ranging from 50 to 250 nm. Uptake studies with ARPE-19 cells (a human retinal pigment epithelial cell line) showed that NPs with 100% folate loading had the highest binding affinity and uptake rate. The maximum uptake rate increased as the size decreased from 250 to 50 nm. By use of clathrin-(chlorpromazine) and caveolae (methyl-beta-cyclodextran) mediated endocytosis inhibitors, revealed that the uptake of the 50-nm NPs was preferentially via clathrin-mediated endocytosis, whereas the uptake the 250-nm NPs was dominated by caveolae-mediated endocytosis (Langston Suen and Chau 2014).

2.2 Phagocytosis models

Wilhelm *et al* followed the uptake of negatively charged super paramagnetic iron oxide NPs (9 nm core) in HeLa cells and mouse RAW macrophages, qualitatively by EM and quantitatively by magnetophoresis and electron spin resonance. A two-step endocytic model was developed based on experimental data at 4°C and 37°C, *ie* binding of anionic magnetic NPs onto the cell surface described as a Langmuir adsorption) followed by saturable cell internalization. Binding (adsorption and desorption rate, density of binding sites) and uptake (internalization rate and capacity) parameters were determined by best fit. The binding and internalization rate parameters were similar for the two cell

types whereas the internalization capacity differed by one order of magnitude, illustrating different cellular functions (Wilhelm, Gazeau *et al* 2002).

In order to estimate the cellular exposure to nickel, Hack *et al* (Hack, Covington *et al* 2007) developed a preliminary model to describe the differences in the extracellular and intracellular kinetics of three different classes of nickel compounds, namely soluble chloride and insoluble sulfide and subsulfide, in tracheobronchial epithelial cells. Literature data were used to define the initial model parameters covering, for nickel ions: maximum cellular influx and efflux rate constant and concentrations at half maximum influx and efflux, intracellular diffusion rates and intracellular maximum binding capacities and binding affinities, and for micro sized nickel sulfide and subsulfide particles: phagocytosis rates and extracellular and vacuolar dissolution rates The model was able to describe experimental kinetic data on the three nickel forms of nickel obtained in cell culture systems (Hack, Covington *et al* 2007).

The binding and internalization of liposomes (phosphatidylcholine vesicles, hydrodynamic diameter 180 nm) loaded with maghemite (γ-Fe2O3), 8 nm) nanocrystals in PC3 human adenocarcinoma prostatic cells line were investigated in vitro. The time course of the rhodamine-labeled liposomes was followed by confocal fluorescence microscopy and that of the iron oxide by magnetophoresis. The uptake kinetics of liposomes could be modeled as a two-step process, *ie* binding adsorption to the outer cell membrane followed by internalization, both processes being saturable (Martina, Wilhelm *et al* 2008).

Jin *et al* (Jin, Heller *et al* 2009) developed a quantitative endocytosis model with a clustering mechanism to account for the energy and enthalpy needed for small NPs to overcome the elastic energy and entropic barriers associated with vesicle formation. The model was developed using experimental data from endocytosis and exocytosis of SWNTs (130-660 nm length) in NIH-3T3 cells measured by single particle tracking of photoluminescence. The model was also tested against published data on gold NPs (14-100 nm). The endocytosis rate constant of SWNTs was nearly 1000 times that of the gold NPs, whereas the exocytosis rate constants were similar in. The total uptake of both types of NP was for a radius of 25 nm (Jin, Heller *et al* 2009).

The uptake of 60 nm (SPIO) and 20 nm (USPIO) super paramagnetic iron oxide NPs (crystalline core of Fe3O4 and y-Fe2O3 covered with carboxydextran) by human macrophages was studied by spectroscopy, TEM and spinning disk confocal microscopy. The principal uptake mechanism for both particles was identified as clathrin-mediated, scavenger receptor A-dependent endocytosis. A mathematical model of the uptake process was developed (Lunov, Zablotskii *et al* 2011).

The uptake kinetics of fluorescent (YG dye) polystyrene NPs (40-50 nm) and free fluorescent dye in A549 cells were studied by flow cytometry. For the NPs, the intracellular concentration increased linearly with time up to 7 h, suggesting that the uptake is essentially irreversible. The following day the increase in fluorescence in cells was sub linear, however, this could be explained by equal sharing of NPs between dividing cells. The flux into cells was proportional to the external concentration up to a concentration of 50 µg/ml but seemed to approach saturation at the highest tested concentration of 90 µg/ml. The authors concluded that the NPs accumulate practically

irreversibly in the lysosomes and that release of dye from the NPs as well as cell division needs to be accounted for in cellular uptake models (Salvati, Åberg *et al* 2011).

The uptake and removal of silicon QDs (3 nm) by HUVEC cells were monitored for 4 h by confocal laser scanning microscope, measuring the fluorescence intensity. Si-QDs were internalized via endocytosis and transported to late endosomes/lysosomes. At all concentrations tested (50, 100, 200 μg/ml), the number of internalized Si-QDs increased with time and gradually reached a plateau value. Similarly, when the cells were washed and exposed to fresh culture medium, the number of internalized QDs decreased with time and gradually reached a plateau. Based on the observed data, a kinetic model based on the mass balance of QDs and receptors in a cell was developed. The model has four rate constants to describe (1) adsorption to and (2) desorption from cell surface, (3) cellular uptake and transport to endosomes, and (4) removal from the cell. In addition, a dissociation constant between receptors and QDs in the endosomes was introduced. According to the model, the latter is a determinant factor for QD accumulation in cells after washing (Ohta, Inasawa *et al* 2012).

The cellular uptake of 25-100% folate functionalized methoxy-poly(ethylene glycol)-b-polycaprolactone (mPEG-b-PCL) and folate-functionalized PEG-b-PCL NPs (50, 120, 250 nm) in ARPE-19 cells was studied by fluorescence microscopy. The binding affinity and maximum uptake rate were evaluated by a 2-step mathematical model to quantify the binding affinity and uptake kinetics. The NPs with 100% folate loading had the highest binding affinity and uptake rate. The maximum uptake rate increased as the NP size decreased from 250 nm to 50 nm. Chlorpromazine and methyl-beta-cyclodextran were used to inhibit clathrin- and caveolae-mediated endocytosis, respectively. The 50 nm NPs were internalized fastest, mainly via clathrin-mediated endocytosis. The uptake of 250 nm NPs was slowest and dominated by caveolae-mediated endocytosis (Langston Suen and Chau 2014).

2.3 Endothelial passage

A major barrier against the redistribution of NPs between blood and surrounding tissue is the endothelium. The blood vessel endothelia are classified as continuous, fenestrated, or discontinuous, depending on the morphology (Michel and Curry 1999; Gentile, Ferrari *et al* 2008; Sarin 2010). The fenestrated endothelium exists in glands, digestive mucosa, and kidneys and has an octagonal symmetry with radial fibrils forming fenestrae of about 60 nm. Discontinuous endothelium with pores of 50-100 nm is typical for the liver, spleen and bone marrow. NPs ≤60 nm may thus more easily penetrate into tissues with fenestrated or discontinuous endothelia (Li, Al-Jamal *et al* 2010). In addition, the phagocytic cells in these organs are located in direct contact with circulating blood, facilitating recognition and uptake of NPs (Moghimi, Hunter *et al* 2001).

The transport and local concentration of NPs in a blood vessel is governed by true convection, radial and longitudinal diffusion in the blood and diffusion/endocytosis into the wall of the vessel, *ie* the endothelium. By describing the longitudinal transport of NP in blood with blood behaving as a Casson fluid (plug flow in the central region, parabolic velocity profile in the outer region), Gentile *et al* (Gentile, Ferrari *et al* 2008)

showed that, theoretically, both the rheology of blood and the permeability of the vessel wall may constitute physiological barriers to the intravascular translocation of NPs.

Kim *et al*, using various lipid-polymer hybrid NPs (1-3 nm gold nanocrystals as kernels) and a variety of imaging methods (TEM, 3D dynamic contrast enhanced MRI, near infrared fluorescent (NIRF) imaging), showed that the NP translocation into the aortic wall was approximately three-fold higher in the aorta wall of atherosclerotic rabbits, compared to healthy rabbits. At the cellular level, the atherosclerotic vessel wall contained a substantial amount of NPs within the atherosclerotic plaque, mainly at the luminal side of the plaque but also near the vasa vasorum (the network of small blood vessels that supply the larger ones). Visualization of gold by TEM at the subcellular level showed NPs in vesicles of macrophages in proximity to endothelial gaps (Kim, Lobatto *et al* 2014).Endothelial passage was studied by Rehberg and coworkers (Rehberg, Nekolla *et al* 2016)who demonstrated that systemically administered carboxyl-modified QDs are rapidly taken up by perivascular macrophages and tissue-resident cells in skeletal muscle of healthy mice. Confocal microscopy revealed presence of microtubules wherein QDs were transported bidirectionally at a velocity of 0.8 μm/s. Expanding this study showed rapid uptake of QDs not only by perivascular macrophages but also by tissue-resident cells localized more than 100 μm from the closest vessel (Rehberg, Nekolla *et al* 2016).

2.4 Protein corona

As with any biomaterial, once in vivo, NPs will interact with surrounding biomolecules forming a so-called protein corona, biocorona, or simply corona. It is the outermost part of the corona, and not the NP itself, that represents interface with the environment. Depending on the surface properties and size of the NP and the composition of the surrounding medium, the corona may profoundly change the surface properties compared to the “naked” NP in terms of *eg* size, surface charge and how it is presented to and recognized by membrane receptors (Fadeel, Feliu *et al* 2013). Thus, the kinetic and equilibrium binding properties depend on protein identity as well as particle surface characteristics and size (Cedervall, Lynch *et al* 2007; Tenzer, Docter *et al* 2011; Tenzer, Docter *et al* 2013).

This can be illustrated by the study of Shim *et al* who analyzed the protein corona by liquid chromatography-tandem mass spectrometry after incubation of four types of silica NPs (20 and 100 nm, positively and negatively charged) with rat plasma. More proteins were found in the corona of small (115 *vs* 50 and 48 *vs* 36 proteins) compared to large and in positive compared to negatively charged (115 *vs* 48 and 50 *vs* 36 proteins). These dependencies on size and charge were less evident for zinc oxide NPs (Shim, Hulme *et al* 2014).

The change in size (and properties) due to corona formation seems to be substantial. Calatayud *et al* (Calatayud, Sanz *et al* 2014) immersed magnetic NPs (magnetite, Fe3O4, cores 25-30 nm) in situ functionalized with positive polyethyleneimine or negative poly(acrylic acid) in cell culture medium with ovalbumin. Iron content was determined by UV-VIS spectrometry after thiocyanate complexation. A 5-fold increase of the hydrodynamic size (measured by dynamic light scattering, DLS) was seen after a

few minutes of incubation and after 24 h large NP-protein aggregates with hydrodynamic sizes of approximately 1500 nm (positive NPs) and 3000 nm (negative NPs) were observed, each one containing 450-1000 magnetic cores. Further, the positive NPs aggregates were incorporated in SH-SY5Y human neuroblasts (measured by magnetic measurements, UV-VIS spectroscopy and ICP-MS) in much larger amounts than the negative ones. There were also notable differences in attachment to the cell membrane, as analyzed by focussed ion beam scanning electron microscopy (SEM) (Calatayud, Sanz *et al* 2014).

The changes in properties may in turn dramatically affect not only the oxidative and inflammatory response but also the biokinetics in terms of endocytic or phagocytic capacity, biodistribution to different organs, excretion etc. Not only does the corona formation alter the properties of the NP but also the function of the proteins (Maiolo, Del Pino *et al* 2015). The adsorption kinetics of proteins forming the corona is highly complex and poorly understood, due to the heterogeneous composition of biological fluids such as plasma. This adsorption occurs, particularly during the initial phases, as a continuous dynamic exchange of proteins between the medium and the NP surface. While first most abundant proteins reach the NP surface and are adsorbed, those are later replaced by less motile proteins with higher binding affinity, forming a so-called "hard corona". However, even the long-lived hard corona evolves and will re-equilibrate as the NP passes from one biological fluid to another, *eg* from plasma to interstitium (Lundqvist, Stigler *et al* 2011). Considering human blood as the medium, serum albumin is first adsorbed to the NP surface and later on replaced by fibrinogen in a dynamic competition reaction [14,15]. The dynamic nature of the adsorption processes makes it difficult to study the corona experimentally, as any change of the medium (*eg* by washing the NPs) will also alter the corona (Pfeiffer, Rehbock *et al* 2014).

Colloidal gold NPs (10 and 15 nm) were modified with amphiphilic polymers to obtain NPs with identical physical properties except for the sign of the charge. The number of adsorbed human serum albumin molecules per NP was not influenced by the surface charge. However, in both serum-free and serum-containing media, NP internalization by cells (3T3 fibroblasts) in vitro was higher for positively than for negatively charged NPs (Huhn, Kantner *et al* 2013).

NP uptake can be described as a two-step process, where the nanoparticles initially adhere to the cell membrane and subsequently are internalized by the cells via energy-dependent pathways. In general, the adsorption of proteins on the NP surface strongly reduces the NP adhesion to membranes and, as a consequence, decreased cellular uptake efficiency (Lesniak, Salvati *et al* 2013). The decreased cellular uptake increases the possibility for translocation to more distant tissues resulting in unexpected biodistribution and accumulation patterns (Kreyling, Fertsch-Gapp *et al* 2014).

The importance of the corona for the biokinetics has not only been demonstrated in vitro, but also in vivo. Thus, Konduru *et al* compared the biokinetics in male Wistar rats of intravenously (*iv*) injected uncoated (29 nm) or silica-coated (28 nm) neutron activated zinc oxide NPs. The rats were sequentially euthanized, and 18 tissues were collected and analyzed for 65Zn radioactivity. The decline in plasma was biphasic for both NP types. However, the half-times of the silica-coated were shorter (initial <1 min,

terminal 2.5 min) compared to the uncoated NPs (1.9 min, 38 min). Moreover, the silica-coated NPs had higher 65Zn activity in red blood cells and higher initial uptake in the liver. However, the 65Zn concentrations were significantly lower in all other tissues compared to dosing with uncoated NPs. Incubation of the two NP types in rat plasma and subsequent analysis by SDS-PAGE gel electrophoresis and mass spectrometry of selected gel bands revealed that the protein corona formed on silica-coated zinc oxide NPs had higher amounts of plasma proteins, in particular albumin, transferrin, A1 inhibitor 3, alpha-2-hs-glycoprotein, apoprotein E and alpha-1 antitrypsin. The authors concluded that surface modification with amorphous silica alters the protein corona, agglomerate size, and zeta potential of the NPs, which in turn influences the biokinetic behavior in the circulation (Konduru, Murdaugh *et al* 2015).

The dynamic nature of corona formation may be of importance in interspecies extrapolation of NP biodistribution. This is illustrated by the pharmacokinetic model developed by Sahneh *et al* (Darabi Sahneh, Scoglio *et al* 2013; Sahneh, Scoglio *et al* 2015). In their hypothetical model, injected NPs are either delivered to target cells or removed from blood by the mononuclear phagocytic system, (previously named reticuloendothelial system or RES). While the NPs are circulating in the blood their corona slowly shifts to a mature, stable, “hard” corona. The stable-corona NPs are delivered to target cells at a lower rate whereas the phagocytic uptake remains high. When the systemic NP half-time is short (such as in rodents compared to humans) there is less time for the stable corona to form. For species with longer half-lives (such as humans), formation of a hard bio¬corona may thus dramatically decrease the intended target delivery ratio (Darabi Sahneh, Scoglio *et al* 2013; Sahneh, Scoglio *et al* 2015).

Fleischer and Payne found that, as serum proteins adsorb onto the surface of positively (zeta potential +20 mV) or negatively (-19 mV) charged NPs polystyrene NPs, similar net anionic protein-NP complexes with similar diameters and effective (-31 mV and -27 mV) surface charges were formed. In contrast, the two NP types showed opposite behavior in terms of cellular binding. Thus, the cellular binding of BSA-NP complexes formed from positive NPs was enhanced, whereas that of complexes formed from negative NPs was inhibited. This contrasting behavior was independent of NP size (40-200 nm) and cell type (monkey kidney epithelial cells (BS-C-1), HeLa cells and CHO cells). Similar results as for negative polystyrene NPs were obtained for anionic QDs and colloidal gold nanospheres (Fleischer and Payne 2014).

3 Dermal exposure

3.1 Potential for dermal exposure

The properties of nano-scale materials have enabled many different applications. Considering consumer exposure, the mark *et al*ready offers many products containing nanomaterials and for most of them the skin is likely to be a potential route of exposure. Powder-based and dusty materials raise concerns mainly for inhalation exposure, whereas for nanomaterials in suspensions, and especially those such as sunscreens) that are intended for dermal application, the dermal exposure route is likely to be of higher concern. Cosmetics in the form of moisturisers, make-up etc. are one of the major applications of nanomaterials. The most commonly used nanomaterials are titanium

dioxide and zinc oxide in sunscreens, since these materials provide effective filters against UV radiation.

However, the potential for skin exposure and uptake does not only apply to nanomaterials in sunscreens and other skin cosmetic products. In a Danish report from 2013, the authors counted more than 400 products containing metal nanomaterials and destined to topical applications for consumers, see examples in Table 1. Consumers can also be exposed to various products not designed for skin application but which use may result in exposure of skin to nanomaterials. For example, silver and other metals are being added into textiles due to properties such as anti-bacterial, water repellent, UV absorption, tear and wear resistance etc., as shown in Table 1. Nanomaterials are also introduced in many other products such as motor oil, fuel catalyst, cleaning products etc. with potential skin exposure of consumers (Poland, Read *et al* 2013).

Table 1. Common nanomaterial, properties and applications with relevance for consumers´skin exposure (from Poland, Read et al 2013).

Nanomaterial	Properties	Examples of applications
Carbon nanofibers, nanotubes, fullerenes	Increased tensile strength High chemical resistance Anti-oxidant Delivery system	Sporting goods Textiles Cosmetics Therapeutics Diagnostics
Carbon black NPs	Improved abrasion resistance and roughness High chemical resistance	Sporting goods Composites Textiles Cosmetics Pigment
Clay NPs	Electrical, heat and chemical resistance Block UV light Flame retardant anticorrosive Absorbing properties	Composites Sunscreens Textiles
Metal NPs (copper, gold, silver)	Antimicrobial Anti-odor Self-sterilisation	Textiles Surface coating Burn dressing Cosmetics Dietary supplement Therapeutics
Metal oxide NPs (aluminum, cerium, magnesium, titanium and zinc oxides)	UV absorption Photo catalytic Photo oxidizing Antimicrobial	Sunscreen Cosmetics Textiles Self-cleaning coating Cleaning products Sporting goods Motor oil Diesel catalyst

3.2 The skin as a barrier

The skin is the largest organ of the human body (15% of total adult body weight). It provides a barrier between the human body and its environment. The major function is to prevent loss of water and heat to the environment. The skin also protects the body from mechanical, biological and chemical hazards. It consists of three layers (from inside to outside): hypodermis, dermis and epidermis. The hypodermis (subcutis) is the deepest part of the skin and contains mainly adipose tissue. The subcutaneous layer is important for protection from mechanical injuries, energy provision, thermoregulation and insulation (Johanson and Rauma 2008).

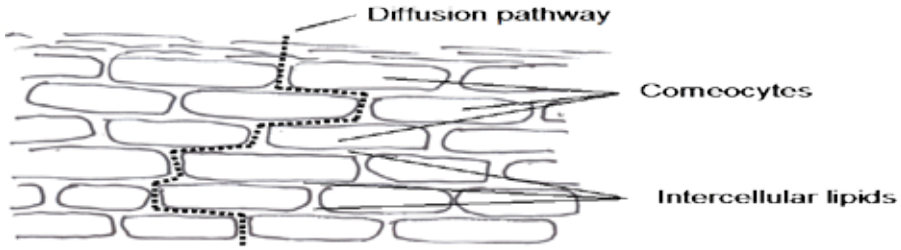

Figure 1. Brick and mortar structure of the stratum corneum showing dense, keratinized corneocytes, intercellular lipid layers and one of the diffusion pathways (from Johanson and Rauma(Johanson and Rauma 2008).

The major diffusion barrier is the stratum corneum, the outermost layer of the epidermis. The stratum corneum mainly consists of several layers of completely keratinized dead cells. The main constituent, keratin, is a tough, insoluble protein that is also the chief structural constituent of hair, nails, and hooves. The keratin is organized together with intercellular lipids in a “brick and mortar” structure (figure1). This makes the skin highly impermeable and at the same time very flexible and elastic. However, the stratum corneum is not entirely impermeable. Thus, water as well as other small molecules diffuses slowly through the skin. Water is very important to maintain the flexibility of the skin. Dry skin becomes rough and flaky and dry stratum corneum is reduced to a very brittle, thin sheet. Water is also important for thermoregulation, as the heat used to evaporate the water excreted via sweat glands lowers the temperature of the skin (Johanson and Rauma 2008).

Overall, as the skin is designed to resist diffusion (*ie* loss of water) it is generally relatively impermeable even to small molecules such as organic solvents with sizes below 1 nm. The permeability for NPs of typically 10-100 nm is obviously expected to be even lower.

However, it should be remembered that several factors may increase the extent of the dermal uptake, including for example: anatomical site (skin thickness), skin humidity, temperature and barrier integrity. The skin integrity may in turn be affected by wounds, detergents, organic solvents and skin burns as well as skin diseases. Moreover, mechanical flexion may also increase skin absorption (Tinkle, Antonini *et al* 2003; Johanson and Rauma 2008).

3.3 *In vitro* studies

3.3.1 Cobalt

Cobalt NPs were applied (80 nm, range 20-500 nm) at a dose corresponding to 1 mg/cm^2 on human skin mounted in Franz cells. The mean amounts of cobalt penetrated into the receptor medium after 24 h of exposure as measured by ICP-AES were 8.5 ng/cm^2 (0,001% of the applied amount) for intact skin and 1870 ng/cm^2 (0.2%) for skin damaged by abrasion with a needle. The 24-h average flux of cobalt through damaged skin was 76 ng/cm^2/h. The presence of cobalt in epidermis and dermis was confirmed by ICP-AES (Larese Filon, Crosera *et al* 2013).

3.3.2 Fullerenes

Porcine skin was topically dosed with an aqueous solution of a fullerene-substituted phenylalanine peptide derivative (fullerene size 0.7 nm, functionalized size 3.5 nm). Skin was flexed for 60 or 90 min or left unflexed. Confocal microscopy showed dermal penetration of the NPs in flexed skin flexed after 8 h, but not in unflexed skin up to 24 h (Rouse, Yang *et al* 2007).

Fullerenes (C60, 1.1 nm) dissolved in squalene, when applied on human skin in vitro, permeated into epidermis, but was not detected in dermis up to 24 h after dosing. The authors concluded that fullerenes in squalene can permeate into the epidermis but not through the basement membrane, and can therefore not reach into the dermis (Kato, Aoshima *et al* 2009).

3.3.3 Gold

Sonavane *et al* investigated the dermal penetration of three types of citrate-coated gold NPs (15, 102, and 198 nm) using isolated rat skin differing in size and the Franz diffusion cell method. Four ml of donor solution containing roughly 2•1019 NPs was applied on a skin area of area 6.3 cm^2) the Gold NPs showed size-dependent permeation through rat skin. The smallest NPs (15 nm) showed higher permeation compared to the larger ones (102 and 198 nm), as indicated by higher permeability and diffusion coefficients. Thus, 1.1•1018 NPs (6% of the applied amount) of the smallest size penetrated the skin in 24 h, with a lag of less than 1 h. In contrast, 1016 of the 102-nm NPs penetrated skin with a lag of about 3 h. Roughly 2•1014 (0.001%) of the largest NPs penetrated skin, but only after more than 6 h. The permeability coefficients for the three NP sizes were calculated to 2.2•10−6, 1.6•10−7 and 4.8•10−8 cm/s. TEM studies revealed accumulation of the smaller NPs in deeper region of the skin compared to larger NPs, confirming the size-dependent penetration (Sonavane, Tomoda *et al* 2008). There is no mention if and how skin intergety was cotrolled in the study.

Filon *et al* used Franz diffusion cells to measure the uptake of 13-nm gold NPs through intact and damaged human skin. Gold NPs suspended in synthetic sweat was applied on the skin for 24 h at doses corresponding to 15 and 45 µg gold/cm^2. Gold was detected in the receptor medium by ICP-MS after both dosages; the higher dose yielded 214 ng gold/cm^2 (0.5% of the applied dose). The calculated gold flux rates were about 7-8 ng/cm^2/h, with a lag time of less than 1 h and with little difference between intact and damaged skin. However, the gold content was 4-fold higher in damaged than intact skin

(Filon, Crosera *et al* 2011). The reported absorption values are far higher than found by other investigators and the absorption was slightly higher in damaged compared to untreated skin, this suggests that also the untreated skin may have had a disrupted barrier. However, skin integrity was controlled by electrical conductibility measurements.

Labouta *et al* (2011) measured the penetration and metabolic effects of ion-stabilized, polar, 15 nm gold NPs in aqueous solution and sterically stabilized, non-polar, 6 nm gold NPs in toluene on excised human skin. Skin penetration studies were done on frozen or fresh excised skin using static Franz diffusion cells. Dermoscopy and reflectance confocal microscopy showed large aggregates in the furrows after application of nonpolar NPs in water, with no penetration into the skin layers. Penetration was only demonstrated for the neutral gold NPs in toluene. Measurements with multiphoton tomography with fluorescence lifetime imaging microscopy, and TEM showed that these NPs reached down to stratum granulosum with a decreasing gradient throughout the stratum corneum. (Labouta, Liu *et al* 2011).

Lee *et al* investigated the effect of surface charge on the skin penetration in female hairless mice of 18x40 nm gold nanorods. The nanorods were lined with an outer polymer layer. Positive nanorods were coated with either CTAB (zeta potential +31.3 mV) or CTAB-PSS-PDADMAC (+61.1 mV), negative nanorods with CTAB-PSS (-66.3 mV). TEM image analysis showed that the penetration into stratum corneum was approximately three- to fourfold increased for negatively compared to positively charged nanorods. Consistent with the TEM observations, ICP-MS analysis of receptor fluid from Franz cell permeation studies (applied dose 50 µg) showed approximately sixfold higher concentrations of gold a 48 h after exposure to negative compared to positive nanorods (Lee, Jeong *et al* 2013). The 48-h percutaneous uptake of negative nanorods can be calculated to 360 ng (skin area not given), corresponding to 0.7% of the applied dose.

3.3.4 Iron

Baroli *et al* (Baroli, Ennas *et al* 2007), using full thickness human skin, demonstrated by electron microscopy and by inductively coupled plasma optical emission spectroscopy (ICP-OES) that iron NPs smaller than 10 nm (iron oxide coated with tetramethylammonium hydroxide, 5.9 nm by TEM, 49 nm by DLS; iron NPs coated with sodium bis(2-ethylhexyl)sulfosuccinate, 4.9 nm by TEM, 4.8 nm by DLS) were able to penetrate the hair follicle and stratum corneum and occasionally reach the viable epidermis. No permeation through skin was detected during the 24 h of exposure (Baroli, Ennas *et al* 2007).

3.3.5 Latex

Kohli *et al* (2004) applied fluorescent latex particles (1% v/v in water) ranging in size (50, 100, 200 and 500 nm, *ie* only the smallest ones were NPs) and charge (positive, negative, neutral) to the surface of full thickness pig skin in a diffusion chamber. Fluorescence microscopy revealed accumulation in the stratum corneum and the viable epidermis. Only negatively charged 50 and 500 nm particles were able to permeate the skin. For both particle sizes, the amount permeated, as measured by fluorescence

spectrophotometry, reached about 0.1% of the applied dose after 4 h. However, there was no confirmation of particle integrity (*ie* that the fluorescence originated from the particles only) or visual confirmation of particles in the receptor medium. According to the authors, the results suggest that negative particles with sufficient charge may be ideal delivery vectors for antigens and DNA in transdermal vaccination (Kohli and Alpar 2004).

3.3.6 Magnesium oxide

The dermal absorption potential of a nanocrystalline magnesium oxide (7 x 100-200 nm, aggregate diameter 4.8 µm) and titanium dioxide (<1 nm, aggregate diameter 5 µm) mixture in dermatomed human skin was measured using Bronaugh-type flow-through diffusion cells. The material was applied on the skin surface as dry powder, in a water suspension, or in a water/sodium lauryl sulfate suspension for 8 h at a dose of 50 mg/cm^2. Dermal absorption of the nanocrystalline into the receptor medium was not detected by ICP-MS (van der Merwe, Tawde *et al* 2009).

3.4 Polystyrene

Confocal laser scanning microscopy (CLSM) was used to visualize the distribution of non-biodegradable, fluorescent, polystyrene NPs (20 and 200 nm) across porcine skin mounted in diffusion cells. The analyzes (exposures up to 2 h) showed that the NPs accumulated preferentially in the follicular openings in a time-dependent manner, and more so for the smaller size of NPs. In the surface images, NPs were also seen in skin furrows, however, the cross-sectional images showed that this was not a penetration pathway as the transport was clearly impeded by the stratum corneum (Alvarez-Roman, Naik *et al* 2004).

In vitro skin permeation experiments were performed for 6 h with dermatomed porcine skin and polystyrene (28-31 nm) and polymethyl methacrylate (79-100 nm) NPs containing covalently bound fluorescein methacrylate and dispersed Nile Red dye. Confocal microscopy after 6 h of exposure showed that the NPs did not penetrate beyond the superficial stratum corneum and that cleaning of the skin surface removed NPs present in the furrows but not those around hair follicles. In contrast, the unbound Nile Red dye penetrated into deeper layers of the stratum corneum to some extent (Wu, Price *et al* 2009).

Three NPs (approx. 100 nm in diameter) with different surface charge were investigated with respect to their ability to deliver an “active” agent into the skin. The three NPs were: cationic amino-functionalized polystyrene (115 nm), anionic carboxyl-functionalized polystyrene (87 nm) and anionic poly-(L-lactide) (138 nm), into each of which a fluorophore (representing an active agent) was incorporated. Formulations were applied to excised porcine skin in vitro for 6 h, whereafter the skin was cleaned and examined by laser scanning confocal microscopy or subjected to repeated tape-stripping and subsequent analysis of the removed stratum corneum for the presence of the fluorophore. The cationic NP showed clear affinity for the negatively charged skin surface (in contrast to the anionic NPs) and delivered a significantly greater amount of the fluorophore into stratum corneum (Wu, Landfester *et al* 2010).

The penetration in dermatomed pig skin of 400 µg of fluorescent polystyrene NPs in aqueous suspension was studied with confocal fluorescence microscopy. The NPs only infiltrated the stratum disjunctum, *ie*, the skin layers in final stages of desquamation. This minimal uptake was independent of contact time (up to 16 h) and NP size (20-200 nm). When the skin barrier function was mildly damaged by tape stripping, the NPs remained incapable of penetration beyond the most superficial layers (2-3 µm) of the stratum corneum (Campbell, Contreras-Rojas *et al* 2012).

3.4.1 Quantum dots

Ryman-Rasmussen *et al* investigated the dermal penetration of selected commercially available QDs of two sizes and with three different coatings (62.5 pmol, neutral (polyethylene glycol), anionic (carboxylic acids), or cationic (polyethylene glycol-amine)) through intact porcine skin using flow-through diffusion cells. Confocal microscopy showed that spherical QD 565 (4.6 nm) and, to a lesser extent, ellipsoid QD 655 (4x6 nm), independent of surface coating, penetrated the stratum corneum and localized in the deeper skin. However, penetration of anionic carboxylic acid-coated QD 655 into the epidermal layers was only seen after 24 h. The authors concluded that QDs of different sizes, shapes, and surface coatings may penetrate intact skin at occupationally relevant exposures within a working day (Ryman-Rasmussen, Riviere *et al* 2006).

QDs (1 µM, 4.6 nm QD655 and 6x12 nm QD565) coated with carboxylic acid were studied for 8 and 24 h in flow-through diffusion cells with non-treated, flexed, tape-stripped and abraded rat skin. QDs were analyzed in the skin by confocal laser imaging and in receptor medium by fluorescence spectrometry and ICP-OES. Nontreated skin did not show any QD penetration, flexed skin showed an increase on the skin surface but no penetration, while tape-stripped skin depicted QD only on the surface of the viable epidermis. QD655 penetrated into the viable dermal layers of abraded skin at both 8 and 24 h, while QD565 was present only at 24 h. QDs or cadmium were not detected in the perfusate for any of the conditions. The authors concluded that the rat skin penetration of these QDs is primarily limited to the uppermost stratum corneum layers of intact skin (Zhang and Monteiro-Riviere 2008).

QD621 dots (8x6 nm, nail-shaped, CdSe sore, CdS shell, coated with polyethylene glycol, soluble in water) were topically applied to porcine skin flow-through diffusion cells for 24 h. The penetration in skin was studied by confocal microscopy. QDs fluorescence was found primarily in the stratum corneum and near hair follicles. TEM analyzes revealed that the QDs were located in the intercellular lipid bilayers of the stratum corneum. No QDs or cadmium could be detected in the perfusate by ICP-OES and fluorescence spectrometry. These results indicate that porcine skin penetration of QD621 is minimal and limited primarily to the outer stratum corneum layers (Zhang, Yu *et al* 2008).

QDs (cadmium and technetium, 3.5 nm) were applied for 14 h on excised human skin. Distribution on the skin and penetration in the skin were analyzed by multiphoton- and confocal laser scanning microscopy. Mechanical massaging of the skin for 5-10 min affected the distribution pattern on the skin surface, but there was no evidence of penetration into the skin other than into the first few µm. QDs could be found in deeper

layers (down to 7 µm) only after massaging of damaged skin (by 20 tape strips) for 10 min (Gratieri, Schaefer *et al* 2010).

The QD penetration of surfaced modified QDs (30-62 pmol/cm^2, PEG-, PEG-amine, and PEG-carboxyl coated, 4.6 nm) in intact and tape-stripped excised human skin was investigated at pH 7, 8.3 and 9.0 by laser-scanning fluorescence confocal microscopy. There was some penetration into intact viable epidermis of skin for the PEG-QDs at pH 8.3 but not at pH 7 and no penetration at any pH for the other QDs. After tape stripping (30 strips), all QDs penetrated through the viable epidermis and into the upper dermis within 24 h (Prow, Monteiro-Riviere *et al* 2012).

3.4.2 Silica

Fluorescence microscopy showed that 28-d dermal application of well-dispersed amorphous silica NPs (70 nm) on female BALB/c mice penetrated the skin barrier and was detected in regional lymph nodes, liver, cerebral cortex and hippocampus. The amounts of NPs translocated were not quantified (Nabeshi, Yoshikawa *et al* 2011).

The skin penetration and cellular uptake of non-functionalized (negative zeta potential) and APS-functionalized (3-(aminopropyl)triethoxysilane, positive zeta potential) amorphous silica particles of four sizes, 42, 190, 75 and 291 nm, were investigated using intact human explants (applied concentration 0.4%) and cultured human keratinocytes (HaCaT cells, applied concentration 10 µg/ml), respectively. DLS measurements and statistical analyzes of TEM images were used to estimate the degree of particle aggregation. Despite partial particle aggregation in physiological media, particles were taken up by skin cells in a size-dependent manner. APS-functionalization enhanced the in vitro cellular uptake. However, this effect was counteracted by the tendency of particles to form aggregates, leading to lower cellular internalization ratios. After topical application on human skin explants with partially disrupted stratum corneum, only the smallest (42 nm) NPs were found to be associated with epidermal cells and especially dendritic cells, and this was independent of the surface charge (Rancan, Gao *et al* 2012).

3.4.3 Silver

The in vitro skin penetration of silver NPs coated with polyvinylpyrrolidone (25 nm, size range 10-49 nm) was studied using Franz diffusion cells mounted with intact and damaged human skin. The skin was exposed for 24 h to 70 µg/cm^2 of NPs dispersed in synthetic sweat. Silver in the receptor fluid was measured by electro thermal AAS. Silver NPs were detected in the stratum corneum and the outermost surface of the epidermis by TEM. The 24-h silver flux permeation in damaged skin was 0.62 ng/cm^2 with a lag time of less than 1 h. Median silver penetration was 0.46 (range from below the limit of detection to 2.23) ng/cm^2 in intact skin and 2.3 ng (0.43-11.6) ng/cm^2 in damaged skin (Larese, D'Agostin *et al* 2009). The median penetrated amounts in 24 h correspond to 0.0007% and 0.003% of the applied dose, respectively.

The skin penetration of PVP-coated silver NPs (70 nm) was investigated ex vivo in porcine ears by two-photon tomography with a fluorescence lifetime imaging technique, confocal Raman microscopy, and surface-enhanced Raman scattering microscopy. After the application of 12 µg Ag NPs /cm^2, the ears were incubated for 24 h at 37ºC. The

fluorescence imaging showed a dramatic decrease of NP-related signal intensity from the skin surface down to a depth of 4 µm. Below 4 µm, the signal declined and disappeared completely at 12-14 µm depth. The penetration depths of silver were 11.1 and 15.6 µm, as measured by the two methods (Zhu, Choe *et al* 2015).

The penetration of PVP-coated silver NPs (25% silver, 19 nm) in synthetic sweat through human skin grafts typically used for skin burns was studied with Franz cells. The applied amount of NPs corresponded to 113 µg silver/cm^2. The 24-h silver fluxes measured by ICP-MS were 0.2, 0.3 and 3.8 ng/cm^2/h for fresh, cryopreserved and glycerolized skin, respectively (Bianco, Adami *et al* 2014).

3.4.4 Titanium dioxide

Microfine titanium dioxide has become a common ingredient in sunscreen formulations due to efficient UV absorption. Sizes between 15-20 and 300 nm have been reported (SCCNFP/0005/98, Opinion of the scientific committee on cosmetic products and non-food products intended for consumers concerning titanium dioxide).

Bennat and Müller-Goymann, using AAS for analyzes of titanium, demonstrated an exponential decline of titanium in sequential tape strips following exposure to sunscreen formulations (5% w/w TiO_2) in vivo (forearms of volunteer during 45 min) as well as in vitro (human abdominal skin during 24 h) using diffusion cells. The average particle size was stated to be below 30 nm. They also found that the microfine titanium dioxide particles reaches deeper in the stratum corneum from an oily dispersion than from an aqueous one, and that penetration was greater when applied to hairy skin, suggesting a surface penetration through hair follicles or pores (Bennat and Muller-Goymann 2000).

Microfine titanium dioxide (T-Lite SF-S and T-Lite SF) were tested for penetration during 24 h in porcine skin using Franz cells and analysis by ICP-AES and ICP-MS. The mean total recovery was 98-100% and 86-93%, respectively, of the applied amount (400 µg). Virtually all applied titanium could be removed from the skin by washing of the surface. The amounts of titanium found in the tape strips and skin preparations were below or close to the analytical determination limit. No titanium was detected in the receptor fluid. According to the authors, the study shows that neither titanium ions nor microfine titanium dioxide particles are able to penetrate porcine stratum corneum (Gamer, Leibold *et al* 2006).

The penetration through human skin of titanium dioxide (3%, 20-70 nm) and zinc oxide (1%, 200 nm) in sunscreen emulsions was determined using Franz cells (applied doses 60 and 20 µg/cm^2, respectively). Metals in the receptor fluid were measured by ICP-OES. After a test of 24 h duration, no penetration of these particles into the receptor medium could be demonstrated (Durand, Habran *et al* 2009). The detection limits for titanium and zinc in the receptor medium were stated to be 10 ng/ml, this corresponds to 42 and 32 ng/cm^2 or 0.05% and 0.16% of the applied dose for the two particle types.

Contrasting results were obtained from dermal exposure experiments in vitro and in vivo to titanium dioxide NPs. Thus, NPs of various sizes (5, 10, 21, 25, 60 and 90 nm, applied doses 25 mg) did not penetrate through stratum corneum in isolated porcine skin during 24 h, as measured by AAS in the receptor medium of Franz cells. However, when topically applied on pig ear for 30 d and on hairless mice for 60 d, TEM imaging

showed that NPs (4 and 60 nm) penetrated through the stratum corneum and through skin reaching other organs (see section in vivo studies – Titanium dioxide below for details) (Wu, Liu *et al* 2009).

The skin penetration of four different types of rutile titanium dioxide NPs (uncoated 35 nm, alumina/silica/silicon coated 35 nm, mixture of alumina coated and silicon coated 10x100 nm, uncoated 250 nm, applied doses were 200 µg for 24 h) suspended in decamethylcyclopentasiloxane (D5) was determined in vitro with intact, stripped, and hair-removed skin of Yucatan micropigs. Titanium in skin was determined by ICP-MS. The 35 and 250 nm uncoated NPs easily aggregated in suspension with a mean diameter greater than 1 µm. The coated NPs showed good dispersion with a mean diameter of approximately 100 nm. No penetration was observed regardless of NP type in intact and stripped skin. The concentration of titanium in skin was significantly higher when the coated 35-nm NPs were applied on hair-removed skin. SEM with energy-dispersed X-ray spectrometry (EDX) examination showed that titanium penetrated into vacant hair follicles but not into dermis or viable epidermis (Senzui, Tamura *et al* 2010).

Monteiro-Riviere *et al* studied the penetration of titanium dioxide and zinc oxide through ultraviolet B (UVB) damaged pig skin mounted on flow-through diffusion cells. Four sunscreen formulations were tested. The primary NP size was 10x50 nm for titanium dioxide, with mean agglomerate size of 200 nm, and 140 nm for zinc oxide. TEM investigations showed that the titanium dioxide NPs (4 mg, 24 h) had penetrated deep into the stratum corneum, whereas the zinc oxide (2 mg, 24 h) remained on the surface. In addition, penetration of both NP types into the epidermis was demonstrated by time-of-flight secondary ion mass spectrometry. No titanium or zinc was detected in the perfusate (analyzed by TEM-EDX or ICP-MS), indicating minimal transdermal absorption. Similar results were obtained with UVB-damaged skin in vivo, with less penetration in normal skin (Monteiro-Riviere, Wiench *et al* 2011).

3.4.5 Zinc oxide

The absorption of microfine zinc oxide (mean diameter 80 nm, 90% of particles <160 nm, 400 µg for 24 h) in cosmetic formulations through porcine skin was investigated in vitro using Franz cells, with determination of zinc by AAS. The mean total recovery of zinc was 102-107% of the applied amount. Virtually all the applied zinc was recovered in the first five tape strips. The amounts of zinc found in the skin membrane and the receptor fluid and the absorption-time plots were comparable in untreated, vehicle treated and test substance treated skin preparations, suggesting minimal absorption of zinc oxide particles through the skin (Gamer, Leibold *et al* 2006).

Cross *et al* (Cross, Innes *et al* 2007) investigated the skin absorption of different formulations (0, 20 and 60 wt%) of 26–30 nm zinc oxide NPs through human abdominal skin from female donors. Zinc was measured by ICP-MS. The authors found that, similar to the application of placebo, less than 0.03% of the applied zinc, a value similar to that obtained after application of placebo, was detected in the receptor medium. Furthermore, no NPs could be detected by in the lower stratum corneum or viable epidermis by TEM, suggesting that minimal NP penetration occurs through the human epidermis (see Table 1).

The skin penetration of a commercial nanosized zinc oxide (30 nm, 2 mg/cm^2, for 12 h) was investigated using porcine skin. Laser diffractometry showed that the NPs were arranged as agglomerates and aggregates in the size range 0.6-60 µm. The tested NPs did not penetrate into viable layers of the intact porcine skin as determined by SEM-EDX. The particles tended to accumulate on the skin folds and in these regions they may penetrate into the stratum corneum. (Detoni, Coradini *et al* 2014).

Mouse skin was exposed in Franz cells for 12 h to 4 mg of 2-nm zinc oxide NPs in physiological saline with oleic acid and/or ethanol added as penetration enhancers. The NP distribution in stratum corneum was investigated by 3-dimensional multiphoton microscopy imaging. Oleic acid, ethanol and the two in combination all enhanced the NP penetration down to a skin depth of about 15-20 µm (Kuo, Wu *et al* 2009).

3.5 In vivo studies

3.5.1 Fullerenes

Xia *et al* (2010) examined the skin penetration of pristine fullerenes from different types of industrial solvents. Three pigs were topically dosed with 100 µg fullerenes in solvent for 24 h and re-dosed daily for 4 d. The dose sites were tape-stripped 26 times, followed by skin biopsies. When dosed in toluene, cyclohexane or chloroform, but not mineral oil, the fullerenes penetrated deeply into the stratum corneum. More C60 was detected in the stratum corneum when dosed in chloroform compared to toluene or cyclohexane (Xia, Monteiro-Riviere *et al* 2010).

3.5.2 Gold

Penetration of gold particles (94 and 161 nm) coated with silica and silica particles (298 nm) coated with gold in human skin was investigated by SEM-EDX. No deeper penetration was observed other than on the superficial layer of the stratum corneum and on the epithelium in superficial parts of hair follicles (Graf, Meinke *et al* 2009).

The clipped skin of female Balb/c mice was exposed for 3 h to a suspension of 5-nm gold NP coated with PVP. Light microscopy of silver-enhanced staining Eosin counterstain revealed that NPs crossed the stratum corneum and spread widely over the epidermis layer. A limited amount of NPs was also detected in the dermis layer. No significant accumulation was observed in the skin appendages such as hair follicles (Huang, Yu *et al* 2010).

3.5.3 Polystyrene

The penetration of solid fluorescent 40 and 200 nm polystyrene NPs was studied in C57BL/6 female mice. Confocal fluorescence microscopy imaging showed that the 40 nm NPs penetrated via hair follicle openings and translocated into the viable tissue, where they were internalized by skin antigen-presenting cells. Moreover, within 24 h, the NPs migrated to the proximal lymph nodes, most likely in association with migrating antigen-presenting cells (Mahe, Vogt *et al* 2009).

3.5.4 Quantum dots

Kim *et al* showed by near-infrared (NIR) fluorescence imaging that NIR type II quantum dots (10 nm) administered in the dermis of mice and pigs migrate to regional lymph nodes, potentially via skin macrophages and Langerhans cells, raising potential concern for immunomodulation. In pigs, between 2% and 4% of the injected dose (400 pmol) was found in the sentinel lymph nodes (Kim, Lim *et al* 2004).

Gopee *et al* (2007) measured cadmium and selenium levels by ICP-MS in various tissues up to 24 h after intradermal injection of QDs (CdSe core, CdS capped, PEG-coated, 37 nm, 48 pmol). The time courses showed time-dependent decrease in cadmium at the injection site, and increases in the liver, regional draining lymph nodes, kidney, spleen, and hepatic lymph node. The tissue distribution was corroborated by fluorescence microscopy. Furthermore, within min after injection, the highly UV fluorescent QDs could be observed moving from the injection sites apparently through the lymphatic duct system to regional lymph nodes. (Gopee, Roberts *et al* 2007).

Gopee *et al* also studied how skin damage influences the penetration. The same type of QDs were applied in an oil-in-water emulsion to intact, tape stripped (stratum corneum removed), acetone treated, or dermabraded (stratum corneum and epidermis removed) mouse skin. QD penetration into the skin was monitored in the liver and regional draining lymph nodes by ICP-MS analysis of cadmium. No consistent cadmium elevation was detected in the sentinel organs of mice with intact, acetone pretreated, or tape-stripped skin 24 h and 48 h after application, however, in dermabraded mice, cadmium elevations were detected in the lymph nodes and liver. The QD accumulation (as cadmium) in the liver was approximately 2.0% of the applied dose (2 mg/cm^2, exposed area approximately 2.6 cm^2). The uptake through dermabraded skin was confirmed by confocal fluorescence microscopy (Gopee, Roberts *et al* 2009).

Carboxylated QDs (30 nm, 3 pmol/cm^2) were applied in a glycerol vehicle to the skin of hairless SKH-1 mice equipped with Elizabethan collar for 8 or 24 h, with and without previous UV radiation exposure (with quantities of UVA and UVB corresponding to medium level sunburn in a human). The penetration pattern was investigated using tissue histology, confocal fluorescence microscopy and TEM-EDX). Low levels of penetration were seen in both non-treated and UV-treated mice, with qualitatively higher levels of penetration in the latter (Mortensen, Oberdörster *et al* 2008).

The 4-h skin penetration of 7-nm PEG-amine coated QDs (16 pmol) in human skin was studied in vivo by tape stripping and confocal fluorescence microscopy and differential interference contrast imaging. Fluorescence from QDs was detected in the first 15 tape strips. Penetration was also studied in vitro using the system EpiDerm™, a 3-D human tissue construct of non-transformed human keratinocytes organized into basal, spinous, and granular layers along a multi-layered stratum corneum with an air-liquid interface (ALI). TEM imaging showed accumulation of QDs in the stratum corneum but not in the lower, viable skin layers. EDX analysis of the TEM-identified particles confirmed that their elemental composition corresponded to QDs. Higher magnification showed that QDs that were located along the periphery of lipid droplets in the keratin layer of epidermis image. According to the authors, the findings suggest transdermal absorption

of QDs after dermal exposure over a relatively long period of time (Jeong, Kim *et al* 2010).

Carboxylated QDs (cadmium selenium core, zinc sulfide shell, 14 nm) were applied for 24 h to the skin of untreated mice and to UVB-treated mice 3-4 d after UVB exposure, *ie* at the peak of the skin barrier disruption. Phase contrast and fluorescent microscopy images revealed there was an increased presence (although still rare events) of QDs In UVR-irradiated skin, below the stratum corneum away from hair follicles. In addition, AAS analysis revealed a marginal but statistically significant increase in cadmium in the liver of UVB-treated compared to untreated mice (7.4 *vs* 5.7 ng cadmium per liver). For comparison, the applied amount of QDs was approximately 105 pmol or 105 µg. No cadmium increase in liver was seen in mice treated with UVB only or with QDs only. These results suggest that the barrier damage caused by UVB resulted in a marginal uptake of QDs (Mortensen, Jatana *et al* 2013).

QDs (selenium sulfide, 20 nm) were applied dorsally to male hairless ICR mice. Fluorescence microscopy, TEM and ICP-MS were used to assess the distribution of QDs in the skin and organs up to 120 h after dosing. The QDs penetrated into the dermal layer and were mainly located in the uppermost stratum corneum layers and the hair follicles. The concentration of cadmium was approximately doubled in liver (10 *vs* 5 ng/g), spleen and kidney in QD treated compared to control animals (Tang, Zhang *et al* 2013). The dermally applied dose of QDs was 0.32 nmol, corresponding to 8 mg cadmium (based on a molar mass of 50000 and 50% cadmium in QDs).

3.5.5 Silica

Well-dispersed amorphous silica NPs (70 nm, 250 mg) were applied to the inner side of the ears of BALB/c mice for 3 consecutive days. TEM analyzes revealed the presence of NPs in Langerhans cells, dermis and cervical lymph nodes (Hirai, Yoshikawa *et al* 2012).

FITC-labeled fluorescent AHAPS-functionalized silica NPs (55 nm) with positive zeta potential were topically applied on intact, tape stripped or on inflamed skin of SKH1 mice with induced allergic contact dermatitis for 1 or 5 d at daily doses of 250 µg. No penetration of NPs through the skin was observed regardless of skin treatment. Following subcutaneous injection the NPs were found inside macrophages and partially transported to local lymph nodes (Ostrowski, Nordmeyer *et al* 2014).

3.5.6 Silver

Vlachou *et al* measured systemic silver levels in 30 skin-burn patients receiving treatment with wound dressings containing nanocrystalline silver. Serum silver levels were measured before, during and after use of the wound dressings, and again after 3 and 6 months. The median total postoperative wound size was 12% of the total body surface area. A maximum serum silver level of 56.8 µg/L was reached after 9 d (median values). No haematological or biochemical indicators of toxicity were associated with the silver absorption. The systemic appearance of silver is no proof of transdermal absorption of the NPs, as silver is easily released from the NPs (Vlachou, Chipp *et al* 2007).

Korani *et al* exposed male albino guinea pigs to two concentrations of colloidal nanosilver (size <100 nm) (1 and 10 g/L) in an acute study and three concentrations of nanosilver (0.1, 1 and 10 g/L) in a subchronic study. The tissue levels of Ag NPs correlated with the applied doses ($p < 0.05$) in a dose dependent manner with the following ranking: kidney > muscle > bone > skin > liver > heart > spleen. Toxic responses were assessed by clinical and histopathologic parameters. The sites of exposure were scored for any type of dermal toxicity and compared with negative control and positive control groups. In autopsy studies during the acute test, no significant changes in organ weight or major macroscopic changes were detected, but dose-dependent histopathologic abnormalities were seen in skin, liver, and spleen of all test groups, with more abnormalities in the chronically exposed group. The authors concluded that colloidal nanosilver may elicit target organ toxicity in a dose- and time-dependent manner (Korani, Rezayat *et al* 2011; Korani, Rezayat *et al* 2013).

A nanocrystalline silver dressing (Acticoat, containing 10-40 nm silver crystals) was applied to a sample of 16 healthy patients with normal intact skin 5 d prior to surgery. The treated skin samples, removed as surgical waste, were then analyzed by tissue mass spectrometry, light microscopy, SEM and X-ray diffusion spectrography. Silver serum levels were also analyzed before and after application of the NPs. A limited amount of silver penetration could be noted even with light microscopy. With SEM, metallic particles could be seen within the dermis and X-ray diffusion spectrography (XRD) confirmed that these were silver species, possibly oxides. Furthermore, silver clusters as large as 750 nm were observed in the dermis. There was no rise in serum silver levels post-treatment compared to pre-treatment (George, Merten *et al* 2014).

3.5.7 Titanium dioxide

Microfine titanium dioxide has become a common ingredient in sunscreen formulations due to efficient UV absorption. Sizes between 15-20 and 300 nm have been reported (SCCNFP/0005/98, Opinion of the scientific committee on cosmetic products and non-food products intended for consumers concerning titanium dioxide)

Tan *et al* (Tan, Commens *et al* 1996) performed a pilot study on percutaneous absorption of microfine titanium dioxide (8%) from sunscreens. The size and size distribution of the particles used were not reported, but (a fraction) was indirectly stated to be 10-50 nm. Thirteen volunteers scheduled to have skin surgery applied sunscreen formulation on the skin for 2-6 wk prior to surgery. The stratum corneum was tape stripped once (cyanoacrylate + adhesive plaster) from the excised skin samples and titanium was measured in epidermis and dermis by ICP-MS. The concentration of titanium after digestion of the skin was evaluated. Although not statistically significant, the titanium concentration tended to be higher in the skin biopsies from the exposed subjects than in those from the controls (Tan, Commens *et al* 1996).

The finding of Tan *et al* (Tan, Commens *et al* 1996) could not be confirmed by Lademann and coworkers (Lademann, Weigmann *et al* 1999). Volunteers were treated with sunscreen containing UV-Titan M 160 (83% titanium dioxide coated with 10% alumina and 7% stearic acid) five times per day for 3 d and once on day 4. The stratum corneum was removed by repeated tap stripping and tapes were analyzed by Raman spectrometry. Most titanium was found in the first 10 tape layers and the concentration

decreased steeply with each layer. Deeper layers of the stratum corneum and viable skin were devoid of titanium dioxide even after repetitive application of sunscreen preparations when analyzing interfollicular areas. Microparticles were only detected in the hair follicle, in amounts less than 1% of the applied amount (Lademann, Weigmann *et al* 1999).

Spatially resolved ion beam analysis (particle induced X-ray emission (PIXE), scanning transmission ion microscopy (STIM), Rutherford backscattering (RBS) and secondary electron imaging) was performed on freeze-dried cross-sections of biopsies of pig skin, exposed in vivo for 48 h to four different formulations containing 4.5, 5, 18 or 40% titanium dioxide NPs. The particle size of was determined with TEM. The NPs were lance-shaped, 45–150 nm by 17–35 nm. The analysis concentrated on the penetration depth and on pathways of the NPs into the skin. In these measurements a penetration of NPs through the stratum corneum to the underlying stratum granulosum via the intercellular space was found. Hair follicles did not seem to be important penetration pathways as no titanium dioxide was detected in the follicles. The NP concentration in the stratum spinosum was below the detection limit (Menzel, Reinert *et al* 2004).

The 48-h penetration of titanium dioxide NPs in human epidermis was investigated by using human foreskin grafts transplanted into mice. TEM and combined ion beam analysis techniques. Skin grafts were treated in occluded conditions for different time periods with a hydrophobic emulsion containing titanium dioxide NPs. A variety of methods (TEM, PIXE, STIM, RBS) was used to detect titanium and NPs in quick-frozen punch biopsies. NPs were shown to have penetrated into the corneocyte layers of stratum corneum by TEM as well as by PIXE (Kertesz, Szikszai *et al* 2005).

Human skin grafts transplanted to mice were treated with titanium dioxide NP (9 nm) emulsion at 2 mg/cm^2 in for 24 h under occluded conditions. Titanium content was analyzed at different depths in punch biopsies by PIXE microscopy. The study showed that the titanium dioxide NPs do not penetrate through the intact epidermal barrier (Kiss, Biro *et al* 2008).

Mavon *et al* (Mavon, Miquel *et al* 2007) used the tape stripping method to assess the penetration of two sunscreens, titanium dioxide and methylene bis-benzotriazolyl tetramethylbutylphenol from a broad-spectrum sunscreen formulation into human skin, and in vitro, using a compartmental approach. Titanium dioxide was quantified by a colorimetric method, whereas TEM and X-ray emission techniques were used to localize titanium dioxide in skin sections. More than 90% of both sunscreens were recovered in the first 15 tape strippings (applied dose 54 µg/cm^2). The remaining 10% did was localized in the furrows and and the hair follicle openings. No titanium dioxide was detected in the follicle, viable epidermis or dermis (Mavon, Miquel *et al* 2007).

Similarly, Schulz *et al* (Schulz, Hohenberg *et al* 2002), using optical and electron microscopy, obtained similar results while testing three other types of micronized titanium dioxide in human volunteer experiments; T 805 (20 nm, hydrophobic, cubic, titanium/silica coated), Eusolex T-2000 (100 nm, amphiphilic, needles, titanium/aluminum/silica coated) and Tioveil AQ (100 nm, hydrophilic, needles, titanium/aluminum/silica coated). The emulsions were applied on the forearms for 6 h at doses of 160 µg TiO_2/cm^2. Independent of particle size, shape and surface properties no

dermal absorption was seen. Thus, the titanium dioxide particles were exclusively deposited on the outermost surface of the stratum corneum, and not in deeper stratum corneum layers, human epidermis and dermis (Schulz, Hohenberg *et al* 2002).

Oil-water emulsions of three types of titanium dioxide NPs (20 nm cubic hydrophobic, and 100 nm needles amphiphilic and hydrophilic, 160 µg/cm^2) were applied non-occluded on the forearm of a volunteer for 6 h. Punch biopsies were examined by light microscopy and TEM. For all three types, NPs were only observed in the outermost layer of the stratum corneum with no penetration into deeper skin layers (Pflucker, Wendel *et al* 2001).

Normal human skin was exposed to a test hydrophobic formulation containing coated 20-nm titanium dioxide NPs and also to two commercial sunscreen formulations containing titanium dioxide alone or in combination with zinc oxide. The exposure conditions were: 0.5-1 mg sunscreen per cm^2 applied on 25 cm^2 skin, 2-h open exposure and 48-h occluded exposure. The presence of NPs in transversal skin cryosections was examined by nuclear microscopy. Even after the 48-h occluded exposure, NPs were only detected at the skin surface and in the uppermost stratum corneum regions and in the openings of the hair follicles (Filipe, Silva *et al* 2009).

Titanium dioxide NPs (4 and 60 nm) where topically applied on one clipped ear of male pigs for 30 d at a daily NP dose of 1.2 mg. NPs were detected by TEM in the stratum corneum, stratum granulosum, prickle cell layer and basal cell layer, but not in the dermis. However, only the 4-nm NPs reached the basal cell layer. In a separate experiment, the skin of hairless mice was exposed 3-h daily for 60 d to 400 µg of titanium dioxide particles of various sizes (10, 21, 25, 60 and 400 nm) via skin. The treatment area was protected by a plastic collar which fitted on the neck and remained uncovered. The dressing was removed 3 h later and the remaining residual materials were removed with lukewarm water. Titanium levels measured by AAS were dramatically (ten-fold or more) increased in various organ compared to background levels in untreated animals (Wu, Liu *et al* 2009). Although the authors took some care to avoid secondary exposure via ingestion, this exposure route cannot be dismissed. Therefore the reported systemic uptake and biodistribution is not considered to be reliable.

The skin of minipigs was exposed 4 times daily (5 d/week, 4 wk) to three types of titanium dioxide particles (uncoated 30-50 nm, uncoated 300-500 nm, and dimethicone/methicone copolymer-coated 20-30 x 50-150 nm) in sunscreen formulations (2 mg cream/cm^2 corresponding to approximately 60 µg titanium/cm^2). The epidermis from treated minipigs showed elevated titanium, measured by ICP-MS, compared to control animals exposed to a blank cream. Increased titanium was also detected in abdominal and neck dermis. However, titanium in lymph nodes and liver from treated animals were not increased over control. Using TEM- and SEM-EDX, all three types of titanium dioxide particles were found in the stratum corneum and upper follicular lumens in all treated skin samples. Isolated particles were also present at various locations in the dermis of animals treated with all three types of titanium dioxide-containing sunscreens but this was likely a result of contamination during

sample preparation. In any case, the few observed particles represented a tiny fraction of the total amount applied (Sadrieh, Wokovich *et al* 2010).

An oil-water emulsion of titanium dioxide NPs (17 nm uncoated anatase, 400 µg TiO_2/cm^2) was applied to the dorsal skin of hairless Wistar Yagi rats once daily up to 56 d. Skin samples were taken after 2, 4 and 8 wk and examined by TEM-EDX. NPs were only located in the stratum corneum and the follicular epithelium, no NPs were identified in the viable skin areas. Titanium in organs was measured by ICP-MS and was found to be elevated in lung samples from the treated animals after 8 wk. Most likely this elevation was not due to dermal penetration but to inhalation of NPs (Adachi, Yamada *et al* 2013).

3.5.7.1 Conclusions – dermal penetration of titanium dioxide

Overall, numerous studies convincingly show that ultra- and nanoscale titanium dioxide particles used in sunscreens only penetrate into the outermost layer of the stratum corneum and the openings of the hair follicles. There is no evidence of penetration through undamaged skin, leading to systemic exposure. Single studies have found slight elevations of titanium in lymph nodes and in distant organs, these elevations are most like due to secondary exposure (ingestion, inhalation) and sample contamination.

3.5.8 Zinc oxide

Gulson *et al* (2010) exposed 20 volunteers to two types of sunscreens over five consecutive days under outdoor conditions. Two sunscreens were used, one containing 19-nm ("nano", 11 subjects) and one with >100-nm ("bulk", 9 subjects) zinc oxide particles, both with the zinc oxide enriched to >99% with the stable isotope 68Zn. The average amount of applied sunscreen was 4.3 mg/cm^2. The levels of 68Zn in blood and urine from females receiving the nano sunscreen appeared to be higher than males receiving the same treatment and higher than all subjects receiving the bulk sunscreen. However, blood and urine samples from all subjects exhibited small increases in 68Zn. The amount of 68Zn detected in blood after the 5-d application period was approximately 0.1% of the total zinc in the blood compartment. It is not known whether the 68Zn was absorbed as zinc oxide particles, soluble zinc or both (Gulson, McCall *et al* 2010).

Gulson *et al* (2012) also performed a pilot study (conducted prior to but published after the main study) to determine if zinc from zinc oxide NPs in sunscreen can penetrate human skin in vivo. NPs (similar to 30 nm) with 52% 68Zn enrichment were incorporated in a sunscreen formulation and 2-3 g was applied on the back of 3 human subjects (910 cm^2) twice daily for 5 d. Blood and urine were collected up to 50 d post application. The levels of 68Zn in blood continued to increase after application and peaked after 2 wk but were small and the absorption through skin was estimated to be below 0.01% of the applied dose. Notably, the increase in 68Zn in blood was about twice as high in the outdoor study (Gulson, McCall *et al* 2010), where the volunteers were sunbathing (Gulson, Wong *et al* 2012).

Sunscreens of three types, containing nano (68ZnO, average size 19 nm), bulk (107 nm), or no zinc oxide were applied to the backs female hairless mice on six occasions over 4 d. The exposed area was approximately 50 cm^2. About 0.1 g sunscreen was

applied, corresponding to a zinc oxide dose of 20 mg per application and an overall dose of 120 mg. The mice were fitted with Elizabethan collars to prevent grooming and subsequent ingestion of sunscreen zinc oxide. In addition, the bedding material was analyzed to ascertain that it was not contaminated. Major organs were assessed for changes in 68Zn/64Zn ratios by multi-collector ICP-MS. By conversion of isotope ratios to mass concentrations, the highest concentrations of 68Zn tracer originating from the sunscreens treatment were found in liver (bulk-treated: 12 mg/g, nano treated: 18 mg/g), whereas the lowest concentration was in brain tissue (1.6 and 3.4 mg/g). Concentrations in heart, kidney, lung and spleen were intermediate (bulk treated: 5-7 mg/g, nano-tretaed: 8.6-12 mg/g). Despite this significant uptake of 68Zn from the sunscreen application, no change in total zinc in the major organs was detected (Osmond-McLeod, Oytam *et al* 2014).

A commercial sunscreen containing zinc oxide NPs (26- 30 nm, 0.3 g) was applied on human skin and rubbed in for 5 min. The skin was examined by multiphoton microscopy (MPM) imaging and SEM-EDX 0, 4 and 24 h later. Penetration of NPs beyond the outermost layers of stratum corneum could not be demonstrated (Zvyagin, Zhao *et al* 2008).

Different doses (0, 250, 500 and 1000 mg/kg/d) of citrate coated zinc oxide NPs (20 nm) were dermally applied to S-D rats, daily for 90 d. Analysis of tissues was performed by AES. Increased concentrations of zinc were seen in liver, small intestine, large intestine, and feces, these were likely a result of oral ingestion via licking (Ryu, Seo *et al* 2014).

3.6 Conclusions – dermal penetration

Numerous studies have examined the dermal penetration of various types of NPs. Most of these studies have used different microscopic imaging techniques. These studies consistently show that an overwhelming part of the topically applied NPs are found on the surface or in the outermost layers of stratum corneum. Furthermore, nearly all studies have failed to demonstrate penetration beyond the epidermis. Limitations with these studies are that they are qualitative rather than quantitative in nature, and detection limits are not available. Thus, although the systemic absorption appears to be low, it cannot be ruled out.

On the other hand, a few studies, summarized in Table 2, have used sensitive analytical methods to measure absorption through skin in vitro using diffusion cells, mainly by using metal-containing NPs and analysis by ICP-MS. As seen the 24-h penetrated amount through human skin in vitro ranges from 0.0007% (silver, 25 nm) to 0.5% (gold, 13 nm). It should be noted that many additional factors not specified in table may influence the results, including, *eg*, NP coating, NP agglomeration, concentration of NP in donor medium, composition of donor and receptor medium, pH, design of diffusion cell, etc. Two major factors may contribute to falsely high values, disruption of the barrier during preparation and, maybe more important, dissolution of metal form the NPs prior to absorption.

Larese Filon and colleagues recently performed a thorough review of the skin absorption of NPs (Larese Filon, Mauro *et al* 2015). In contrast to the above reasoning

on diffusion they concluded that experimental data allows for a size-dependent skin rule of thumb for penetration in that NPs sized:

≤4 nm can penetrate and permeate intact skin,

4-20 nm can potentially permeate intact and damaged skin,

21-45 nm can penetrate and permeate damaged skin only,

>45 nm cannot penetrate nor permeate the skin.

The percent uptake in the study of 15-nm NPs by Sonavane *et al* (Sonavane, Tomoda *et al* 2008) is strikingly high compared to other studies. However, also the other studies in Table 2, as well as the rule of thumb suggested by Larese Filon *et al* (Larese Filon, Mauro *et al* 2015), are at odds with theoretical calculations made by Watkinson *et al* (Watkinson, Bunge *et al* 2013). Thus, based on the Potts & Guy equation, Watkinson *et al* calculated permeability coefficients (Kp) for the diffusion through intact skin of NPs, assuming spherical shape, a density of 1 g/cm^3 and a log octanol:water partition coefficient (log K) of 2. The predicted Kp values were 6•10-4, 2•10-17 and 0 cm/h for 1, 2 and 5 nm NPs, respectively. For comparison, the Kp values for neat chemicals with a skin notation (*ie* a warning that skin absorption may contribute significantly to the systemic toxicity of an inhaled chemical) are typically between 0.1 and 10-4 cm/h (Johanson and Rauma 2008). Using the equation of Magnusson *et al*, the predicted maximum flux values were calculated to 0.34, 2•10-28 and 0 µg/cm^2/h, compared to typically 0.1-104 µg/cm^2/h for chemicals with a skin notation. These calculations suggest that NPs, except the very smallest ones of 1 nm, are too large to permeate skin by diffusion.

Table 2. Estimated percutaneous absorption of nanoparticles through intact skin in vitro.

Nano-particle	Size (nm)	Zeta poten-tial	Species	Applied dose (µg/cm^2)	Recovery in receptor medium after 24 h (ng/cm^2)	Absorbed after 24 h (% of applied dose)	Reference
Gold	13	ns [1]	Human	45	214	0.5%	Filon, Crosera *et al* 2011
Gold	15	–	Rat	2·1019 NPs	1.1·1018 NPs	6%	Sonavane, Tomoda *et al* 2008
Gold	18x40	+	Mouse	50 µg	60 ng [2]	0.1% [2]	Lee, Jeong *et al* 2013
Gold	18x40	–	Mouse	50 µg	360 ng [2]	0.7% [2]	Lee, Jeong *et al* 2013
Silver	25	ns	Human	70	0.46	0.0007%	Larese, D'Agostin *et al* 2009
Titanium dioxide	20-70	ns	Human	60	<42	<0.07%	Durand, Habran *et al* 2009
Zinc oxide	200	ns	Human	20	<32	<0.16%	Durand, Habran *et al* 2009

[1] ns – not stated.

[2] After 48 h.

The NP surface charge (zeta potential) may also influence the skin penetration; however, seemingly opposite results have been reported. For example, Ryman-Rasmussen *et al* reported deeper penetration into the stratum corneum of positive compared to negative QDs (Ryman-Rasmussen, Riviere *et al* 2006), whereas Lee *et al* measured up to 6-fold lower percutaneous absorption of positive compared to negative gold nanorods (Lee, Jeong *et al* 2013). Kim and co-workers, using cultured human colon carcinoma cells and mathematical modelling, showed that positively charged drug-carrying gold nanorods had higher uptake and dissociation by viable cells, whereas negative nanorods diffused faster (Kim, Han *et al* 2010). Rancan *et al* similarly found that despite partial particle aggregation, silica particles were taken up by skin cells in a size-dependent manner and that positive particles had a higher cellular uptake rate. On the other hand, the positive particles tended to aggregate, lowering the uptake rate. Thus, there appears to be a complex relation between size, surface charge, pH, aggregation and dermal penetration.

For pharmaceutical drugs and other chemicals, the follicular route has previously been considered to be of minor importance. However, it has been shown that skin penetration rate of different drugs is significantly lower in hairless than in hairy rodents, that the rate correlates with the follicle density and that the rate can be lowered by blocking the follicular openings (for references see *eg* Rancan and Vogt (Rancan and Vogt 2014). There are several reasons for a potential importance of this route also for NPs: large contact area and large storage volume of follicles, well developed capillary network, and less developed stratum corneum (compared to the skin surface). Thus, once accumulated in the follicular canal, NPs might more easily translocate across the stratum corneum and reach the lymph and blood circulation. Skin penetration of NPs via the hair follicles has therefore received considerable attention.

The rule of thumb presented above still needs to be confirmed. In any case, smaller NPs are expected to have a higher ability to penetrate through the skin than bigger ones. In real life conditions, the percutaneous absorption through intact skin of larger NPs (at the 100-nm end) is likely nil or insignificant. The absorption of small-scale NPs (at the 1-nm end) may be a concern. Still the uptake is likely low compared to that of chemicals with a skin notation.

A remaining concern, especially for metal NPs, is that of dissolution *eg* in sweat and subsequent skin penetration of the dissolved molecules/ions. It is well known that metal and metal oxide powders once placed in biologic media can release metal ions (Midander, Pan *et al* 2007; Midander, Pan *et al* 2007; Midander, Wallinder *et al* 2007). Experiments by Larese Filon *et al* (Larese, Gianpietro *et al* 2007) have demonstrated that metallic nickel and cobalt can be oxidised when suspended in synthetic sweat. Release of metal ions may not only enhance the penetration but also result in a changed tendency to form aggregates and an increased sensitizing potential (Larese Filon, Mauro *et al* 2015).

4 Oral exposure

4.1 Introduction

There are two major barriers for NPs to enter the body from the GI tract, namely the mucus and the epithelium. The mucus is a viscoelastic and adhesive gel lining the epithelium surface creating a significant barrier for macromolecules and NPs to cross. Most foreign particles are efficiently trapped in the mucus layers by steric obstruction and/or adhesion (Lai, Wang *et al* 2009). The mucus is continuously renewed and transported distally, thus carrying the trapped particles to the feces. The epithelial cells themselves form the second barrier. Absorption of particles occurs especially via the M cells located in the Peyers patches in the wall of the small intestine (des Rieux, Fievez *et al* 2006), however, absorption via intestinal enterocytes has also been demonstrated. After entering the interstitial space of the gastrointestinal (GI) tract, the NPs are redistributed to other organs via the blood circulation as well as the lymph systems (Li, Al-Jamal *et al* 2010).

4.2 *In vitro* studies

4.2.1 Gold

Sonavane *et al* (Sonavane, Tomoda *et al* 2008) investigated the 6-h dermal (see previous chapter on dermal exposure) and the 24-h intestinal penetration of 15, 102, and 198 nm gold NPs. The gold NPs showed a size-dependent permeation through isolated rat intestine. The number density and amount of NPs was analyzed by UV-VIS spectroscopy and ICP-MS, respectively. The permeation of gold NPs was higher through intestine than through skin. The smallest NPs (15 nm) showed higher permeation compared to the larger ones (102 and 198 nm), as indicated by higher permeability and diffusion coefficients. The lag of appearance in the receptor medium was less than 1 h for all NP sizes. However, about 1000 times more of 15-nm NPs and about 10 times more 102-nm NPs penetrated the intestine, compared to the 198-nm NPs (expressed as number density) (Sonavane, Tomoda *et al* 2008).

4.2.2 Latex

Sinnecker *et al* used isolated perfused rat small intestine to investigate the 6-h absorption of differently sized fluorescent latex NPs (20, 40 and 200 nm). The latex NPs were given as boluses (7.5•1013, 6•1012 and 3.9•1011 NPs) in the isolated intestine, and samples from the luminal, vascular and lymphatic compartments were collected over time and analyzed for latex by fluorescence spectroscopy. No NPs were detected in the vascular and lymphatic systems, whereas over 95% of the doses were recovered in the luminal samples and the dissolved mucus lining the intestinal epithelium (Sinnecker, Krause *et al* 2014).

4.2.3 Polylactide

McClean *et al* followed the binding, uptake and absorption of poly-dl-lactide (PLA) micro- and nanoparticles up to 2 h in Caco-2 monolayers and in ileal tissue and gut associated lymphoid tissue of anaesthetised rats and rabbits. The fluorescein-loaded and

blank microparticles were 30 and 10 μm, respectively, whereas the “nanoparticles” were below 2 μm. Approximately 10% of the particles were adsorbed to the apical membranes of each of the five intestinal models. Nanoparticles were better absorbed than microparticles. Little difference in uptake patterns was seen between Peyer's patch and non-Peyer’s patch tissue. The uptake of PLA particles was low capacity, size-dependent and predominantly transcellular in all systems. A low proportion of the apically-bound particles was absorbed, however, particles larger than 4 μm were not absorbed (McClean, Prosser *et al* 1998).

4.2.4 Polystyrene

Win *et al* studied the cellular uptake of 10-50 μg polystyrene and other polymeric NPs of different sizes (50-1000 nm) for 0.5-4 h using Caco-2 cells. Using fluorescence spectroscopy the authors showed that the cellular uptake was size, concentration and time-dependent. Thus uptake increased less than proportional with concentration, suggesting a capacity limited (saturated) uptake. Also, the uptake levelled off with time, again suggesting saturation. The uptake decreased with increasing particle size (100 – 1000 nm), the exception being 50-nm polystyrene NPs which showed the lowest uptake. Experiments with PLGA NPs coated with polyvinyl alcohol or vitamin E succinated PEG1000 showed that these surface modifications markedly improved the cellular uptake (Win and Feng 2005).

Gastrointestinal mucus consists of a complex network of highly branched glycoproteins and macromolecules that may restrict the diffusion of NPs. Carrier *et al* (Crater and Carrier 2010) explored the barrier properties of gastrointestinal mucus using real-time multiple particle tracking fluorescence microscopy 2 h after addition of amine-, carboxylate-, and sulfate-modified polystyrene NPs (0.1 mg/ml). The anionic NPs diffused 20-30 times faster than the cationic ones. Thus, carboxylate- (228 nm) and sulfate- (235 nm) modified NPs are likely capable of crossing a 10 mm thick layer of mucus (similar to that of the mucus layer observed in the ileum) within min, whereas amine-modified NPs require several hours (aggregate diameter 200-2000 nm, average 666 nm) (Crater and Carrier 2010).

Using polystyrene NPs (50 nm), Walczak *et al* investigated the impact of gastrointestinal digestion in vitro on protein corona formation and NP translocation across an in vitro intestinal barrier. Co-cultured intestinal Caco-2 and HT29-MTX cells were exposed to neutral and positively and negatively charged NPs. In vitro digestion significantly reduced the amount and composition of proteins in the corona, predominantly by decreasing the presence of high molecular weight proteins. The digestion also significantly increased the translocation of most NP types. The authors stress the importance of including in vitro digestion when studying in vitro intestinal translocation (Walczak, Kramer *et al* 2015).

4.2.5 Silver

Bouwmeester *et al* used an intestinal epithelium coculture model consisting of Caco-2 and M-cells to study the translocation of silver NPs. As these NPs leak silver, also silver ion was investigated. The cell culture was exposed (5 and 25 μg/ml) to four NP sizes (20, 34, 61 and 113 nm) and silver nitrate for 4 h. Silver was detected by ICP-MS or

AAS. The amount of silver ions that passed the cell barrier was equal for the silver ion and NP exposures. The authors concluded that the translocation of silver is likely in the ionic and not in the particulate form (Bouwmeester, Poortman *et al* 2011).

The behavior of 60 nm monodisperse silver NPs (10 µg/ml) and silver ions (1µg/ml) was studied in an in vitro human digestion model, simulating a gastrointestinal transit time of approximately 4 h. Samples after saliva, gastric and intestinal digestion were analyzed with single particle ICP-MS, DLS, TEM and SEM-EDX. In the presence of proteins, after gastric digestion the number of particles dropped significantly, to rise back to original values after the intestinal digestion. SEM-EDX revealed that reduction in number of particles was caused by their clustering. These clusters were composed of silver NPs and chlorine. During intestinal digestion, these clusters disintegrated back into single 60 nm NPs. The authors conclude that these NPs under physiological conditions can reach the intestinal wall in their initial size and composition. Importantly, intestinal – but not salivary or gastric - digestion of silver nitrate in presence of proteins resulted in particle formation. These NPs (20-30 nm) were composed of silver, sulfur and chlorine (Walczak, Fokkink *et al* 2013).

4.2.6 Titanium dioxide

Janer *et al* used different in vitro and in vivo test methods to evaluate the cellular uptake and oral absorption of titanium dioxide NPs (the in vivo experiment is described later, see section in vivo studies below). The NPs (18 nm, 100 µg/ml, 72-h incubation) were readily taken up by A549 cells (adenocarcinomic human alveolar basal epithelial cells) in vitro, as evidenced by TEM. The NPs were present as agglomerates of different sizes within cytoplasmic vesicles. Most NPs had sizes around 20–30 nm, but some NPs were considerably larger, up to 200–300 nm. The agglomerates ranged from a few NPs, with a total size less than 100 nm, to hundreds of NPs, with total size above 1000 nm. No NPs were found free in the cytoplasm or nucleus, however, in some cases the NPs agglomerates were seen bound to the cell membranes (Janer, Mas del Molino *et al* 2014).

Titanium dioxide particles (1 mg/ml) were also added to Caco-2 cells grown in transwell inserts. The NPs could move freely through the insert membrane in the absence of cells, but only a very small proportion (below or close to the detection limit, corresponding to 0.4% of the applied concentration) was able to cross the insert when the cellular membrane was present (Janer, Mas del Molino *et al* 2014).

4.3 *In vivo* studies

4.3.1 Cerium oxide

The acute toxicity and tissue distribution of 30-nm cerium oxide NPs in rats were investigated after single oral doses 100 and 5000 mg/kg bw. The cerium oxide NPs tended to increase in all investigated tissues (liver, kidney, spleen, lung, testis, brain) with a marked (and statistically significant) increase in lung. The authors attribute the low levels in the tissues to a low bioavailability of these NPs (Park, Park *et al* 2009).

Kumari *et al* investigated the 28 days of repeated toxicity of 30, 300 and 600 mg/kg body weight (bw)/day of cerium oxide NPs (24 nm) and microparticles (3.1 µm) in male

and female Wistar rats after oral exposure. Cerium levels (determined at day 28 by ICP-OES) in the NP-dosed animals increased in tissues and excreta in a dose-related manner and and were approximately doubled in the high dose group compared to control in brain, spleen and heart and five times higher compared to control in blood and urine. Animals dose with microparticles whoed only minimal increases in cerium levels in tissues and urine. Substantial and similar amounts of NPs and microparticles were excreted via feces. There was no obvious sex difference in the disposition of either particle size (Kumari, Kumari *et al* 2014).

4.3.2 Fullerenes

Water soluble fullerenes labeled with carbon-14 were administered orally to rats. Trace amounts of fullerenes were detected in liver and urine. Furthermore, 97% of the dose was excreted in the feces within 48 h, altogether suggesting poor oral absorption. (Yamago, Tokuyama *et al* 1995).

4.3.3 Gold

Correlative instrumental neutron activation analysis and TEM were used to quantitatively and qualitatively study the gastrointestinal uptake and biodistribution in mice of 4, 10, 28, and 58 nm metallic colloidal gold NPs following repeated oral exposure. The NPs were administered via drinking water ad libitum for 7 d at a concentration of approximately 200 mg/L. Electron microscopic studies 12 h post-exposure showed that the NP uptake occurred in the small intestine by persorption through single, degrading enterocytes in the process of being extruded from a villus. The gold levels in non-gastrointestinal tissues were higher, the smaller the NPs, indicating that smaller gold NPs cross the GI tract more readily. The amounts absorbed cannot be calculated from this study (Hillyer and Albrecht 2001).

Schleh *et al* administered radiolabeled gold NPs in different sizes by single intra-oesophageal instillations to adult female rats (1-27 µg/rat). The NP sizes studied were 1.4, 2.8, 5, 18, 80 and 200 nm with negative surface charge and 2.8 nm with positive surface charge. The amount of NPs in organs, tissues and excrements was measured after 24 h by gamma-spectroscopy. Overall, the systemic uptake was low, ranging from approximately 0.37% for the smallest to 0.01% for the largest NPs. The highest accumulation in secondary organs was generally found for 1.4 nm particles, the exception being the 18 nm NPs which showed a higher accumulation in brain and heart compared to the other sizes. Higher systemic uptake and tissue accumulation was seen for negatively charged compared to positively charged NPs of the same size. No general rule for accumulation could be made according to the authors (Schleh, Semmler-Behnke *et al* 2012).

4.3.4 Graphene oxide

Yang *et al* investigated the in vivo biodistribution of ^{125}I -labeled nanographene oxide (average size 500 nm, average thickness 1 nm) and three different labeled PEGylated nanographene oxides (average size 25-50 nm, average thickness 1-6 nm) in mice. The mice were sacrificed 4 and 24 h after oral dosing and 1 and 7 d after intraperitoneal (*ip*) dosing of 4/mg kg. The uptake and organ distribution were similar for the three

PEGylated graphene oxides after oral as well as *ip* dosing. At 4 h after the oral dosing, the bulk of the dose (10-20%) was found in stomach and intestine, whereas only a few per cent or less were detected in other organs. At 24 h post-dosing, the overall retained radioactivity was 2-3% of the dose, whereof around 1% in stomach and skin. Following *ip* injection on the other hand, the bulk of the dose (15-40%) was found in liver and spleen after both 1 and 7 d. The study indicates limited oral bioavailability of the four graphene oxides, however, the stability of the iodine labeling is unclear and quantitative data cannot be deduced from the paper (Yang, Gong *et al* 2013).

4.3.5 Iron oxide

A study primarily aimed at investigating the genotoxity of iron oxide NPs also investigated the biodistribution. Female rats were treated orally with single doses of 500, 1000, 2000 mg/kg bw of 30-nm or bulk iron oxide NPs. Iron was measured by AAS. The biodistribution of studied by measuring iron by AAS in liver, spleen, kidney, heart, brain, bone marrow, urine and feces at 6, 24, 48 and 72 h after treatment. The excretion of iron in urine and feces was proportional to dose at all time points. Further, in all tissues the concentration of iron increased over the background level in control animals. However, these increases were less than proportional to dose. This suggests capacity limited (saturated) uptake in the tissues. The absorbed amount of iron oxide NPs cannot be deduced from the study (Singh, Rahman *et al* 2013).

4.3.6 Polystyrene

Non-ionic and carboxylated fluorescent polystyrene microspheres (100, 500, 1000 and 3000 nm) were fed by gavage1.25 mg/kg bw and day for 10 d to female rats. Peyer's patches, villi, liver, lymph nodes and spleen of animals fed the non-ionic microspheres from 100 nm to 1 micron showed unequivocal evidence of uptake and translocation of the particles. Heart, kidney and lung showed no evidence of microspheres. The carboxylated microspheres were taken up to a lesser degree than the non-ionised ones. Experiments with 100 and 1000 nm microspheres radiolabeled with iodine-125 showed a higher uptake of the smaller particles, which were concentrated in gastro-intestinal tissues and liver. The particles were concentrated at the serosal side of the Peyer's patches and could be seen traversing the mesentery lymph vessels towards the lymph nodes (Jani, Halbert *et al* 1989).

The same authors made similar experiments while also expanding the size range by including 50 nm polystyrene microspheres. The absorption of the 50 and 100 nm microspheres was 34% and 26%, respectively, measured by determination of the polystyrene content). Approximately 7% (50 nm) and 4% (100 nm) of the absorbed dose was in the liver, spleen, blood and bone marrow. Particles larger than 100 nm did not reach the bone marrow, and those larger than 300 nm were absent from blood. No particles were detected in heart or lung tissue (Jani, Halbert *et al* 1990).

Female rats were dosed by gavage with 50 nm fluorescent polystyrene NPs for 5 d at a daily dose of 2.5 mg/kg bw. The percentages of administered dose taken up in different parts of the GI tract (measured by fluorescence microscopy 12 h after the final dose) were as follows: lymphoid small intestine 3.4%, non-lymphoid small intestine 2.3%, lymphoid large intestine 3.0% and non-lymphoid large intestine 2.2%. Approximately

60% of the polystyrene detected in the small intestinal tissue was recovered from the Peyer's patches, although the patches constitute much less than 1% of the area (Florence, Hillery *et al* 1995).

The biliary excretion of covalently linked fluorescence polystyrene microspheres of various diameters was investigated after a single dose of 12.5 mg/kg bw given by gavage to male rats. The recovery in bile as per cent of dose was 18% for the 50 nm, 8% for the 500 nm, and 1% for the 1000 nm and 0% for the 1000 nm microspheres. For comparison, about 36%, 16%, 3% and 1% of the dose were excreted in bile after *iv* injection. The amounts in blood were 9%, 1%, 0% and 0% after oral dosing, compared to 13%, 11%, 1% and 1% at 24 h after *iv* dosing. The study shows that biliary excretion plays an important role in the disposition of microspheres and that the biliary excretion is size-dependent. The blood levels suggest that at least the smaller microspheres are systemically absorbed to a large extent (Jani, Nomura *et al* 1996).

4.3.7 Selenium

Selenium NPs (red amorphous elemental selenium, stabilized with BSA, 19 nm) (Se) or an aqueous solution of sodium selenite dissolved in water was repeatedly given by gavage for 28 d to female rats at daily doses of 0.05 or 0.5 mg Se/kg bw. Selenium in tissues was determined by ICP-MS. In addition, elemental selenium was determined after addition of sulfite, and analysis of the resulting selenosulfate by anion exchange HPLC and ICP-MS. Elemental selenium was detected in liver, kidney and feces after administration of high doses of NPs as well as selenite. Selenium was also found in non-exposed control animals, but higher levels were attained in the high dose animals. According to the authors, this suggests that the natural metabolic pathways of selenium were exhausted at the high doses of NPs and selenite (Loeschner, Hadrup *et al* 2014).

4.3.8 Silica

The biodistribution of 110 nm fluorescent silica NPs was studied in mice after single *iv*, hypodermic, intramuscular injection and oral administration. The oral dose was 50 mg/kg bw. Silicon content was analyzed by ICP-OES. NPs in organs were also localized by fluorescence microscopy and by TEM. The authors claimed that the orally dosed NPs were absorbed, however, this was only supported by TEM imaging of liver at 24 h (and not at 7 d). The ICP-OES revealed no increases of silicon over control. The NPs were mainly excreted through urine and feces (Fu, Liu *et al* 2013).

Silica NPs (20 and 100 nm) were given orally to male and female rats at doses of 500 and 1000 mg/kg bw. The tissue distribution and excretion was studied by measurement of silicon in inner organs (1 h, 6 h, 1 d, 2 d, 3 d, and 7 d post-dosing) with the molybdenum blue method. Clearly elevated silicon levels (over background) were generally seen in liver and spleen, with no or marginal increases in brain kidney, lung and ovary/testis. There were no obvious dose- size- or sex-dependent differences in NP distribution. TEM and energy dispersive spectroscopy studies demonstrated almost intact NPs in liver and partially decomposed NPs with irregular morphology in kidney, especially in rats dosed with 20 nm NPs. Size-dependent excretion kinetics were apparent and the smaller 20 nm particles were found to be more rapidly eliminated than the larger 100 nm particles. The overall urinary and fecal excretion of silicon was 7-8%

and 75-79% of the dose, respectively, with no differences between doses, sizes or sexes. However, the fecal excretion of silicon in male rats occurred faster for the 20 nm compared to the 100 nm NPs presumably die to more rapid decomposition (Lee, Kim *et al* 2014).

4.3.9 Silicon

Bimbo *et al* studied the oral absorption and biodistribution in Wistar rats of thermally hydrocarbonized porous silicon NPs using NPs labeled with the short-lived fluoride isotope 18F (half-time 109.8 min) and PET imaging. The NP size was 97-188 nm, the oral dose was 0.2 mg, animals were sacrificed up to 6 h post-dosing. The investigators used NPs of three sizes, 97, 142 and 188 nm, but it is unclear which one was used in the oral study. To account for possible defluorination of the NPs, control animals were given radiolabeled sodium fluoride to establish the biodistribution of free fluoride. Negligible amounts of radioactivity were detected in the systemic circulation and in organs outside the GI tract, suggesting that the NPs did not cross the intestinal wall. 18F radioactivity appeared in bone and urine (corresponding to at most 0.4% of the dose) at later time points and was explained by the authors by minor detachment of the 18F -label, caused either by in vivo defluorination or NP disintegration. Autoradiography of the lower GI tract showed that most of the administered dose reached the distal parts of colon in 6 h and was excreted in fecal pellets (Bimbo, Sarparanta *et al* 2010).

4.3.10 Silver

The antibacterial effect of silver NPs has resulted in extensive use in various products. A complicating factor with regard to absorption and biokinetics is the dissolution of silver from the NPs and, hence the relation between ionic and particulate silver.

The 28-d oral toxicity of 60-nm silver NPs was investigated in rat according to the OECD test guideline. The daily doses were 0 (control) 30, 300 and 1000 mg/kg bw. Apart from conventional toxicological examination tissue silver levels were determined by AAS. All examined tissues (testis, kidney, liver, brain, lung, stomach, blood) from all groups exposed to silver NPs for 28 d showed clear dose dependent increase in silver. In addition, female rats hade two-fold higher silver levels than males in all dose groups. The distribution was dose-dependent in that the increases in tissue silver levels were less than proportional to dose in testis, brain and blood, and more than proportional to dose in liver and lung. This dose-dependency (not commented by the authors) may indicate saturation of phagocytic processes. However, the study presents no data on silver NPs in the tissues (Kim, Kim *et al* 2008).

The same investigators also conducted an oral 28-d study with F344 rats and 58-nm silver NPs at daily dose levels of 0, 30, 125 and 500 mg/kg bw. A similar dose-dependent biodistribution pattern was seen as in the previous study. However, the dose-corrected silver concentrations were generally 5-fold higher compared to Kim *et al* (Kim, Kim *et al* 2008), the exception being blood which had similar levels in the two studies. Further, female rats achieved higher concentrations than males not only in the kidney, but also in liver tissue (Kim, Song *et al* 2010).

Mice were administered silver NPs of four sizes (22, 42, 71 and 323 nm) by gavage in 14-d repeat-dose toxicity test at daily doses of 1 mg/kg bw. The distribution of silver

depended on the NPs so that, with some exceptions, the smaller the NP, the higher were the silver concentrations in the tissues. Silver concentrations in lysed tissues were determined by ICP-MS. The three smaller sizes of NPs were distributed to the organs including brain, lung, liver, kidney, and testis. This suggests a higher gastrointestinal bioavailability and/or more efficient translocation of the smaller NPs. The large-sized silver NPs (323nm) were not detected in any of the investigated tissues (brain, lung, liver, kidney, testis) (Park, Bae *et al* 2010).

The bioavailability, tissue distribution, time course in blood concentration, and excretion were investigated in rats after single *iv* (tail vein) and oral administration of 1 or 10 mg/kg bw of citrate-coated 7.9-nm silver NPs. Silver levels in blood were measured by ICP-MS. By comparing area under the concentration-time curves (AUC) following oral and *iv* dosing, the oral bioavailability was found to be 1.2% at the low dose and 4.25% at the high dose. The NPs mainly accumulated in the liver, with significant amounts also in lungs and kidneys. The levels in urine were extremely low. The amounts in liver and feces were approximately 50-fold elevated after the 10 mg compared to the 1 mg/kg *iv* dose, suggesting dose-dependent kinetics. NPs were detected in feces also after *iv* dosing, suggesting biliary excretion (Park, Park *et al* 2011).

Loeschner *et al* studied the biodistribution of 14-nm nanosilver and silver acetate in rats after 28 d of repeated oral administration of 9 mg/kg bodyweight. The NPs were stabilized with PVP. The fecal extraction of silver was higher and the concentrations in tissues were lower following oral exposure to NPs compared to silver acetate. The highest silver concentrations were seen in the intestinal system, liver and kidneys. However, silver was also found in the lungs and brain. Autometallographic staining revealed a similar cellular localization of silver in ileum, liver, and kidney tissue in rats exposed to NPs and silver acetate. Also, nanosized granules of similar composition (silver, selenium and sulfur) and size were detected by TEM and energy dispersive x-ray spectroscopy in the ileum after exposure to both NPs and acetate. No silver granules were detected in the liver. The presence of these granules suggests a common mechanism of formation. The authors concluded that additional studies are needed to understand the mechanisms of granule formation and to clarify whether the silver NPs dissolve in the GI tract and/or are absorbed and biodistributed as intact NPs (Loeschner, Hadrup *et al* 2011).

Rats were daily exposed for 28 d by gavage to silver free solution (control), silver nitrate (9 mg Ag/kg bw), <20 nm uncoated (average core size 18 nm, 90 mg Ag/kg bw), or <15 nm PVP-coated (average core size 12 nm, 90 mg Ag/kg bw). Silver concentration in organs was measured at 1 d, 1 wk and 8 wk post-dosing. For all exposures, silver was detected in all examined organs with the highest levels in liver and spleen, followed by testis, kidney, brain and lungs. The silver concentrations in the organs were highly correlated to the amount of silver ions in the NP suspensions, suggesting that mainly ions were absorbed in the GI tract. The silver was gradually cleared from all examined organs, except brain and testis, at 8 wk post-dosing. The retention was most prominent in brain, where the concentration remained more or less constant throughout the observation period (1 d – 8 wk post-dosing). Using single particle ICP-MS, silver NPs were detected not only in the NP-exposed exposed rats, but

also in rats exposed to silver nitrate, demonstrating the formation of NPs in vivo (van der Zande, Vandebriel *et al* 2012).

Blood levels, tissue distributions, and excretion of silver were measured in five male S-D rats up to 24 h after single oral doses of 2 or 20 mg/kg bw silver ions or citrate-capped silver NPs (average diameter 3.8 nm). Silver in serum was measured by ICP-MS after digestion with nitric acid. For both types of silver, silver in plasma increased less than proportional to dose, the 24-h AUC (µg•d/ml) being: 1.9 (ionic) and 1.2 (NP) after 2 mg/kg bw, *vs* 3.8 (ionic) and 1.6 (NP) after 20 mg/kg bw). Further, silver levels were seen in liver, kidneys, and lungs after administration of silver ions. The orally administered NPs were predominantly excreted through feces, suggesting low bioavailability (Park 2013).

S-D rats were exposed by gavage over 28 d to two types of silver NPs (average diameters 10 nm and 25 nm) at three dose levels, 0, 100 and 500 mg/kg bw. Silver NPs in tissues were measured by AAS at 0, 1, 2 and 4 months post-dosing. The silver content in studied tissues (blood, brain, kidney, liver, spleen, testis, ovary) gradually decreased during the 4-month recovery period. The half-times and mean residence times differed depending on organ, dose level and NP size. As the elimination curves were highly variable and often appeared to be biphasic, mean residence time was calculated as the AUMC/AUC ratio, where the AUMC is the first moment of the AUC. The longest mean residence times of about 2 months were seen in brain (both sexes) and testis. The shortest mean residence times of about 3-11 d were seen for blood. The authors concluded that the NP size did not affect the tissue distribution and that the blood-brain and blood-testis barriers seem to play an important role in the silver clearance (Lee, Kim *et al* 2013).

Blood levels, tissue distribution, and excretion of silver were measured by ICP-MS in male S-D rats up to 24 h after single oral administration of 8-nm silver NPs or silver ions at the same doses (2 or 20 mg Ag/kg bw). At the high dose, the concentration of silver in blood liver, kidneys and lungs was markedly higher after silver ion administration, compared to silver NP administration. The measurements and the low dose are difficult to interpret due to high background levels of silver in the control animals. Orally administered NPs were predominantly excreted through feces, suggesting low bioavailability (Park 2013).

4.3.11 Titanium dioxide

Suspended titanium dioxide (475±24 nm) particles were given by gavage for 10 d at daily doses of 12.5 mg/kg bw to female S-D rats. A variety of tissues were examined for histopathological effects, presence of particles by SEM and presence of titanium by ICP-MS. The largest particle amounts were found in the colon (4.5% of the administered dose), Peyer's patches (2.8%), liver (2.3%), lungs (1.2%), peritoneum (0.7%) and small intestine (0.1%). The titanium dioxide particles were present in all major gut associated lymphoid tissues. They were not detected in heart and kidney (Jani, Mccarthy *et al* 1994).

In a study designed to evaluate the acute toxicity of titanium dioxide NPs, adult mice were given a single dose of NP suspension (5g/kg bw). The biodistribution was studied

by determination of titanium in tissues by ICP-MS. These experiments showed that the NPs were mainly retained in the liver, spleen, kidneys, and lung tissues, indicating uptake by the GI tract followed by transport to other tissues and organs. The NPs mainly accumulated in the liver and a 40-fold higher amount was detected after administration of 80-nm compared to 25-nm titanium dioxide NPs (Wang, Zhou *et al* 2007).

In a comparative toxicity study of titanium dioxide NPs, 3- and 8-wk old S-D rats were given 0, 10, 50 or 200 mg NP/kg bw and day for 30 d by oral gavage Although different different toxic effects were seen in young and adult rats, no age differences in biodistribution were detected in the high dose groups. Thus, TEM images showed that some NPs were adhered to the intestinal villi and absorbed in the stomach and small intestine tissue. However, no NPs were found in the liver of neither young, nor adult, rats. Furthermore, the titanium concentrations in blood, liver, kidney and spleen of the NP-treated young and adult rats (measured by ICP-MS and ICP-OES) were not significantly different from that measured in untreated animals (Wang, Chen *et al* 2013).

The tissue distribution and blood kinetics of various titanium dioxide NPs (NM-100, 101, 102, 103, and 104), which differ with respect to primary particle size, crystalline form and hydrophobicity, were investigated in rats up to 90 d post-exposure after daily repeated oral administration (2.3 mg TiO_2/animal/d for 5 d). The agglomerate/aggregate sizes were in the range 50-200 nm. Liver, spleen and mesenteric lymph nodes were sampled for titanium analysis high-resolution ICP-MS. Titanium was only sporadically detected (detection limit 0.03 µg/g tissue) in liver and spleen in some rats. Titanium could be detected at low levels in mesenteric lymph nodes. These results indicate that some minor absorption occurs in the GI tract, but to a very limited extent. Overall, the results indicates very low oral bioavailability and slow tissue elimination (Geraets, Oomen *et al* 2014).

Male S-D rats were given a single oral dose of 100 mg/kg bw titanium dioxide NPs (18 nm) by gavage. Tissues sampled at 24 h after dosing were examined for titanium by ICP-MS and for particles by TEM. There was no statistically significant increase in titanium in any tissue. In contrast, considerable amounts of NP aggregates were observed in at least one cell (freely distributed in the cytoplasm) from a Peyer's patch section of the ileum (Janer, Mas del Molino *et al* 2014).

The comparative absorption, distribution, and excretion patterns of titanium dioxide (26 nm, 260, 521 and 1042 mg/kg bw) and zinc oxide (89 nm, 134, 268 and 537 mg/kg bw) NPs following oral administration were evaluated in rats. The NPs were given orally by gavage once daily for 13 wk (7 d/wk). Blood, liver, kidney, spleen, brain, urine and feces were obtained at necropsy and titanium and zinc was measured by ICP-MS. The titanium dioxide NPs had an extremely low absorption, thus the titanium levels were very high in feces but not significantly increased compared to non-exposed control animals in the sampled organs and urine even in the rats given the highest dose. In contrast, zinc was clearly increased compared to control in liver, kidney and urine, and minimally increased in spleen and brain. The higher absorption of the zinc oxide NPs might be due to their dissolution in the acidic gastric fluid (Cho, Kang *et al* 2013).

4.3.12 Zinc oxide

A complicating factor with regard to the absorption and biokinetics is the dissolution of zinc oxide from the NPs and, hence the relation between ionic and particulate zinc.

In a study aimed to investigate the acute oral toxicity of 20- and 120-nm zinc oxide NPs, the distribution of zinc in serum and organs following a single oral dose of 5 g/kg bw was studied by ICP-MS. For both NP sizes, the zinc levels were significantly elevated in bone, kidney and pancreas. For serum, liver and heart, the zinc levels in treated animals were not different from controls. The total recovery in the tissues was not reported but judging from the increases in zinc levels, the systemic absorption appeared to be extremely low (less than 0.01%). The absorption of NPs is difficult to assess, since the zinc oxide dissolves in gastric fluid (Wang, Feng *et al* 2008).

Male ICR mice were given a single oral dose of 2500 mg/kg zinc oxide NPs (average diameter 50 nm, hydrodynamic diameter 93 nm) or microparticles (at least one dimension >100 nm, hydrodynamic diameter 1226 nm) and sacrificed up to 72 h post-dosing. Serum and tissue samples were analyzed for zinc by ICP-MS. Increased zinc levels in serum were found already after 30 min post-dosing with maxima of 18 and 15 µg/g for NP- and microparticle-treated mice, respectively, occurring after 2 h. Serum zinc level began to decrease after 6 h and returned to the baseline after 48 h (Li, Shen *et al* 2011).

Lee *et al* investigated the biodistribution of orally administered 20 nm and 100 nm Cy5.5-conjugated zinc oxide NPs (250 mg/kg) in rats using optical imaging. Cy5.5 is a near infrared fluorescent dye. The zinc oxide NPs were chemically modified by conjugation with a monoreactive hydroxysuccinimide (NHS) ester of Cy5.5. The conjugated NPs were stable in simulated gastric fluid for 7 h. Blood sampling and optical imaging studies were performed up to 7 h after dosing. Most of the zinc oxide particles were excreted via the feces, with some absorbed into the blood and distributed to the organs. The 20 nm NPs showed faster passage from the stomach to the GI tract and absorption into the blood than the 100 nm NPs. The signal intensity of NHS NPs in blood peaked earlier (3 h after dosing) than that of plain Cy5.5 NPs (5-7 h). Seven hours following administration, the NHS NPs accumulated in the lung and liver, and the plain ones in the kidney and liver (Lee, Jeong *et al* 2012).

In a study exploring the NP size-dependence of biokinetics, 20- and 70-nm zinc oxide NPs were given as single oral doses of 50, 300 or 2000 mg/kg bw to male and female rats. The plasma AUC, tissue distribution, excretion, and the fate of the NPs in organs were analyzed by ICP-AES and TEM. For both NP sizes, zinc in plasma increased during the 24 h after administration in a dose-dependent manner. The systemic absorption, calculated from the plasma AUC, seemed to increase with dose (6-18% at the low dose *vs*. 28-33% at the high dose). Significantly increased zinc levels were detected in kidney, liver, and lung within 6-24 h at the two lower doses, followed by a decrease in zinc levels, suggesting rapid distribution and no accumulation in these tissues. In contrast, zinc levels peaked in lung, liver, and kidney after 1-3 d after the high dose. These observations are consistent with the estimated mean residence times of 2-7 h, -12 h, and 32-39 h, respectively after the low, medium, and high dose. The NPs were mainly excreted via the feces (49-97% of the dose), whereas only a small amount

(0.3-1.5%) was excreted via urine. Overall, the study indicates that the biokinetics of zinc oxide NPs is dose-dependent with no clear dependence of NP size and gender (Baek, Chung *et al* 2012).

The biodistribution and clearance of zinc oxide NPs (50 nm, hydrodynamic diameter 94 nm) and microparticles (at least one dimension >100 nm, average 1200 nm) (ZnO-NPs) were followed by ICP-MS in male mice up to 72 h after single oral (gavage) and *ip* doses of 2.5 g/kg bw. The highest NP and microparticle concentrations were found in liver, followed by spleen, lung, kidney, and heart. Judged by the time courses in blood and organs, the NPs were more efficiently absorbed via both dosage routes than were the microparticles. No quantitative conclusions can be drawn regarding the absorption (Li, Shen *et al* 2012).

Lee *et al* investigated the biokinetics in female mice of 20- and 100-nm zinc oxide NPs after oral administration of 250 mg/kg bw. To follow the particles, the investigators used alkyne modified particles that were click labeled with 18F-etoxy azide. The PET imaging revealed the radioactivity from 18F-labeled particles was seen only in the GI tract, whereas administration of 18F or 18F-ethoxy azide resulted in radioactivity in the bone and bladder 3 h after dosing. After 5 h, the fluoride was almost exclusively found in bone (10% of the dose, calculated from Figure 8 in (Lee, Jeong *et al* 2012), corresponds to approximately 18% of the administered dose), whereas ethoxy azide was more evenly distributed to the tissues. The smaller 18F-NPs exhibited a biodistribution similar to that of 8F, albeit with approximately 10-fold lower tissue levels relative to dose. In contrast, the larger NPs showed a vast preference for kidney tissue (7% corresponding to 2% of the dose). The absorption of the 20- and 70-nm NPs can be estimated to 1.8% and 18%, respectively, of the given dose (estimated from Figure 8) (Lee, Jeong *et al* 2012).

The influences of particle size (20 nm and 70 nm) and surface charge (negative and positive) on the biokinetics of zinc oxide NPs were examined in rats by following the time course of zinc in plasma and organs (brain, blood, kidney, liver, lung, spleen, testis, ovary) after single oral (50, 300 and 2000 mg/kg bw) or *iv* (20 mg/kg bw) doses of the different NPs. Positively and negatively charged NPs were prepared by treating pristine zinc oxide NPs with L-serine and sodium citrate, respectively. The biokinetic profiles and biodistribution (measured with ICP-AES) were not affected by particle size or gender. However, the positive NPs (84-93% of the oral dose excreted via feces, 0.3-1.4% via urine) were more efficiently absorbed by the systemic circulation than the negative NPs. Based on AUC in plasma, 6-33% of the administered negative and 10-17% of the administered positive NPs reached the systemic circulation. There was no obvious relation between absorption and gender, dose or NP size. According to the authors, the results suggest that surface charge, rather than size, gender or dose, determines the absorption. It should be noted that these calculations were based on zinc (and not NP) measurements after subtracting background levels in control animals. By comparing the concentration time courses of zinc in the tissues following *iv* dosing with those after oral dosing and the identification of NPs by TEM imaging, the authors concluded that the biodistribution of zinc is mainly determined by the ionic and not the particulate form and that it is independent of exposure route (oral or *iv*). The particle size only affected the excretion, where the 20-nm NPs were more rapidly eliminated.

Most NPs were excreted via the biliary and fecal routes, but a small amount of the NPs was excreted via urine. The study suggests that surface charge, rather than particle size or gender, determines the biokinetic behavior of zinc oxide NPs (Paek, Lee *et al* 2013).

The biokinetics of uncoated (29 nm) and silicone oxide coated (28 nm + 4.5 nm coating) neutron activated 65zinc oxide NPs was followed in rats after oral administration of 5 mg/kg bw and after it instillation (see section Intratracheal administration). Tissue samples were analyzed for 65Zn radioactivity at 2, and 7 d after dosing. At 7 d post-dosing, 7.4% (uncoated) and 6.7% (coated) of the dose were recovered in all tissues combined. As with instilled NPs (see later chapter), significantly more 65Zn was measured in skeletal muscle (6.5% *vs* 0.2% of dose), but less in thoracic lymph nodes (0.02% *vs* 0.06%) and urine (0.07% *vs* 0.12%) after dosing with uncoated compared to coated NPs (Konduru, Murdaugh *et al* 2014).

4.4 Conclusions – oral absorption

Overall, 24 studies addressing the oral absorption of NPs were examined. Various types of NPs with respect to composition and size have been studied in mice and rats. Considerable uptake of NPs was demonstrated in vitro with cultured cells (Win and Feng 2005; Bouwmeester, Poortman *et al* 2011) and with isolated rat intestine (Sonavane, Tomoda *et al* 2008; Sinnecker, Krause *et al* 2014), however, extrapolation of these to the situation in vivo is difficult.

A few in vivo rat and mouse studies report quantitative data on oral absorption, summarized in Table 3. A number of other in vivo studies present data suggesting high to low oral absorption (Jani, Mccarthy *et al* 1994; Hillyer and Albrecht 2001; Wang, Zhou *et al* 2007; Park, Park *et al* 2009; Singh, Rahman *et al* 2013; Yang, Gong *et al* 2013; Geraets, Oomen *et al* 2014). Studies conducted with silver and zinc oxide NPs are not useful to assess the absorption of NPs per se, due to significant dissolution and formation of metal ions in gastric juice. Several studies could not demonstrate any oral absorption, *ie* no increase in NP levels in tissues, while one study with gold NPs showed 0.03-0.37% size- and charge-dependent uptake, with higher uptake for the smaller NPs (Schleh, Semmler-Behnke *et al* 2012). On the other hand single studies with polystyrene (Jani, Nomura *et al* 1996), silica (Lee, Kim *et al* 2014) and titanium dioxide (Jani, Mccarthy *et al* 1994) microparticles suggest oral uptake of several per cent of the administered dose.

Table 3. Summary of quantitative animal data on oral absorption of nanoparticles.

Nano-particle	Size, nm	Zeta potential	Oral dose (mg/kgbw)	Species	Systemically absorbed(% of dose)	Reference
Gold	1.4 2.8 2.8 5 18 80 200	– – + – – – –	1 μg 1.4 μg 16.4 μg 27.4 μg 2.4 μg 19.9 μg 19 μg	Rat	0.37% 0.37% 0.14% 0.05% 0.12% 0.03% 0.1%	Schleh, Semmler-Behnke *et al* 2012
Polystyrene	59 540 1044	–	12.5	Rat	18% in bile, 9% in blood 8% in bile, 1% in blood 1% in bile, 0% in blood	Jani, Nomura *et al* 1996
Silica	20, 100 20, 100	–	500 1000	Rat	7-8% in urine in 10 d	Lee, Kim *et al* 2014
Silver	7.9	–	1 10	Rat	1.2% 4.25%	Park, Park *et al* 2011
Titanium dioxide	475	–	12.5, daily for 10 d	Rat	4.3% sum of amounts in major non-GI organs	Jani, Mccarthy *et al* 1994
Zinc oxide	20 70	–	50, 300, 2000	Rat	6-18% at low dose 28-33% at high dose	Baek, Chung *et al* 2012
Zinc oxide	20 100	Not stated	25	Rat	1.8% 18%	Lee, Jeong *et al* 2012
Zinc oxide	20, 70 20, 70	– +	50, 300, 2000	Rat	6-33% 10-17%	Paek, Lee *et al* 2013

5 Inhalation exposure

5.1 In vitro studies

5.1.1 Quantum dots

Chau *et al* studied the influence of physicochemical properties on paracellular permeability of QDs across a monolayer of primary human bronchial epithelial cells in an ALI system. QD localization was determined by immunofluorescence and TEM. The fluorescence imaging showed that, within 5 min, positively charged QDs were localized in the cells, whereas negatively charged QDs were localized between cells. At 30 min, the basal medium expressed higher fluorescence after exposure to positive than after exposure to negative QDs; however, the fluorescence was independent of dose. At 4 h after exposure, the fluorescence intensities increased with dose and were similar for the two types of QDs. The authors interpreted these findings as a high paracellular epithelial storage capacity for negatively charged QDs, resulting in a delayed transport into the basal medium (Chau, Galloway *et al* 2013).

5.2 In vivo studies

5.2.1 Aluminosilicate

Snipes *et al* studied the retention of inhaled aluminosilicate particles in dogs, rats, and mice. The animals were briefly exposed to polydisperse (1,5-2 μm) or monodisperse (0.7-, 1.5-, or 2.8 μm) aluminosilicate particles fused with cesium-134. Cesium levels in the dogs were followed up to 850 d post-exposure by whole-body liquid scintillation counting. Cesium in organs (mice and rats) and feces (all three species) were measured using the same liquid scintillation system. In dogs, solubilization was the dominant factor in lung clearance; mechanical clearance was dominant in rats and mice. After accounting for solubility, physical clearance from the lung to the GI tract and to lung-associated lymph nodes (LALNs) was independent of particle size within the investigated size range. The clearance of particles from the lung was rapid in rats and mice and much slower in dogs. A small portion of the initial deposit was retained in the upper respiratory tract of all three species (Snipes, Boecker *et al* 1983).

5.2.2 Aluminum oxyhydroxides

Pauluhn studied the lung kinetics and dynamics of inhalation exposure (6h/d, 5 d/wk, 4 wk, nose-only) of rats to two sizes of aluminum oxyhydroxides (Boehmite, primary size 10 nm, agglomerated size 1.7 μm, and 40 nm agglomerated size 0.6 μm) and to synthetic iron oxide black (Magnetite, primary size 300-600 nm, agglomerate sixe 1.5 μm). Three dose metrics (inhaled mass, inhaled surface area, mass-based lung burden) were compared with the pulmonary inflammation characterized by broncho alveolar lavage. The pulmonary inflammation corresponded better with inhaled mass than with inhaled surface area or body burden mass. The 0.6 μm particles resulted in a higher dose than the 1-2 μm particles (Pauluhn 2009).

5.2.3 Cadmium chloride

Cassee *et al* exposed rats nose-only to soluble cadmium chloride aerosols with different particle sizes (33, 170, 637 or 1495 nm) but at similar mass concentrations (1.43 – 0.63 mg/m^3). The measured deposition of cadmium in the respiratory tract correlated well with the masses predicted with a lung deposition model (MPPDep V1.1). The deposited mass, in turn, depended on the aerodynamic diameter, thus, the smaller the particles, the higher the lung deposition. Cadmium levels in tissues other than the respiratory tract were only minimally elevated (Cassee, Muijser *et al* 2002).

5.2.4 Carbon

Five healthy volunteers inhaled 3-5 breaths of Technegas, an aerosol consisting mainly of ultrafine ^{99m}Tc -labeled carbon particles (<100 nm). Most NPs were 5-10 nm in size, however, larger particles as well as aggregates were also seen by SEM. Radioactivity was detected in blood already after 1 min, reached a maximum at 10-20 min, and remained at this level up to 60 min. Gamma camera images showed substantial radioactivity over the liver and other areas of the body. The authors concluded that the inhaled ^{99m}Tc -labeled carbon NPs pass rapidly into blood (Nemmar, Hoet *et al* 2002).

Brown *et al* studied the deposition and clearance of an ultrafine ^{99m}Tc -labeled carbon aerosol (64 nm, 10 µg/m^3) in 10 patients with chronic obstructive pulmonary disease (COPD) and in 9 healthy subjects. The particle retention was followed by gamma scintigraphy for 2 h after inhalation and again after 24 h. Particle accumulation in the liver was examined by quantifying activity below the right lung. Patients had a significantly greater dose rate than healthy subjects (2.9 *vs* 1.9 µg/h), likely explained by a higher tidal ventilation in BW patients. Central-to-peripheral ratios of the thorax measurements were slightly greater in patients, a sign of a more turbulent air flow, than in healthy subjects. There were no differences in particle clearance between the two groups. The average 24-h retention was 85%. No accumulation in the liver (gamma activity below the right lung) could be demonstrated (Brown, Zeman *et al* 2002).

Fischer 344 rats were exposed to carbon-13 NPs (20-29 nm) for 6 h in whole-body inhalation chambers at concentrations of 180 and 80 µg/m^3 and killed at 0.5, 18, and 24 h post-exposure. ^{13}C levels were determined by isotope ratio mass spectroscopy and compared to background levels of sham-exposed rats. The ^{13}C retained in the lung at 0.5 h post-exposure was about 70% less than predicted by rat deposition models for ultrafine particles, and did not change during the 24-h post-exposure period. Significant amounts of ^{13}C had accumulated in the liver at 0.5 h after the high exposure, at 18 h and 24 h ^{13}C was elevated in livers of all exposed rats and was approximately fivefold greater than that in the lung. No significant increase in ^{13}C was detected in the other examined organs (heart, brain, olfactory bulb, and kidney). The authors concluded that the translocation of carbon to the liver occurs not only via direct input from the respiratory tract to blood but also via the GI tract and that such translocation may differ between carbon and other insoluble (metal) NPs (Oberdörster, Sharp *et al* 2002).

Oberdörster *et al* further examined whether translocation of inhaled NPs to the brain takes place via the olfactory mucosa and olfactory nerve into the olfactory bulb. Rats were exposed in a whole-body exposure chamber to 160 µg/m^3 of elemental carbon-13

NPs (generated by electric spark discharge in argon) for 6 h. Lungs, cerebrum, cerebellum and olfactory bulbs were removed at 1, 3, 5, and 7 d after exposure and ^{13}C levels were determined in lung, cerebrum, cerebellum and olfactory bulb by isotope ratio mass spectrometry. Lung ^{13}C decreased from 1.4 µg/g day 1 to 0.6 µg/g day 7 post-exposure. The ^{13}C level (corrected for background in non-exposed rats) increased significantly and persistently in the olfactory bulb, reaching 0.35 and 0.43 µg/g on days 1 and 7, respectively. The day 1 levels in cerebrum and cerebellum were also significantly increased but did not persist, possibly reflecting translocation across the blood-brain barrier in certain brain regions. The authors stated that, depending on particle size, over 50% of inhaled ultrafine particles can be deposited in the nasopharyngeal region during nasal breathing. They further estimated that approximately 20% of the particles deposited on the olfactory mucosa of the rat can be translocated to the olfactory bulb, thus circumventing the blood-brain barrier (Oberdörster, Sharp *et al* 2004).

Nine healthy subjects and four asthmatics inhaled 30 l of a ^{99m}Tc -labeled carbon NP aerosol (37 nm) for approximately 7 min. The pulmonary retention was followed for 24 h by gamma camera imaging. There were no significant differences between healthy and asthmatic subjects in any of the parameters studied. Particle retention after 24 h was 102%. The 24-h in vitro leaching of radioactivity from the particles was 1.7%. In blood, 1.1% of the initially deposited activity was detected at 80 min post-exposure, 91% of this activity was not bound to particles. The cumulative 24-h excretion in urine was 3.6%. The gamma camera images showed that activity translocated from the lungs to the thyroid and the GI tract. The authors concluded that there was no significant translocation of the inhaled NPs to the systemic circulation (Wiebert, Sanchez-Crespo *et al* 2006).

The same group exposed 15 healthy subjects to ^{99m}Tc-labeled carbon NPs (100 nm). The radioactivity over the lung was followed for 70 h. The clearance of these ultrafine particles from the lungs and specifically translocation to the circulation was tested. The average lung retention at 46 h was 99% of the deposited amount. The 70-h cumulative leaching of ^{99m}Tc activity from the NPs was 2.6%. The 24-h activity leaching in urine was 1.0%. According to the authors, it is unclear if the cleared activity of approximately 1% is due to leached activity or translocation of NPs (Wiebert, Sanchez-Crespo *et al* 2006).

Kreyling *et al* exposed anesthetized rats to iridium and carbon NPs radiolabeled with ^{192}Ir for 1 h via intubation. The inhaled NPs were chain aggregates and agglomerates, with primary particle sizes of 2-4 nm (iridium) and 5-10 nm (carbon) and aggregate sizes (mean mobility diameters) of 20-80 nm. The aggregates contained less than 1% iridium. Iridium was detected in liver, spleen, kidneys, heart, brain and remaining carcass. The recoveries after 24 h of the larger NPs (80 nm iridium and 25-nm carbon) in each of blood, brain, heart, kidney, liver and spleen corresponded to 0.03-0.16% of the deposited dose (estimated from figure 4 in (Kreyling, Semmler-Behnke *et al* 2009). In contrast, the amounts of the 20-nm iridium NPs were approximately tenfold higher than the 80-nm ones (blood 1.9% *vs* 0.1%, other tissues 0.2-0.3% *vs* 0.03-0.06%), showing that the 20-nm NPs were translocated to a higher extent than the 80-nm NPs (Kreyling, Semmler-Behnke *et al* 2009).

5.2.5 Cerium oxide

Blood and tissue biokinetics were investigated in rats during and after 28 d of inhalation exposure (6 h/d, nose-only) to three types of cerium oxide particles (55, 20 and 11 mg/m^3; nominal primary particle sizes: < 5000, 40, and 5-10 nm; by TEM: >500, 27 and 13 nm; by SEM 615, 28 and 45 nm; mean aerodynamic diameter MMAD: 1.4, 1.17 and 1.02 µm). After a single exposure, approximately 10% of the inhaled dose was measured in lung tissue; similar percentages were also estimated by multiple path particle dosimetry (MPPD) modeling. Elevated cerium oxide levels were observed in liver, kidney, spleen, brain, testis, and epididymis after a single in 6-h inhalation exposure, and the 28-d repeated exposure to cerium oxide resulted in significant accumulation of the particles in the extrapulmonary tissues. Furthermore, tissue clearance was slow and insignificant amounts of cerium oxide were eliminated from the body at 48 h and 72 h after exposure. No clear effects of the primary particle size or surface area on the pulmonary deposition and extrapulmonary tissue distribution were seen. According to the authors, this is most likely explained by similar aerodynamic diameter of the cerium oxide particles in air because of the formation of aggregates (Geraets, Oomen *et al* 2012).

Male CD1 mice were exposed 6 h/d nose-only to 2 mg/m^3 of cerium oxide NPs (15-30 nm) for 0, 7, 14 or 28 d with 14 or 28 d of post-exposure recovery. ICP-OES results showed a bioaccumulation of NPs not only in lungs (1200 mg/g tissue at 28 d post-exposure) but also small but significant levels in liver (0.6 mg/g), kidney (0.8 mg/g), heart (0.6 mg/g) and brain (0.3 mg/g) (Aalapati, Ganapathy *et al* 2014).

Keller *et al* had female Wistar rats inhale aerosols of cerium oxide NPs (4-15 nm and 40 nm, MMAD 0.9-2.2 µm, 0.5, 5, and 25 mg/m^3, whole-body) for 6 h/d on 5 consecutive days for 1 wk or 4 wk with a post-exposure periods of 24 d or 129 d, respectively. Cerium in lungs was analysed by ICP-MS or ICP-OES. The NPs were cleared from the lungs with a half-time of 40 days (rats exposed for 4 wk), however, at the two higher exposures the clearance was 0 was impaired and the half-time after the highest exposure was above 200 d (Keller, Wohlleben *et al* 2014).

5.2.6 Gold

Male rats were exposed to 88 µg/m^3 spherical gold NPs (5-8 nm) in a whole-body exposure chamber for up to 7 d. Gold in lung, lavage fluid and blood was measured by ICP-MS. A large portion of the deposited gold NPs was retained in the lung and 1.9 and 1.5 µg were detected on days 0 and 7 post-exposure. Gold particles in tissues were individual or slightly agglomerated. In the lavage fluid, 0.6 and 0.1 µg were detected, corresponding to 29% and 6%, respectively, of the lung burden. A low but significant increase of gold (0.03 to 0.06% of lung concentration) was found in the blood. Small vesicles containing gold particles were found in the cytoplasm of alveolar macrophages and in the cytoplasm of alveolar type I epithelial cells. These findings indicate that the gold NPs are processed by endocytotic pathways, though the uptake of the gold particles by alveolar macrophages is limited (Takenaka, Karg *et al* 2006).

Male rats were exposed to gold NPs (> 75% of between 30 and 110 nm) for 15 d in a whole-body exposure chamber. Significant increases of gold in lung and olfactory bulb

were detected by ICP-MS after 5 d and lung, esophagus, tongue, kidney, aorta, spleen, septum, heart and blood after 15 d. The tissues levels at 15 d were generally 3% or lower of that in lung, exceptions being tongue and oesophagus (9%), aorta and spleen (6%), kidney (5%) and heart (4%). The concentration in the olfactory increased 3-fold above background at 5 d (6% of concentration in lung) with no further increase after 15 d (2%) (Yu, Yung *et al* 2007). The author do not state whether measures were taken to avoid secondary exposure due to *eg* licking the fur.

S-D rats of both sexes were exposed to 0, 0.04, 0.38 or 20 µg/m^3 of gold NPs (4-5 nm) for 90 d (6 h/d, 5 d/wk) in a whole-body inhalation chamber. Gold in tissues was measured by AAS. The gold content in lung was markedly increased over background levels. A significant increase was also seen in kidney after the highest exposure (43 ng/g *vs* 19 ng/g in control animals) but not in blood, brain, liver or olfactory bulb (Sung, Ji *et al* 2011).

Balasubramanian *et al* studied the biodistribution of two gold NP types with similar size distribution and number concentration, but different primary diameters of 7 nm or 20 nm. Gold in tissues were measured by ICP-MS after microwave-assisted acid digestion. Fifteen days of whole-body exposure (6 h/d, 3 wk, exposure levels 86 µg/m^3 (7 nm) and 53 µg/m^3 (20 nm)) of male Wistar rats to agglomerates of the smaller NPs resulted in highest deposition in lungs, followed by brain regions including the olfactory bulb, hippocampus, striatum, frontal cortex, entorhinal cortex, septum, cerebellum; aorta, esophagus, and kidney. Eight organs, especially brain, reached higher gold concentrations after exposure to the 7-nm, compared to the 20-nm NPs. However, concentrations were still low and generally below 1% of that measured in lung. The amount of gold excreted in feces was 5-50 times higher than that translocated to secondary organs, supporting that the clearance of the gold NPs from the lungs occurs mainly via macrophage-mediated transport to the airways and mucociliary escalation to larynx and pharynx, followed by swallowing and transport through the GI tract. The fraction of lung deposited gold NPs translocated to other tissues was 1.4% for the 7-nm compared to 0.2% for the 20-nm NPs, supporting that smaller particles can more easily cross the air-blood barrier in the lungs. (Balasubramanian, Poh *et al* 2013). The paper does not indicate if measures were taken to exclude secondary exposure via ingestion.

Female mice were exposed via intubation to radioactively labeled gold NPs for 2 h. One group of mice were given 10 µg of pulmonary surfactant protein D by it instillation prior to the NP exposure. The highest amount of gold NP was associated with the lung tissue. A high fraction, 57.5%, of the lung-deposited NPs was associated with the lung tissue directly after the 2-h exposure. Furthermore, 1.2% was detected beyond the air-blood barrier. The authors excluded the possibility of secondary uptake via the GI tract, due to the short exposure time and the limited amount of NPs (3.6%) in the GI tract. Pretreatment with surfactant protein D had no significant effect on the biodistribution of the gold NPs (Schleh, Holzwarth *et al* 2013).

S-D rats were exposed nose-only to 13-nm (12.8 µg/m^3) and 105-nm (13.7 µg/m^3) gold NPs for 5 d (6 h/d), followed by a recovery period of 1, 3, and 28 d in fresh air. Tissue gold was determined by ICP-MS following microwave-assisted acid digestion. NP of both sizes deposited mainly in lungs. While the larger NPs were only found in the

blood, the smaller NPs were detected in the liver, spleen, brain, testes, and blood. Still, the levels in these tissues were generally less than 1% of that measured in lung. Further, the elimination half-time from the lungs was significantly shorter for the smaller (45 d) than the larger (180 d) NPs (Han, Lee *et al* 2015).

5.2.7 Iridium

Anesthetized male Wistar Kyoto rats were exposed for 1 h to ^{192}Ir NPs (15 and 80 nm) via an endotracheal tube. Biodistribution and clearance by excretion was followed for 1 wk by gamma spectroscopy. The thoracically deposited fractions were 49% for the 15-nm and 28% for the 80-nm NPs. The NPs were predominantly cleared to the GI tract and feces and already 6 h after inhalation 18% and 10%, respectively, of the lung deposited doses were already cleared into the GI tract. Only 2% was cleared via urine up to 7 d after exposure and less than 1% was translocated to secondary organs such as liver, spleen, heart, and brain. The recovery during the 7 d accounted for 0.3-0.5% for the 15-nm and 0.6-0.8% for the 80-nm NPs. The particle dissolution was below 1% in 7 d. Instillation experiments with soluble iridium chloride performed in parallel suggested that almost all ^{192}Ir found in the tissues after the NP exposure was particulate and not ionic (Kreyling, Semmler *et al* 2002).

Semmler *et al* studied the lung retention and clearance kinetics in male Wistar Kyoto rats up to 6 months after 1-15 h inhalation exposures to ^{192}Ir NPs (15-20 nm, deposited dose 11.2 µg). The anesthetized animals were exposed via endotracheal intubation. Whole-body retention was followed by external gamma counting, and particle clearance kinetics was determined by excretion radio analysis. The biggest fraction was retained in the lungs (26% after 3 wk, 15% after 2 months and 6% after 6 months). The extrapulmonary tissue levels peaked after 1 wk (liver and kidneys 0.6%, spleen 0.4% and brain 0.3% of the lung deposited dose) and then quickly returned to low levels (Semmler, Seitz *et al* 2004).

The same group also studied the lung clearance of larger ^{192}Ir NPs (0.7 mg/m^3) in Wistar Kyoto rats over 6 months after single it inhalation exposures (60-100 min). Directly after inhalation free NPs were detected in BAL; later the NPs were predominantly associated with alveolar macrophages and after 3 wk, the lavageable fractions decreased to 6% of the actual NP lung burden, whereas 80% was translocated into epithelium and interstitium. The authors concluded that NPs are much less phagocytized by alveolar macrophages than larges particles but are effectively removed from the lung surface into the interstitium (Semmler-Behnke, Takenaka *et al* 2007).

(Kreyling, Semmler-Behnke *et al* 2009) exposed anesthetized rats to ^{192}Ir NPs and ^{192}Ir-labeled carbon NPs for 1 h via intubation. The study is described elsewhere (see section on Carbon above).

Geiser *et al* exposed wild type and chloride channel defective Cftr (model for cystic fibrosis) mice to 30-nm ^{192}Ir NPs for 1 h by it inhalation. NP biokinetics was deduced from total and regional lung deposition and from whole body translocation as measured by gamma spectrometry at 24 h after the aerosol inhalation. About 10% and 40% of the estimated total amount inhaled were deposited in the head region and the lungs, respectively, immediately after exposure. After 24 h, about 40% of the lung deposited

dose had been cleared and 60% remainder in the lungs. Iridium was also detected in trachea (0.05% of the inhaled dose), heart (0.01%), skin (5%), liver (0.01%), kidneys (0.01%), GI tract (4%), head (0.1%), brain (0.01%), remainder of body (0.1%), urine (0.02%) and feces (41%). These values were estimated from figure 5 in Geiser *et al* (Geiser, Stoeger *et al* 2014). There were no significant differences in the organ biodistribution between the two types of mice.

5.2.8 Iron

Mice were exposed nose-only to 50-nm fluorescent PVP-stabilized magnetic ferrite NPs (4 h/d, 5 d/wk for 4 wk). The distribution was studied by MRI and confocal laser scanning microscopy (CLSM). The image intensities revealed presence of NPs identified in various organs, including brain, lung, heart, liver, spleen, kidney, testis and ovary liver (Kwon, Hwang *et al* 2008).

5.2.9 Manganese oxide

Rats were exposed nose-only via one or both nostrils to 500 µg/m^3 of 30-nm manganese oxide NPs for 12 d (6 h/d, 5 d/wk for 2 wk). Manganese concentrations in the olfactory bulb, measured by AAS, increased 3.5-fold whereas concentrations in lung doubled. There were also increase concentrations in striatum, frontal cortex, and cerebellum. With the right nostril occluded during 2 d of exposure, manganese was only increased in the left olfactory bulb. The dissolution rate of the manganese oxide NPs, measured by ICP-OES, was less than 1.5% per day. The authors concluded that the olfactory neuronal pathway efficiently translocates inhaled manganese oxide NPs to the central nervous system. The authors suggested that despite differences between human and rodent olfactory systems, the pathway is relevant also in humans (Elder, Gelein *et al* 2006).

5.2.10 Multi-walled carbon nanotubes

Wistar rats were exposed nose-only to 11 or 241 mg/m^3 MWCNT (Baytubes, diameter 10-16 nm), containing 0.53% cobalt, for 6 h. Cobalt in tissues (brain, liver, lung, kidney, testis) was analyzed by AAS. In animals given the low dose, cobalt was elevated in lungs after 1 wk but not after 13 wk. Following the high dose (lung overload) cobalt in lung was elevated also after 13 wk. No increases in cobalt were seen in the other tissues examined, with one exception, namely, a slight and transient increase in liver 1 wk after the high dose. The results suggest that the uptake of MWCNT via lungs was minor, if any (Ellinger-Ziegelbauer and Pauluhn 2009).

Male mice were exposed whole-body to MWCNT aerosol (5 mg/m^3 5 h/d, 4 times weekly for 3 wk), resulting in a lung burden of 28.1 µg/lung. Tissues were analyzed for MWCNT by enhanced dark field microscopy, morphometric methods and field emission scanning electron microscopy (FESEM). The tracheobronchial lymph nodes contained 1.1% and 7.3% of the lung burden at days 1 and 336 post-exposure, respectively. The corresponding percentages for other tissues were: liver 0.003% and 0.003%, kidney 0.001% and 0.005%, heart 0.0002% and 0.0007%, brain 0.001% and 0.002%, chest wall 0.004% and 0.0009%, and diaphragm 0.0003% and 0.0004%. Agglomerates accounted for approximately half the lung burden, however, only single

MWCNT were observed in the examined extrapulmonary tissues. At 1 d post exposure, the average length of singlet MWCNT in liver and kidney (8.2 µm), was comparable to that in the lungs (7.5 µm) (Mercer, Scabilloni *et al* 2013).

5.2.11 Quantum dots

Two male Wistar rats were head-nose exposed to QDs ($CdS/Cd(OH)_2$, core 73 nm, MMAD 1.7 µm, 4.1 mg/m^3 corresponding to 0.52 mg Cd/m^3, 6 h/d for 5 d). Cadmium burden in organs was determined by ICP-OES. The approximate concentrations directly after exposure and 3 wk later were: lungs 10 µg and 7 µg, liver 1.6 µg and 2.1 µg, kidneys 0.5 µg and 1.5 µg, respectively. There was no evidence of translocation to the central nervous system (Ma-Hock, Brill *et al* 2012).

Rats were exposed nose-only to non-coated or coated QDs ($CdS/Cd(OH)_2$, MMAD 1.5-4 µm) 6 h/d for 5 d at a concentration of 2 mg/m^3. Cadmium levels in select organs (brain, kidneys, liver, lungs, mediastinal lymph nodes, spleen) and excreta were determined after the end of exposure and 3 wk later by ICP-MS. Since cadmium ions were present as an impurity, rats were similarly exposed to cadmium chloride. All cadmium exposures resulted in similar profound increases (approximately ten-fold above the detection limit) in cadmium levels in lung at both time points and slight increases in liver at the end of exposure but not 3 wk later. There was no evidence of translocation of particles from the respiratory tract, however, considering the detection limit in tissues, minor uptake would remain unnoticed (Ma-Hock, Farias *et al* 2014).

5.2.12 Silica

Studies describing inhalation exposure to nanosized crystalline silica were not found.

A study by (van Ravenzwaay, Landsiedel *et al* 2009) describes comparative exposures of rats to nano and pigmentary titanium dioxide, and to bigger size quartz dust. The study is described below under the section on titanium dioxide.

5.2.13 Silver

Rats were exposed whole-body for 6 h to 133 µg/m^3 silver NPs (15 nm) and were sacrificed on days 0, 1, 4, and 7. ICP-MS analyzes showed that 1.7 µg silver was found in the lungs at the end of exposure and then decreased rapidly reaching 4% of the initial burden at day 7. Significant amounts of silver were detected in liver (0.16 µg) and blood on day 0 and thereafter decreased rapidly. Low concentrations were detected in kidney, spleen, brain, and heart. Nasal cavities, especially the posterior portion, and lung-associated lymph nodes showed relatively high concentrations of silver. For comparison, rats were instilled it with either 7 µg silver nitrate (4.4 µg Ag, aqueous solution) or 50 µg agglomerated silver NPs (aqueous suspension). A portion of the agglomerates remained undissolved in the alveolar macrophages and in the septum for at least 7 d. In contrast, silver nitrate was rapidly cleared from the lung (Takenaka, Karg *et al* 2001).

Male and female rats were exposed whole-body to 19-nm silver NPs for 6 h/d, 5 d/wk, for a total of 4 wk. The exposure levels were: 0 (control), 0.8 (low), 5.8 (mid) and 61 µg/m^3 (high dose). Silver in tissues was measured by AAS. Following the highest exposure, silver was markedly elevated in lung (1200-1500 µg/g) and significantly

elevated in liver (5-7 µg/g), brain (2-3 µg/g), blood and olfactory bub (7-9 µg/g). Marginal, non-significant increases in silver were seen after the low and mid exposures (Ji, Jung *et al* 2007).

S-D rats were exposed whole-body to silver NPs (18-19 nm) for 13 wk (6 h/d, 5 d/wk) to clean air, 49 (low dose) 133 (mid dose) or 515 mg/m^3 (high dose). In both sexes, silver in tissues, measured by AAS, increased in a dose-dependent manner in lung (14645 ng/g after 4 wk) liver (133 and 71 ng/g in male and female rats, respectively), kidney (9 and 38 ng/g), olfactory bulb (31 and 33 ng/g), brain (19 and 20 ng/g) and blood (4 and 7 ng/g) (Sung, Ji *et al* 2009).

Mice were exposed nose-only to 2.9 mg/m^3 of 20-nm silver NPs for 6 h. Silver in tissues were determined by AAS before, at end of exposure and 24 h later. Elevated silver levels were demonstrated for lung and heart but not brain, liver, spleen and testis. The results are difficult to evaluate in quantitative terms, due to the high background levels in unexposed animals (Kwon, Minai-Tehrani *et al* 2012).

Male and female rats were exposed whole-body to silver NPs (14-15 nm) at 49 µg/m^3 (low dose), 117 µg/m^3 (mid dose) or 381 µg/m^3 (high dose) for 6 h/d for 12 wk. Silver in tissues was measured by AAS at the cessation of exposure and 4 wk and 12 wk later. Dose-dependent increases in silver concentration were seen in all examined tissues (blood, brain, eye, kidney, liver, lung, spleen, testis/ovary), with highest levels in liver and kidney and lowest in eye and brain. The concentrations in tissues after the mid and high exposures were roughly 0.5-2% of that in lung. Half-times of silver in lung tissue were calculated to be 29 and 39 d in males and female rats, respectively, after the low dose, 85 and 113 d after the mid dose and 42 and 40 d after the high dose (Song, Sung *et al* 2013).

Rats were exposed nose-only to clean air, 15-nm (179 µg/m^3) or 410-nm (167 µg/m^3) silver particles 6 h/d, for 4 d. The tissue distribution was measured by ICP-MS at 24 h and 7 d after exposure and compared with the internal alveolar dose. Twenty-four hours after exposure to the 15-nm NPs, lung and liver contained 3.4 and 0.06 µg/g, respectively. The corresponding values for 410-nm particles were 6.0 µg/g and below limit of detection. The internal alveolar silver dose 15 nm nanoparticles was 3.5 times higher after exposure to 15-nm compared to 410-nm particles. TEM analysis revealed that 15-nm NPs present in vesicles and nuclei of lung cells had decreased to less than 5 nm 24 h after exposure due to substantial dissolution of the silver NPs (Braakhuis, Gosens *et al* 2014).

5.2.14 Titanium dioxide

Oberdörster *et al* studied lung disposition and effects of anatase titanium dioxide particles of two sizes, 20 nm and 250 nm. Both formed agglomerates in air with mass median aerodynamic diameters of 710 and 780 nm, respectively. Rat were exposed whole-body for 12 wk (6h/d, 5 d/wk) at 23.5 and 22.3 mg/m^3, respectively. Similar mass depositions of the two particle types in the lower respiratory tract were seen. However, the retention differed significantly with prolonged retention in the lung and increased translocation to the pulmonary interstitium, and persistence there, of the smaller particle type (Oberdörster, Ferin *et al* 1994).

Rats inhaled 22-nm (primary size 4 nm) titanium dioxide NPs for 1 h at a concentration of 0.11 mg/m^3. The intrapulmonary distribution of particles was analyzed 1 and 24 h after exposure using energy-filtering TEM for elemental microanalysis of individual particles. The inhaled NPs were found on the luminal side of airways and alveoli, in all major lung tissue compartments and cells, and within capillaries (Geiser, Rothen-Rutishauser *et al* 2005).

Rats were exposed for 1 h to 22-nm titanium dioxide NPs (exposure concentration not stated) and the lungs were examined light microscopy and energy filtering TEM at 1 h and at 24 h after exposure. The size of four lung compartments were estimated by light microscopy and the number of NPs were counted using energy filtering TEM. A relative deposition index (RDI) was calculated for each compartment based on the compartment volumes and NP counts. RDI=1 indicates equal (random) distribution whereas RDI > 1 indicates preference for the compartment. The RDIs to the four compartments at 1 h and 24 h were: airspace 0.92 and 0.96, epithelium/endothelium 1.14 and 0.73, connective tissue 2.65 and 1.15, and capillary lumen 1.27 and 1.65. Thus, at 1 h post-exposure the connective tissue was the preferential target of the NPs, whereas at 24 h they were preferentially located in the capillary lumen. The authors suggested that a small fraction of NPs are rapidly transported from the airway lumen to the connective tissue and subsequently released into the systemic circulation (Mühlfeld, Geiser *et al* 2007).

Male Wistar rats were exposed for 5 d (6h/d) head/nose-only to 100 mg/m^3 nano titanium dioxide (20-30 nm, MMAD 1.0 µm), 250 mg/m^3 pigmentary titanium dioxide (200 nm, MMAD 1.1 µm), or to 100 mg/m^3 quartz dust (DQ 12, 315 nm, MMAD 1.2 µm). Deposition in the lung and other tissues was evaluated upon termination of exposure, and 2 wk later. Most of the inhaled nanosized titanium dioxide was deposited in the lung, as measured by ICP-AES. Translocation to the mediastinal lymph nodes was noted and was much higher than for quartz dust (3%) but smaller than for pigmentary titanium dioxide. Electron microscopy showed that the particles from both the pigment and the nano-scale material were mainly located extracellularly in the lumen of the alveoli and bronchi. Particles were also detected in the cytoplasm of alveolar macrophages. The nano materials in the lung were mostly agglomerates of about the same size as those in air and there were no signs of deagglomeration. Rats were also given a single *iv* dose of a titanium dioxide suspended in serum (5mg/kg bw), and tissue contents of were determined 1, 14 and 28 d later. Titanium dioxide was trapped mainly in the liver (134 µg/g at day 1) and spleen (79 µg/g) and less so in lung (9 µg/g) and kidney (0.7 µg/g), and disappeared gradually over the observation period (van Ravenzwaay, Landsiedel *et al* 2009).

5.2.15 Uranium

Rats were exposed nose-only to an aerosol containing 1 180 µg/m^3 of 38-nm uranium NPs (MMAD 179 nm) for 1 h and uranium in respiratory tract, blood, brain, bone and kidney was measured by ICP-MS. Uranium concentrations (measured 10 min, 4 h and 24 h post-exposure) were significantly elevated over background in all tissues except brain. Twenty-seven percent of the inhaled uranium NPs was deposited in the respiratory tract while 20% were rapidly cleared from lung with a half time of 2.4 h. Most NPs had a much slower clearance with a half time of 141.5 d (Petitot, Lestaevel *et al* 2013).

5.2.16 Zinc oxide

Mice (C57Bl/6) were exposed whole-body to crystalline zinc oxide NPs (3.5 mg/m^3, 4 h/d) for 2 wk (NP size 15 nm) or 13 wk (NP size 26 nm) and necropsied immediately or 3 wk post-exposure. Zinc in lung, blood, liver, kidney, spleen, heart, brain and BAL fluid was measured by ICP-MS. Elevated levels of zinc ion were measured in BAL fluid (both groups), lung tissue (2-wk group only) and heart (13-wk study only) immediately after exposure but not at 3 wk post-exposure. Dissolution studies showed that the zinc oxide NPs readily dissolved in artificial lysosomal fluid (pH 4.5, 100% dissolved), but formed aggregates and precipitated in artificial interstitial fluid (pH 7.4, approximately 0.1% dissolved) (Adamcakova-Dodd, Stebounova *et al* 2014).

5.3 Conclusions – inhalation uptake

Several animal studies report small but significant increases in systemic levels of a main NP con-stituent after inhalation exposure, suggesting that the NPs are absorbed to a low but measurable degree via the respiratory route. Thus, as summarized in a recent review (Kermanizadeh, Balharry *et al* 2015), elevated levels of *eg* carbon, cerium, gold, iridium, iron, manganese, MWCNT, QDs, silver, titanium, uranium and zinc have been detected in one or several secondary organs (blood, bone marrow, brain, heart, kidneys, liver and/or spleen) following inhalation exposure to the corresponding NP. Similarly, cerium, diamond, fullerenes, gadolinium, gold, latex, lead, manganese, MWCNT, polystyrene, QDs, zinc, have been detected after it instillation, and copper, gold, manganese, polystyrene and titanium after intranasal instillation (Kermanizadeh, Balharry *et al* 2015).

Unfortunately, most studies were not designed and do not present data, in a way that allows a quantitative estimate of the systemically absorbed fraction. Some studies, mainly performed with rats, present NP amounts in organs relative to the inhaled or lung deposited dose. These studies are summarized in Table 4.

The per cent estimates given in Table 4 should be interpreted with caution, as they vary considerably between studies and it is difficult to judge if this variation is due to methodological issues (such as experimental design, exposure system, sampling time and species and strain differences), NP properties (such as size, shape, degree of agglomeration and zeta potential) or simply reflects method error. Most studies have been carried out with metal or metal oxide NPs and a major concern is that of dissolution and subsequent uptake of ions, *ie* not NP uptake per se. However, most studies have addressed and seemingly controlled for this aspect. Another concern relates to repeat whole-body exposure in exposure chambers. In these experiments there is a high risk of contamination or secondary exposure after licking the fur.

It is difficult to accurately assess the total absorption via inhalation from the scattered data in Table 4 since only some (major) organs are accounted for. Nevertheless, the data suggest that the total systemic uptake (*ie* excluding mucosal clearance to the GI-tract of larger NPs is generally below 1% for the bigger (80 nm) NPs and perhaps up to a few percent for the smaller ones.

Table 4. Summary of quantitative rat data on inhalation absorption of nanoparticles.

Nano-particle	Size (nm)	Exposure duration and concentration	Recovery 24 h post-exposure (% of inhaled dose)			Reference
Carbon, ^{192}Ir - labeled	25	1 h [1] ns [3]	Lung 2 70% Blood 0.1% Brain 0.03% Heart 0.053%	Kidney Liver Spleen	0.06% 0.06% 0.05%	Kreyling, Semmler-Behnke *et al* 2009
Gold	5-8	7 d 88 µg/m^3	0-7 d post-exposure: Blood 0.03-0.06% of lung concentration			Takenaka, Karg *et al* 2006
Gold	7 20	15 d 86 µg/m^3	2 d post-exposure: [6] Secondary organs 1.4% Secondary organs 0.2%			Balasubramanian, Poh *et al* 2013
Iridium-192	15-20	1-1.5 h [1] Deposited dose 11.2 µg	7 d post-exposure: [6] Liver 0.6% Kidneys 0.6% Spleen 0.4% Brain 0.3%			Semmler, Seitz *et al* 2004
Iridium-192	15 80	1 h [1] ns	7 d post-exposure: [6] Liver 0.3-0.5% Liver 0.6-0.8%			Kreyling, Semmler *et al* 2002
Iridium-192	20	1 h [1] ns	Lung [2] 64% Blood 1.7% Brain 0.3% Heart 0.3%	Kidney Liver Spleen	0.2% 0.2% 0.5	Kreyling, Semmler-Behnke *et al* 2009
Iridium-192 [4]	30	1 h [1] ns	Lungs 54% Trachea 0,05% Heart 0,01% Skin 4,9% Liver 0,01% Kidneys 0,01%	GI tract Head Brain Remainder Urine Feces	4,1% 0,1% 0,01% 0,2% 0,02% 41%	Geiser, Stoeger *et al* 2014
Iridium-192	80	1 h [1] ns	Lung 2 86% Blood 0.1% Brain 0.03% Heart 0.053%	Kidney Liver Spleen	0.06% 0.06% 0.05%	Kreyling, Semmler-Behnke *et al* 2009
MWCNT 4	1 500 [5]	12 d 5 000 µg/m^3	1 d post-exposure: Tracheobronchial lymphnodes 1.1% Liver 0.003% Kidney 0.001%	336 d post-exposure 7.3% 0.003% 0.005%		Mercer, Scabilloni *et al* 2013

Nano-particle	Size (nm)	Exposure duration and concentration	Recovery 24 h post-exposure (% of inhaled dose)		Reference
			Heart 0.0002% Brain 0.001% Chest wall 0.004% Diaphragm 0.0003%	0.0007% 0.002% 0.0009% 0.0004%	
QD CdS(CdOH)$_2$	73	5 d 520 µg/m^3	0 d post-exposure: Lungs 10 µg Liver 1.6 µg Kidneys 0.5 µg	21 d post-exposure 7 µg 2.1 µg 1.5 µg	Ma-Hock, Brill *et al* 2012
Uranium	3.2	1 h 1 180 µg/m^3	1 d post-exposure: Extra thoracic region 55 ng Bronchial region 27 ng Bronchiolar and alveolar region 3257 ng Blood 9 ng Bones 134 ng Kidneys 200 ng Brain olfactory 0.3 ng Brain rest 0.4 ng		Petitot, Lestaevel *et al* 2013

1 Exposure via intubation.
2 Including BAL fraction.
3 Exposure concentration not stated.
4 Experiment performed with mice.
5 Mass median aerodynamic diameter (MMAD) assuming lognormal distribution.
6 Percent of lung deposited dose.

6 Other exposure routes

6.1 Intratracheal instillation

6.1.1 Albumin

Hamsters were given 100 µg of ^{99m}Tc -labeled albumin nanocolloid NPs (< or = 80 nm) by it instillation. Thin-layer chromatography of blood samples showed only one peak of radioactivity corresponding to unaltered labeled albumin nanocolloid. The radioactivity in blood was 2.9% of the dose at 5 min after instillation, 1.3% at 15, 1.5% at 30 min, and 0.2% at 60 min. The corresponding recoveries in liver were 0.1%, 0.2%, 1.2%, and 0.06%. Lower values were observed in the heart (0.08-0.2%), spleen (0.01-0.002%), kidneys (0.3-0.07%), and brain (0.006-0.002%). Similar tissue recoveries were attained after instillation of 10 µg and 1 µg of albumin NPs (measured at 30 min), suggesting no dose-dependence in biodistribution. The authors concluded that a significant fraction of these NPs rapidly diffuses from the lungs into the systemic circulation (Nemmar, Vanbilloen *et al* 2001).

6.1.2 Cerium oxide

Cerium-144 oxide NPs (6.6 nm, 0.2 mg) were given by it instillation to Wistar rats and 144Ce radioactivity was measured in various organs at 6 h, 7d, and 28 d after dosing. The elimination half-time from lung was 103 d and 64% of the instilled amount remained in the lung 28 after dosing. Only 12-30% was cleared via the GI tract, suggesting that phagocytosis by alveolar macrophages with subsequent removal towards the larynx was not the predominant route for the elimination from the lung. Whole-body biodistribution studies showed that the lung deposited nanoceria can penetrate through the alveolar wall into the systemic circulation and accumulate in other organs. Thus, the cerium content increased over time in liver, spleen, kidney, blood, bone and testicle, remained approximately constant in heart, and decreased in lung, stomach, intestine, brain and muscle. The systemic body burden (sum of brain, liver, spleen kidney, brain and testicle, estimated from figure 2) at 28 d post-dosing is estimated to approximately 0.1% of the administered dose (He, Zhang *et al* 2010).

6.1.3 Fullerenes

Male Wistar rats were it instilled with 100, 200 or 1000 µg of fullerenes in a suspension prepared with Tween 80 (aerosol particle diameter 18-29 nm). Fullerenes in lung, liver, and brain were determined from 1 h and up to 6 months by HPLC after organ extraction and concentration from the organs. The concentrations in liver and brain were below the detection limit of 8.9 ng/g tissue. The half-time in lung was 15-28 d, with particle overload in lungs after the highest dose. The pulmonary clearance was evaluated with a two-compartment model to account for fast and slow elimination. Most instilled fullerenes were eliminated by the fast clearance pathway, a finding consistent with the TEM observations that many particles were present in alveolar macrophages. Pulmonary fullerene burden decreased with time and depended on the fullerene concentration administered. Rats were also exposed to 120 µg/m^3 f fullerene aerosol by

inhalation. The deposition mass fraction of inhaled fullerene was 0.14 (Shinohara, Nakazato *et al* 2010).

6.1.4 Gold

Gold-198 NPs (1.4 and 18 nm), were created by neutron activation and given by it instillation to female Wistar-Kyoto rats. Tissues were collected 24 h later and analyzed for radioactivity. The 1.4-nm NPs were mainly retained in the lungs (91.5% of the instilled dose) but significant amounts were also found in carcass 3.3%), skin (1.5%), kidneys (1.2%), urine (1.1%), liver (0.7%) and blood (0.6%). NPs were not detected in spleen, brain, heart and uterus (all <0.1%). In contrast, the 18-nm NPs were almost entirely recovered in the lungs (99.8%) with a minor amount in carcass (0.1%) and amounts below 0.1% in the other tissues. After *iv* injection, NPs were not captured by the lungs but by the liver (48% for 1.4 nm and 94% for 18-nm NPs) and spleen (1.3% and 2.2%). Disregarding the lungs, the biodistribution to other tissues was similar for both exposure routes (Semmler-Behnke, Kreyling *et al* 2008).

Gold NPs (2, 40, 100 nm) were instilled it in adult female mice. One group of mice were given a single dose and were killed after 1 h, another group were does 5 times over 3 wk and the animals were killed 24 h after the last dose. NPs in tissue were traced by autometallography at both ultrastructural and light microscopic levels. Gold content was quantified by ICP-MS and neutron activation analysis (NAA). The gold NPs were found in lung macrophages already 1 h after a single instillation and in mice dosed repeatedly the load was substantial, still AMG, ICP-MS and NAA analyzes of the liver showed an almost total lack of translocation of NPs. Thus, repeat dosing with 2-nm NPs resulted in 0.14% (by ICP-MS) to 0.19% (by NAA) recovery in the liver. With 40-nm and 100-nm NPs, no gold was detected in liver (detection limit 2 ng, corresponding to 0.01% of dose) except for one mouse (out of 5) given 40-nm and one mouse (out of 5) given 100-nm NPs, in which 0.3% and 0.04% of the dose, respectively, were found in the liver. The authors concluded that inert gold NPs are phagocytized by lung macrophages, that only a small fraction is translocated into the systemic circulation, and that the translocation is greatest with the smallest (2 nm) gold NPs (Sadauskas, Jacobsen *et al* 2009).

Gold colloid particles (20 nm and 200 nm, 50 µg) were it instilled in male BAlb/c mice. At 15 min after instillation, dispersed and agglomerated 20-nm gold colloid particles were observed by TEM on the surface of endothelial cells, on the alveolar surface, in endocytic vesicles of alveolar epithelial cells, and in the basement membrane of the lung. For both particle sizes, most of the body burden (20-nm NPs: 75%, 200-nm particles: 90%) was located in lung, yet small but significant amounts of gold were detected by ICP-MS in liver (0.01%, 0.03%), kidney (0.002%, 0.0002%), spleen (0.003%, 0.0008%), and heart (0.0003%, not detected). Gold was not detected in brain (detection limit 0.01 ng/ml). Based on this and a parallel study with fluorescent polystyrene particles (described below), the authors concluded that small amounts of the 20-nm NPs are transported across the alveolar wall into the blood circulation via endocytic pathways, whereas alveolar macrophages translocate both 20-nm and 200-nm particles from the lungs to the extrapulmonary organs (Furuyama, Kanno *et al* 2009).

Plain (prepared with bis(p-sulfonatophenyl)phenylphosphine to enhance colloidal stability) and PEG-modified (750 Da and 10 kDa) radiolabeled gold NP (5 nm core diameter) suspensions were instilled it to female Wistar-Kyoto rats. The doses were approximately 100 µg/kg bw. Gold content in tissues, organs and excretion were quantified by gamma spectroscopy after 1 and 24 h. The majority of all three types of applied NPs stayed in the lungs and approximately one third was cleared by the mucociliary pathway with no clear difference between the three. Moreover, the systemic translocation did not differ considerably after PEGylation; however, a prolonged retention time in the circulation was detected for the small fraction of translocated gold-PEG10k NPs. This finding was in agreement with an *iv* study performed in parallel, showing that the uptake in liver of the PEG10k NPs after 1 h was less than 5% of the injected dose. In contrast the uptake of plain and PEG750 NPs in liver was approximately 90%. The distribution to other organs also differed, depending on PEGylation. Thus, at 24 h post-instillation the recovery in carcass was 10% for PEG750, 4% for plain and 0.5% of the dose for PEG10k NPs. The recovery of PEG750 NPs in brain was 0.004% of the dose, whereas the two other types were not detected (Lipka, Semmler-Behnke *et al* 2010).

Male BALB/c mice received a single dose of 0.8 mg/kg bw of gold NPs (40 nm) by oropharyngeal aspiration 24 h with (pretreated) or without (healthy) previous instillation treatment with lipopolysaccharide to induce inflammation. Metal content was analyzed ICP-MS. High gold concentrations were seen in lungs from the healthy animals, however these concentrations were approximately 10-fold lower in the pretreated animals. Furthermore, healthy animals had significantly higher gold levels ted in heart and thymus of, whereas the pretreated had higher levels in spleen (Hussain, Vanoirbeek *et al* 2013).

Kreyling *et al* studied the pulmonary biokinetics in rats of it instilled monodisperse radiolabeled (198Au), negatively charged gold NP of five sizes; 1.4, 2.8, 5, 18, 80, and 200 nm, and of 2.8-nm gold NP with positive surface charge. The distribution to tissues was measured at 1, 3, and 24 h post-dosing by gamma spectrometry. The study showed a clear and consistent size-dependency in biokinetics, in that as the NPs get smaller, they are more likely to cross the air-blood barrier depending strongly on the inverse diameter of the gold core, *ie* the specific surface area. Thus, the smallest (1.4 nm) NPs had the highest and the second biggest (80 nm) NPs had the lowest translocation. However, the 200-nm NPs had a higher translocation than the 80-nm NPs and did thus not follow the surface area rule. Translocation of 5, 18, and 80 nm gold NPs is virtually complete after 1 h, while 1.4 nm gold NPs continue to translocate until 3 h. The translocation of negatively charged 2.8-nm gold NPs was significantly higher that of the positively charged NPs. The study shows that translocation across the lung and to secondary organs are two distinct processes, both depending specifically on particle size/surface area and surface charge (Kreyling, Hirn *et al* 2014).

6.1.5 Polystyrene

The extrapulmonary distribution of iodine-125 labeled polystyrene NPs (56 and 202 nm, 0.6 mg per animal) was measured up to 120 h in it dosed rats. Rats receiving a single it dose of free ^{125}I or a single *iv* injection of ^{125}I -labeled NPs served as controls. In healthy

rats, the pulmonary deposition and biodistribution of radioactivity were similar for both particle sizes. However, following pretreatment with lipopolysaccharides (inducing pulmonary inflammation) translocation to blood of the smaller sized particles was significantly higher (2.0-4.7%) compared to the larger ones (2.2%). The translocation to liver was also higher in pretreated rats given the larger particles (11% of the dose, compared to 3.5% for the healthy rats and the smaller NPs). The authors concluded that only a small fraction of it instilled NPs passes into the systemic circulation in healthy rats, but that pulmonary inflammation enhances this extrapulmonary translocation (Chen, Tan *et al* 2006).

Fluorescein-labeled polystyrene particles (50 µg, 20 nm and 200 nm) were given to male BAlb/c mice by it. Free particles were detected infrequently by TEM in blood vessels, on the endocardial surface, and in the kidney and liver only in the mice that received the smaller size, whereas phagocytes containing 20- or 200-nm particles were found in the extrapulmonary tissues. Experiments with particle-laden alveolar macrophages administered it showed that these translocated from alveoli to extrapulmonary organs via the blood circulation (Furuyama, Kanno *et al* 2009). Due to the qualitative nature of this study, the extent of pulmonary translocation cannot be assessed.

Copper-64 labeled 100-nm polystyrene NPs were instilled it into C57BL/6 mice and deposition and biodistribution was followed for 48 h by PET imaging. Quantitative analyzes showed that 79% (0 h post-dosing) to 76% (48 h) of the instilled dose remained in the lungs. Minimal amounts (below 0.1%) were detected in bladder and liver. Significant amounts in trachea (10-1%) mouth (5-1%), and GI tract (15-10%) demonstrated the importance of mucociliary clearance from the upper respiratory tract to the GI tract (Palko, Fung *et al* 2010).

The biodistribution of 100-nm 64Cu-labeled polystyrene NPs was measured by PET imaging for 48 h following it instillation of 5x1012 particles in healthy and asthmatic mice (ovalbumin induced). The asthmatic mice had a smaller initial accumulation in lung than healthy animals (74% *vs* 90% of instilled dose at 0 h) and the NPs cleared faster (56% *vs* 80% remaining after 48 h). In addition, somewhat higher amounts were recovered in the asthmatic compared to healthy mice in trachea (6.1% *vs* 5.2% at 0 h), intestines (7.1% *vs* 6.6% after 4 h), bladder (1.5% *vs* 0.3% after 24 h) and liver (0.8% *vs* 0.2% after 48 h). This decrease in lung retention is significantly different when compared to the normal mouse (~11% of the deposited dose). The study indicates that these NPs undergo enhanced transport out of the lungs in asthmatic animals (Enright, Bratt *et al* 2013).

6.1.6 Quantum dots

Male S-D rats were exposed by it instillation to 1.25, 5.0, or 12.5 µg of quantum dots composed of a cadmium-selenide (CdSe) core (~5nm) with a zinc sulfide (ZnS) shell functionalized with carboxyl (QD-COOH) or amine (QD-NH2) terminal groups. The left lung, lung-associated lymph nodes (LALN), heart, kidneys, spleen, liver, brain, and blood were collected for analysis of cadmium content by neutron activation. Both QD types appeared to lose their fluorescent properties and destabilize after 1 wk in the lung. Cadmium persisted in the lung up to 28 d for both forms, however, the clearance rate

was slightly greater for QD-COOH. Cadmium appeared in the LALN and kidneys beginning at 1-2 wk post-exposure. The recoveries (as % of instilled dose) of QD-COOH and QD-NH2 after 28 d were 25% and 40% in LALN and 6% and 10% in kidney. Cadmium was not detected in the other examined tissues at any time point (Roberts, Antonini *et al* 2013).

6.1.7 Silver

Male C57Bl/6 mice were exposed once to citrate coated 20-nm or 110-nm silver NPs by oropharyngeal aspiration at doses up to 1 mg/kg bw. Tissue silver levels were assessed 21 d later by ICP-OES. Silver was only detected in lungs (around 7 µg/mg protein for both NP sizes) and not in heart, liver, spleen, kidney or brain (Wang, Ji *et al* 2014).

6.1.8 Titanium dioxide

The lung distribution of titanium dioxide NPs (20 nm) in mice was examined using synchrotron radiation X-ray fluorescence (XRF) imaging following it administration of 1 mg/kg bw. The NPs were mainly retained in lungs, cleared slowly and were still present after 3 months (229 µg/g lung tissue after 1 d, 79 µg/g after 3 months). The XRF imaging showed an uneven distribution of titanium within the lung tissue, that the instillation technique (with or without air) influenced the lung clearance, and that titanium dioxide NPs I interfered with the natural distribution of metals (K, Ca, Fe, Cu, Zn) in lungs (Zhang, Li *et al* 2013).

Titanium dioxide NPs (Aerosil P25, 20 nm) were it administered to male F344 rats at doses of 0, 0.375, 0.75, 1.5, 3.0, and 6.0 mg/kg bw. Titanium levels in various lung and other tissues organs were determined by ICP-MS. The lungs contained 62-83% of the dose 1 d after administration. After 26 wk, the lungs contained 6.6-8.9%, 13% and 21% of the administered dose in rats that had received the three lowest doses, 3 mg/kg and 6 mg/kg, respectively. Translocation of titanium dioxide from the lungs to the thoracic lymph nodes increased in a time- and dose-dependent manner, accounting for 0.10-3.4% of the administered dose after 26 wk. A small amount of titanium dioxide was found in liver after 3 d (0.002-0.01% of the highest dose administered, 6.0 mg/kg). Translocation to the other extrapulmonary organs was not detected (Shinohara, Oshima *et al* 2014).

Balb/c mice were oropharyngeally aspirated with 20 µg pristine NPs of titanium dioxide (15 nm), silver (25-85 nm), silicon dioxide (19 nm) or aged paint particles (also containing titanium dioxide, silver and silicon dioxide but larger particle sizes) once a week for 5 wk and sacrificed either 2 or 28 d after the final dosing. Biodistribution measurements showed distribution of silver and silicon outside of the lung after dosing with aged as well as pristine NPs. Tissue levels were generally lower after dosing with aged compared to pristine NP (Smulders, Luyts *et al* 2014).

Table 5. Summary of quantitative animal data on systemic absorption of nanoparticles given by intratracheal instillation (values rounded off).

Nanoparticle	Core diameter (nm)	Zeta potential [1] (mV)	Dose [1] (µg/kg bw)	Species	Systemically absorbed [2,3] (% of instilled)	Reference
Albumin	<80 - 80	ns	1 µg 10 µg 100 µg	Hamster	3%	(Nemmar, Vanbilloen *et al* 2001)
Cerium oxide	6.6	+30	200 µg	Rat	0.1%	(He, Zhang *et al* 2010)
Fullerenes	18-29	-29	100 µg 200 µg 1000 µg	Rat	nd	(Shinohara, Nakazato *et al* 2010)
Gold	1.4, 18	ns	ns	Rat	9%, 0.1%	(Semmler-Behnke, Kreyling *et al* 2008)
Gold	2 40 100	-	ns	Mouse	0.1-0.2% (liver) nd (liver) nd (liver)	(Sadauskas, Jacobsen *et al* 2009)
Gold	20 200	-	ns	Mouse	<0.1%	(Furuyama, Kanno *et al* 2009)
Gold, Phos-coated *Id*, PEG750-coated *Id*, PEG10k-coated	5	-28 -19 -10	100	Rat	4% 10% 0.5%	(Lipka, Semmler-Behnke *et al* 2010)
Gold [3]	1.4 2.8 2.8 5 18 80 200	-21 - + -21 -23 -22 -41	2.6 µg 0.8 µg 20 µg 35 µg 2.5 µg 18 µg 14 µg	Rat	6.0% 3.1% 1.3% 0.22% 0.12% 0.06% 0.21%	(Kreyling, Hirn *et al* 2014)
Titanium dioxide	20	-44	6000	Rat	0.1-3.4% (thoracic lymph nodes)	(Shinohara, Oshima *et al* 2014)
Polystyrene	56 202	ns	600 µg	Rat	Approx 6%	(Chen, Tan *et al* 2006)

Nanoparticle	Core diameter (nm)	Zeta potential [1] (mV)	Dose [1] (µg/kg bw)	Species	Systemically absorbed [2,3] (% of instilled)	Reference
Polystyrene	100	ns	ns	Mouse	<0.1% (bladder, liver)	(Palko, Fung *et al* 2010)
Polystyrene	100	-22	ns	Mouse	0.5% (bladder, liver)	(Enright, Bratt *et al* 2013)
QDs	5	- +	1.25, 5, 12.5	Rat	6% (kidneys) 10% (kidneys)	(Roberts, Antonini *et al* 2013)
Silver, citrate coated Id, PVP-coated	20, 210 20, 210	-47	100, 500, 1000	Mouse	nd	(Wang, Ji *et al* 2014)
Zinc oxide, uncoated Id, silica coated	29 28	+23 -16	1000	Rat	58% 47%	(Konduru, Murdaugh *et al* 2014)

1 ns = not stated.
2 nd = not detected.
3 Estimated from sum of major systemic organs.

6.1.9 Zinc oxide

The biokinetics of uncoated and silicone oxide coated neutron activated 65zinc oxide NPs was followed in rats after oral administration (see chapter Oral absorption) and it instillation at doses of 1 mg/kg bw. Tissue samples were analyzed for 65Zn radioactivity at 2, 7 and 28 d after dosing. The NPs were rapidly cleared from lungs with initial half-times of 0.2-0.3 h, and later half-times of 1.2-1.7 d, with the silica-coated being cleared more rapidly than the uncoated NPs. 16-18% of the instilled dose remained after 2 d, 1.1-1.9% after 7 d and 0.14-0.28% after 28 d. A corresponding rapid distribution to, but a much slower elimination from, non-lung tissues was seen for both NP types. The NPs were preferentially distributed to bone (12% of the dose at day 7), skeletal muscle (8-20%), liver (5-6%) and bone marrow (3-4%). The elimination half-times in secondary tissues (calculated by us from the levels at days 7 and 28) were 1-2 wk in most examined organs, with longer half-times in brain, skin and skeletal muscle. After 28 d 37% of the uncoated and 24% of the silica-coated still remained in the body. In general, uncoated NPs reached 20-40% higher concentrations compared to the silica-coated NPs. The overall half-times (based on total 65Zn in secondary tissues) were 3 wk for uncoated and 4 wk for silica-coated NPs. The major effects of silica-coating were enhanced transport to thoracic lymph nodes and decreased transport to skeletal muscle (Konduru, Murdaugh *et al* 2014).

Adult female C57BL/6 mice were exposed via it instillation to 18 or 162 mg of titanium dioxide NPs (rutile, 20.6 nm). Using a nanoscale hyperspectral microscope,

translocation of NPs to heart and liver was confirmed at both doses, and to blood at the high dose, at 24 h post-exposure (Husain, Wu *et al* 2015).

6.1.10 Conclusions – Intratracheal instillation

Quantitative studies on systemic absorption from it instillates are summarized in Table 5. The percent systemic absorption is highly variable, ranging from over 50% uptake to below fractions of a percent or undetected, and there is no obvious relation between percent absorbed and type of NP or surface charge. The high variability may be a result of *eg* differences in instillation technique, instilled dose and volume, time of tissue sampling, tissues analyzed and detection limits. The uptake clearly increases as NP size decreases, as most clearly seen in the paper by Kreyling *et al* (Kreyling, Hirn *et al* 2014). It should be noted that instillation is rather unphysiological and cannot readily be translated to inhalation uptake.

6.2 Intranasal administration

6.2.1 Polyanhydride nanoparticles

The in vivo distribution, depot effect, and localized persistence of various polyanhydride NPs were studied as a function of NP chemistry and administration route. The NPs were administered subcutaneously, intramuscularly or intranasally to hairless SKH-1 mice. The NP chemistries studied were amphiphilic copolymers of 1,8-bis-(p-carboxyphenoxy)-3,6-dioxaocatane and 1,6-bis-(p-carboxyphenoxy) hexane (CPH) (50:50 and 20:80), and hydrophobic copolymers of CPH and sebacic acid (50:50 and 20:80), each labeled with a different fluorescent dye. Organ distribution after 1h, 12 h, 24 h, 3 d, 7 d and 14 d was studied by XRF image analysis in live animals. Overall, the administration route differentially affected the tissue distribution and tissue residence times. All NPs rapidly dispersed when delivered intranasally but provided a depot when administered by the other routes. When the amphiphilic and hydrophobic NPs were administered intranasally, they persisted (and more so the hydrophobic NPs) within lung tissue (Petersen, Huntimer *et al* 2013).

6.2.2 Copper

Mice were exposed to 23.5-nm copper NPs by nasal instillation every other day for 15 d at daily doses of 1, 10 or 40 mg/kg bw. Copper levels in tissues, determined by ICP-MS on day 17, were approximately doubled in liver, lung and olfactory bulb, compared to control animals. No significant increases were seen after the low and mid doses. Further, no increases were seen in the other tissues examined (spleen, kidney, hippocampus, striatum, cerebral cortex, cerebellum) at any dose level (Zhang, Bai *et al* 2012).

Mice were exposed by intranasal instillation every other day for 19 d to copper NPs (23.5 nm, hydrodynamic size 233 nm) at three dose levels, namely 1, 10, or 40 mg/kg bw. Analyzes by ICP-MS showed significantly increased copper levels in hippocampus, cerebral cortex, cerebellum and striatum after the mid and high doses. The increases over background were generally in the order of 20-30% (Bai, Zhang *et al* 2014).

6.2.3 Iron oxide

Fine ferric oxide (Fe2O3, 280 nm) particles were intranasally instilled in CD-ICR male mice at a single dose of 40 mg/kg bw. The iron distribution and chemical state in olfactory bulb and brain stem were examined 14 d later by synchrotron radiation XRF and x-ray absorption near-edge structure. Iron in the olfactory bulb and the trigeminus of brain stem were clearly increased, suggesting that the particles were transported via uptake by sensory nerve endings of the olfactory nerve and trigeminus (Wang, Feng *et al* 2007).

6.2.4 Latex

The uptake in blood of ^{125}I -labeled, sulfate modified polystyrene latex NPs was studied in rats following intranasal instillation, using a range of particle sizes (20, 100, 500, 1000 nm) and surface coatings (poloxamine, poly-1-lysine, chitosan). ^{125}I was detected with a gamma-counter and particles were detected in the blood already 5 min after dosing. The number of particles in the blood peaked after 60 min and remained constant for 2 h. The 20-nm NPs showed greater uptake than the larger ones. The total maximum uptake of the smallest NPs was in the order of 3% of the dose. The 100-nm NPs coated with chitosan showed an increase in both the extent and rate of uptake, with the concentration in the blood peaking at 15 min rather than at 60 min. The authors suggested that transport of particles across the nasal membrane is due mainly to transcellular transport mechanisms by the nasal associated lymphoid tissue, especially the M-cell like cells. Tissue analyzes revealed that the NPs were mainly taken up by liver and kidneys. The relative distribution to liver increased, whereas for kidneys it decreased, with NP size (Brooking, Davis *et al* 2001).

6.2.5 Manganese oxide

Groups of rats were exposed to 500 µg/m^{3}of manganese oxide NPs (30 nm) via one or both nostrils. Manganese and iron were analyzed in lung, liver, and olfactory bulb and other brain regions. After 12 d of exposure via both nostrils patent, manganese concentrations in olfactory bulb and lung increased 3.5-fold and two-fold, respectively. There were also slight but statistically significant increases in striatum, frontal cortex, and cerebellum. With the right nostril occluded (2-d exposure), manganese increased only in the left olfactory bulb. Solubilization of manganese from the NPs was below 1.5% per day. The authors conclude that the olfactory neuronal pathway is efficient for translocating inhaled manganese oxide NPs to the central nervous system and (based on data not reported herein) that this can result in inflammatory changes. They further suggest that the pathway is relevant also in humans (Elder, Gelein *et al* 2006).

6.2.6 Silica

Rats were intranasally instilled once daily for 1 or 7 d with 10 µg of ^{125}I -labeled silicone oxide NPs per nostril. Samples from different sub-regions of the brain were analyzed by gamma-counting. Both dosing regimens resulted in significant increases in silica with highest levels in the olfactory bulb, followed in descending order by striatum, hippocampus, brain stem, cerebellum and frontal cortex (Wu, Wang *et al* 2011).

6.2.7 Titanium dioxide

Female mice were intranasally instilled with 500 µg of either of two types of titanium dioxide NPs, 80-nm rutile and 155-nm anatase, every other day for 30 d. Brain tissues were collected and analyzed for titanium by ICP-MS after 2, 10, 20 and 30 d. Titanium levels increased in a time-dependent fashion in all examined sub-regions of the bran (olfactory bulb, cerebral cortex, hippocampus, and cerebellum). After 30 d, the increases were 2 to 4-fold over background levels of titanium (Wang, Liu *et al* 2008).

Female mice were intranasally instilled with 500 µg either of four types of titanium dioxide (rutile) particles: uncoated, hydrophobic (10x40 nm and 1 µm) and silica-coated, hydrophilic (10x40 nm and 50 nm). Titanium contents in sub-brain regions were measured by ICP-MS. Titanium increased significantly in the cerebral cortex and striatum after dosing with the hydrophilic NPs. Dosing with hydrophobic NPs resulted in an increase in striatum only, whereas no increases in the brain regions were seen after dosing with the 1-µm particles. These results suggest that size, shape and surface modification affects the nose to brain transport (Zhang, Bai *et al* 2011).

6.2.8 Conclusions – intranasal instillation

Numerous experimental studies with rodents show that NPs can be absorbed by the olfactory mucosa in the nose and transported in significant amounts via the olfactory bulb and other parts of the brain. Limited data suggest that the uptake into brain is dependent on NP size and other properties. In particular, smaller NPs are more prone to uptake than bigger particles. The uptake into brain is difficult to express in quantitative terms, however, one study suggest that the systemic uptake (into blood, not brain) of small (20 nm) latex particles is around 3% (Brooking, Davis *et al* 2001). The nose to brain route is likely relevant also for humans, although it is difficult to assess in quantitative terms.

6.3 Intraperitoneal administration

6.3.1 Aluminum

Male rats were given single *ip* injections of aluminum oxide NPs (Al2O3, 10 nm) at three near lethal (3.9, 6.4 and 8.5 g/kg bw, 48-h LD50 calculated to 12.9 g/kg) doses. The bioaccumulation of aluminum in various organs was measured 48 h later by ICP-AES after acid digestion. Compared to unexposed controls, the aluminum concentration was elevated in a dose-dependent manner, by 1.5- to 7-fold in brain, 2- to 3-fold in liver, 7- to 12-fold in kidney, 1.2- to 3-fold in intestine, and 13- to 14-fold in spleen, compared to control rats. Another group of rats were given two sublethal *ip* doses of 1.3 g/kg bw with 2 d interval and animals were sacrificed after 1, 3, 7, 14 and 28 d. Increases in tissue aluminum over time were evident, 1.8- to 16-fold in brain, 3- to 10-fold in liver, 8- to 30-fold in kidney, 12- to 22-fold in intestine, and 25- to 55-fold in spleen, compared to controls (Morsy, El-Ala *et al* 2016).

6.3.2 Carbon nanotubes

Athymic nude, male mice were exposed to single-walled CNTs (average length 42 nm, bundles of 1-20 nm thickness, dose 0.12 mg) labeled with yttrium-86 by *ip* injection.

The biodistribution was examined by PET at 3 and 24 h post-injection. The animals were sacrificed after 24 h and the distribution to kidneys, liver and spleen was further analyzed with a gamma counter. Yttrium-86 cleared from blood within 3 h and distributed predominantly to the kidneys (8% of injected dose after 3 h by PET, 7% after 24 by PET, 13% after 24 h by gamma-counting), liver (7%, 8%, 6%), spleen (9%, 7%, 7%), and bone (2%, 2%, -). Although the activity that accumulated in kidney and spleen decreased with time, the whole-body clearance was slow (McDevitt, Chattopadhyay *et al* 2007).

6.3.3 Gold

Female mice were given 40-nm gold NPs *ip* and gold was traced after 1, 4 and 24 h by AMG. NPs were found in macrophages only, and at moderate exposure primarily in the Kupffer cells in the liver. The *ip* injections were followed by a delayed uptake in the liver and included a moderate uptake in macrophages located in mesenteric lymph nodes, spleen and small intestine. Ultrastructurally, the AMG silver enhanced nanocrystals were found in lysosome-like organelles of the Kupffer cells and other macrophages wherever located. Accumulations of gold nanoparticles were not found in any other organs analyzed (kidney, brain, lung, adrenal, ovary, placenta, ad fetal liver). The authors concluded that the gold NPs are taken up by endocytosis, primarily by Kupffer cells in the liver and secondarily by macrophages in other places, and they do not seem to penetrate the placenta and blood-brain barriers (Sadauskas, Wallin *et al* 2007).

Gold NPs (12.5 nm) were administered *ip* daily at three doses (40, 200, and 400 µg/kg/d) for 8 d. The animals were sacrificed 1 d after the last dosing and gold in brain, kidney, liver, spleen, lung and blood was determined by AAS. The gold levels in these tissues increased with dose in all examined tissues indicating efficient uptake, however, the increases were in general less than proportional to dose, suggesting saturable distribution kinetics. Especially in blood the deviation from dose-proportionality was marked. Although gold in brain was one to two orders of magnitude lower than the levels in kidney, liver, spleen and lung, but clearly elevated over the background level. Moreover, gold levels in brain and blood were similar, suggesting that the gold detected in brain tissue cannot be explained by residual blood. Altogether, this suggests that the gold NPs were able to cross the blood-brain barrier (Lasagna-Reeves, Gonzalez-Romero *et al* 2010).

6.3.4 Fullerenes

A suspension of C60 fullerenes were given *ip* (0.5 ml/20 g, corresponding to 2.5 g/kg bw) to mice in a study aimed at developing an HPLC-UV assay method. Fullerenes were measured in blood, liver and spleen, 1, 2 and 6 d after dosing. The fullerenes disappeared quickly from blood (179 mg/l day 1, 88 mg/l day 2, 1.1 mg/l day 6), disappeared slowly from liver (0.7 -0.4% of dose) and increased in spleen (0.5-2.4% of dose) (Moussa, Pressac *et al* 1997).

In another study aimed to investigate the acute toxicity and antioxidative effects, suspended micronized C60 fullerenes were given as a single *ip* dose (0.5 kg/kg bw) to rats. Fullerenes in liver remained relatively stable for 1 wk at 7-17 mg/liver,

corresponding to 10-24% of the injected dose and decreased to 5% of the dose on day 9 and 1% on day 14 (Gharbi, Pressac *et al* 2005).

6.3.5 High-density lipoprotein

High-density lipoprotein (HDL) NPs (8-12 nm) labeled with super paramagnetic iron-59 oxide NPs (SPIOs) or quantum dots were injected *iv* or *ip* into ApoE knockout mice and radioactivity was measured using a gamma counter. DLS measurements revealed that the HDL-NP size was unaffected by the internalization of quantum dots or SPIOs. HDL-NP accumulation within atherosclerotic plaques in vivo and ex vivo was estimated by MRI, ex vivo confocal fluorescence microscopy, XRF microscopy, and histological analysis. Blood concentration time curves showed a rapid decrease the first hour after *iv* injection, but a slow increase after *ip* injection. For both routes the amount in blood remained stable between 1 and 4 h at around 10% of the dose Radioactivity measurements showed a similar predominant accumulation in the liver and spleen after both administration routes, increased levels in intraperitoneal macrophages (*ip* route only) and NP uptake into atherosclerotic plaques (more after *ip* compared to *iv*) (Jung, Kaul *et al* 2014).

6.3.6 Iron oxide

Aqueous suspensions of 10, 50 nm magnetite (Fe3O4) NPs and 1000 nm particles were injected *ip* to rats (500 mg/kg) three times per week for 5 wk. The iron content of the blood was measured photometrically, and that of the liver and the spleen AAS and electron paramagnetic resonance (EPR). Iron levels in blood were approximately doubled after 10-nm and tripled after 50-nm but unaffected after dosing with 1000-nm particles. Similarly, the levels in liver and spleen increased approximately 5-fold for the NPs but were similar to control for the bigger particles (Katsnelson, Degtyareva *et al* 2011).

6.3.7 Polymers

Thoracic duct cannulated rats were given carbon-14 labeled polyhexylcyanoacrylate (PHCA, 543 nm) or polymethylmethacrylate (PMMA, 1.4 nm) NPs by *ip* administration. For PHCA, the radioactivity in blood tended to decrease during the 4-h sampling period, from 0.2% to 0.1% of the absorbed dose. Conversely, the amount in lymph (thoracic duct) increased over time, reaching 0.6% after 4 h. Levels in main organs after 4 h were: spleen 0.7%, liver 0.6%, kidneys 0.8%, diaphragm 1.2%, heart 0.6% and lungs 0.4% of the absorbed dose. Substantially lower amounts were found for PMMA in blood and lymph as well as in all organs tested (Maincent, Thouvenot *et al* 1992).

Kobayashi *et al* studied the biodistribution in mice of *ip* given a single dose of avidin-gadolinium dendrimers (size not stated, dose 1 µg gadolinium per mouse corresponding to 50 µmol/kg bw). Avidin is a biotin-binding protein that is quickly internalized in tumor cells. Gadolinium emits Auger electrons after irradiation with a neutron beam, this causes strong cytotoxicity but only when Gd(III) is present inside the cell. The NPs were constructed by combining avidin and biotin with a generation-6 polyamidoamine dendrimer, followed by saturation with Gd(III). Studies in vitro showed that the

dendrimers were efficiently internalized by SHIN3 cells (a human ovarian cancer). The biodistribution study was performed with nude mice bearing *ip* disseminated SHIN3 tumors. Blood, tumors, and organs were removed and radioactivity was measured with a gamma-counter. Gadolinium showed an overwhelming preference for tumor cells with one to three orders of magnitude higher concentrations, compared to other tissues (Kobayashi, Kawamoto *et al* 2001).

6.3.8 Quantum dots

The distribution of captopril-conjugated quantum dots (QDs-cap, core CdSe, shell ZnS, 13.5 nm) was evaluated in male ICR mice following *ip* injection of 0.68 mg (18 mg/kg, 50 nmol Cd) by ICP-MS and confocal microscopy coupled with spectrometric analysis. At 6 h post-injection the QDs were mainly located in blood (8.8% of the dose), liver (2.3%), spleen (1.6%) and kidneys (0.7%), but a small amount (0.1%) was found in various regions of the brain. The QDs were located predominantly inside the blood vessels in the liver, kidney and brain, but a few were distributed in the parenchyma, especially noteworthy in the brain strongly suggesting passage of the blood-brain barrier (Kato, Itoh *et al* 2010).

6.3.9 Selenium

Elemental selenium NPs (50 nm, 0.7 mg/kg bw) were *ip* injected in mice previously inoculated with highly malignant H22 hepatocarcinoma cells. The mice were sacrificed after 3, 6 and 12 h and tissues were analyzed for selenium by TEM. Selenium level was only slightly elevated in blood, whereas approximately 4-fold and 40-fold increases over background were seen in liver and H22 cells, respectively, at 3 h post-dosing. The selenium levels decreased over time in all three tissues and reached half their values after 12 h (Wang, Sun *et al* 2014).

6.3.10 Silica

The biodistribution in male Kun Ming mice of 27-nm silica NPs was determined by ICP-AES after *ip* injection of 20 mg/kg bw. Elevated silica levels compared to background were seen in liver, spleen, lung and kidney, but not in heart and brain. Co-exposure to silica NPs and cadmium chloride markedly increased the cadmium accumulation in the liver. In vitro binding assays indicated that serum albumin and cadmium ions (Cd2+) mutually enhanced the binding of each other to the silica NPs via the interaction of serum albumin and Cd2+. The uptake of cadmium-bound silica NPs by macrophages can explain the increased cadmium accumulation in the liver (Guo, Xu *et al* 2013). The total systemic uptake, estimated by summing the amounts in the major organs, is less than 0.1% of the dose

6.3.11 Silver

Female BALB/c mice were exposed twice per week for 4 wk to 22 or 108 µg/kg bw of PVP-coated silver NPs (25 nm) or to 108 mg/kg bodyweight of silver ions (as silver nitrate) via the *ip* route. Silver in tissues was determined by ICP-MS. The silver was predominantly localized in liver and spleen, and more so after dosing with nanosilver compared to silver nitrate. The investigators also demonstrated that the silver crossed the placental barrier and accumulated in fetuses. Administration of a higher dose (1.3 mg/kg

twice weekly for 4 wk) to male mice showed a similar preference for liver and spleen and, in addition, accumulation in the testes. These results suggest that silver NPs may pass the blood-placenta and blood-testis barriers, however, the contribution of dissolution of silver from the NPs is unclear (Wang, Qu *et al* 2013).

6.3.12 Titanium dioxide

Mice were given titanium dioxide NPs (100 nm) by a single *ip* injection at doses ranging from 324 to 2592 mg/kg bw. Distribution to various tissues was determined after 24 h, 48 h, 7 and 14 d by ICP-MS. After 24 h, the titanium was almost exclusively located in then spleen, but at later stages some was also found (in falling order) in liver, lung, kidney and heart. The passage of titanium dioxide NPs to the spleen was also verified by histopathological examinations. The tissue titanium levels were generally not dependent on the dose. It can be estimated that titanium in the tissues amounts to approximately 0.1-1% of the dose (Chen, Dong *et al* 2009).

6.3.13 Zinc oxide

Male ICR mice were *ip* injected with zinc oxide NPs (50 nm, slice-shaped) or microparticles (minimum 122 nm, average 1200 nm) at doses of 2.5 g /kg bw. Titanium was measured in serum after 2-72 h and in organs after 24-72 h by ICP-MS. Zinc in serum reached about 15 and 20 µg/g after microparticles and NP administration, respectively. Higher zinc levels were also found in the organs of mice give NPs compared to microparticles. Meanwhile, for both particle types the concentrations were highest in liver followed by spleen, lung, kidney and heart. These data suggest that the nanosized particles are more efficiently translocated from the *ip* space to the circulation and from the circulation to the organ, than the microsized particles. The total increase of zinc in the organs corresponded roughly to 1% of the administered dose (Li, Shen *et al* 2012).

6.3.14 Conclusions – intraperitoneal absorption

Most studies on NPs with *ip* administration have used mice as the test species. This is not surprising, since the *ip* route is commonly used in mouse experiments. The studies were generally not primarily designed to study the systemic uptake and biodistribution. Nevertheless, some studies report organ levels of NPs in a way that make it possible to roughly estimate the systemic uptake.

As seen in Table 6, this uptake varies widely, from less than 0.1% for gold NPs to 50% of the dose for nanographene. There is no obvious relation with composition, shape, size or dose of the NPs; however, these factors have not been systematically investigated. Possible exceptions are those of titanium dioxide and zinc oxide NPs. For titanium dioxide, the per cent uptake was much lower after a high compared to a low dose, suggesting saturation kinetics. For zinc oxide, slightly higher tissue level were reached after dosing with nanosized compared to microsized particles, suggesting enhanced peritoneal translocation and tissue distribution for the smaller sized NPs.

With respect to biodistribution, the same major pattern is seen as with other exposure routes, namely accumulation mainly in liver and spleen and to some extent in kidney and lung. More detailed analysis of the distribution pattern is not possible, there seems to quite a wide fluctuation in distribution, even within the same studies.

Table 6. Systemic absorption of nanoparticles following intraperitoneal administration.

Nanoparticle	Size (nm)	Zeta potential [1]	Dose [2] (mg/kg bw)	Species	Systemically absorbed (% of dose)	Reference
Carbon nanotubes, single-walled (SWCNT)	1-20 x 42	ns	0.12 mg per animal	Mouse	>25%	McDevitt, Chattopadhyay *et al* 2007
Gold	12.5	–	0.04 3	Mouse	<0.1%	Lasagna-Reeves, Gonzalez-Romero *et al* 2010
Fullerenes, C60	0.7	ns	2500	Mouse	>2.5%	Moussa, Pressac *et al* 1997
Fullerenes, C60	0.7	ns	500	Rat	10-24%	Gharbi, Pressac *et al* 2005
Graphene oxide, PEGylated PEGylated, reduced PEGylated, reduced	1x25 5x60 6x25	ns	50	Mouse	30% 50% 25%	Yang, Gong *et al* 2013
Graphene oxide, PEGylated, reduced	1-6 x 25-50	ns	100	Mouse	>40%	Yang, Gong *et al* 2013
Graphene oxide, PEGylated, reduced	1-6 x 25-50	ns	100	Mouse	>40%	Yang, Gong *et al* 2013
Silver, PVP-coated	25	ns	0.022 [3] 0.108 [3]	Mouse	<1%	Wang, Qu *et al* 2013
Silica	27	–	20	Mouse	1% 0.1%	Chen, Dong *et al* 2009
Titanium dioxide	100	ns	324 2592	Mouse	1% 0.1%	Chen, Dong *et al* 2009
Zinc oxide	50 1200	ns	2500 2500	Mouse	<0.1%	Li, Shen *et al* 2012
Quantum dots	13.5	ns	18	Mouse	>13.5%	Kato, Itoh *et al* 2010
Polyhexylcyanoacrylate (PHCA)	543	ns	0.75	Rat	>5%	Maincent, Thouvenot *et al* 1992

Nanoparticle	Size (nm)	Zeta potential [1]	Dose [2] (mg/kg bw)	Species	Systemically absorbed (% of dose)	Reference
Polymethylmethacrylate (PMMA)	1.4	ns	2.5	Rat	>2.5%	Maincent, Thouvenot *et al* 1992

[1] ns – not stated.
[2] Single dose if not otherwise stated.
[3] Repeated daily for 8 d.

6.4 Intramuscular administration

Fluorescent carbon dots (3 nm) were synthesized and their clearance from the injection site after *iv*, intramuscular and subcutaneous injection in mice was investigated by measurements in blood, tumors and urine using NIRF and PET imaging techniques. The carbon dots were taken up efficiently and rapidly excreted from the body after all three injection routes. Among the three routes, the uptake was, as expected, fastest after *iv* and slowest after subcutaneous injection. After 24 h, no significant signal was detected in any organ, suggesting that these particles were cleared out of the body regardless of the injection route (Huang, Zhang *et al* 2013).

The in vivo distribution and persistence of various polyanhydride NPs was studied after subcutaneous, intramuscular and or intranasal administration to hairless mice. All NPs rapidly dispersed when delivered intranasally but provided a depot when administered parenterally (Petersen, Huntimer *et al* 2013). See section Intranasal administration for more details.

6.5 Ocular administration

The highly sensitive interior of the eye is protected from the external environment by tight junctions in the corneal epithelium and by the mucosal surface. Moreover, the eye is separated from the rest of the body by multiple layers of biological barriers. Much research has been carried out with different types of nanomaterials to improve the ophthalmic delivery of drugs, *ie* to circumvent the protective barriers to achieve therapeutically effective concentrations of drugs in the intraocular space. Various nanomaterial-based ocular drug delivery systems have been investigated, including *eg* polymeric micelles, hydrogels, liposomes/niosomes, dendrimers and cyclodextrins. These systems generally use hydrophilic and lipophilic phases (*eg* liposomes) and steric conformations (cavities), allowing for the drug molecules to be dissolved and stored inside the nanomaterial.

Several of these drug-delivery systems are already in clinical practice or in pre-clinical phases. For review see, *eg* (Liu, Jones *et al* 2012).

7 Tissue distribution, excretion and accumulation

Upon systemic absorption, such as after *iv* injection, NPs as well as nanosized molecules enter the vascular system and distribute with the blood flow organs and peripheral tissues. In blood, the NPs come in contact with various types of plasma proteins, coagulation factors, platelets, and red and white blood cells. Depending on the size and charge, the NPs may undergo adsorption or opsonization (binding to antibody) by serum proteins. In addition to enhancing particle recognition by the host immune system, the adsorption/opsonization of NPs increases the effective size of the particle resulting in a so called in vivo hydrodynamic diameter. The hydrodynamic diameter may be considerably larger than the in vitro diameter of the “naked” NP and affects the clearance from blood to organs and to urine. Generally speaking, a larger hydrodynamic diameter lowers the blood clearance and the glomerular filtration rate and thereby increases the biological half time (Longmire, Choyke *et al* 2008).

The endothelial cell layer lining the blood vessels serves as a semi selective barrier that controls the exchange of fluid and macromolecules between blood and extravascular space. The structure of the endothelium differs between tissues, however, effective pore size in normal intact endothelium is about 5 nm, as shown with QDs by Choi *et al* (Choi, Liu *et al* 2007) (see section on Quantum dots later in this chapter). Thus, NPs with a hydrodynamic diameter below 5 nm rapidly reach equilibrium with the extravascular extracellular space, whereas larger NPs have longer circulatory times due to slower transport across the endothelium. The endothelium of the lymphatic vessels has slightly larger fenestrae, accepting NPs up to 6 nm in diameter (Longmire, Choyke *et al* 2008).

There are numerous studies describing the biokinetics of NPs following *iv* administration, whereof a few illustrative ones are described in the following. More studies are summarized *eg* in the review by Lin *et al* (Lin, Monteiro-Riviere *et al* 2015). The *iv* route is not relevant for environmental exposures per se, but is obviously important for nano-based products for internal use (such as *iv* drugs and medical implants). *Iv* studies are also useful to understand tissue distribution in different species and the dependence on NP properties.

7.1 In vivo studies

7.1.1 Carbon

Carbon nanohorns (100 nm) labeled with gadolinium oxide and coated with DSPE-PEG were injected in the tail vein of male mice at single dose of 5 mg/kg bw. The concentration of nanohorns dropped quickly in blood during the first 24 h post-injection, with a half-time of 5-6 h. The amount of nanohorns was highest in liver and spleen. In liver, the amount increased from 22% of the injected dose after 1 h to a maximum of 70% after 24 h. Thereafter, the amount in liver declined slowly to about 30% at 30 d post-injection, with little further decline up to 120 d. In spleen, the amount increased from 6% to 10% in the same time frame. A few percent were also detected in intestine, skin, kidney, and “others” (percentages estimated from figure 3 in Zhang *et al*

The recovery in whole mice dropped from 95-100% during the first 24 h to 60% after 30 d and 120 d. However, only 15% of the dose was recovered in feces. The remaining 25% was inferred to by the authors to be partly or completely degraded in the liver (Zhang, Tahara *et al* 2014).

7.1.2 Chitosan

Tritium- and FITC-labeled amphiphilic N-octyl-O-sulfate chitosan (65 000 Da) was injected in the tail vein of mice (13 mg/kg bw). The AUC in plasma was proportional to dose over the tested range (4-17 mg/kg bw), likewise the half-time in plasma (17-18 h) was independent of dose, suggesting linear dose-independent kinetics. The highest amounts of chitosan (up to 10% of the dose) were seen in kidney (up to 10% of the dose) and plasma (up to 5%), but chitosan was also detected up to a few per cent in all other organs examined. Excretion studies with S-D rats showed that about 15% of the dose was excreted via bile in 36 h. Urinary excretion was the predominant way of excretion, with 75 % of the dose excreted in 7 d (Zhang, Qu *et al* 2008).

7.1.3 Fullerenes

The biodistribution of C60 fullerenes (30-200 nm) was studied by LC-MS/MS at day 1, 7, 14 and 28 after tail vein injection in rats. Fullerenes were detected in various tissues (but not in blood), with highest concentrations in lung (174 µg/g tissue), followed by spleen (57 µg/g), liver (21 µg/g), kidney (1.3 µg/g), and brain (0.05 µg/g tissue, average concentrations for comparison only). Most fullerenes (roughly 80-95%) of fullerenes were found in lung and liver, these two organs corresponded to about 30-50% and 50-60%, respectively, of the body burden. The high amounts in lung and absence in blood suggest that the fullerenes are effectively cleared from blood by filtering in the lung capillary vessels. Different time courses in concentration were observed, a faster decrease in kidney and brain (half-time in the order of 1 wk), slower in liver and lung (1 month), and no decrease in spleen. Overall, the results suggest that unmodified and or metabolized fullerenes are excreted from the body (Kubota, Tahara *et al* 2011).

7.1.4 Gold

The biodistribution of gold-dendrimer composite nanodevices (CNDs) of different size surface charge (5 nm positive, negative, neutral; 22 nm positive; 11 nm negative) was studied in male, tumor-bearing C57BL/6J mice following *iv* injection in the tail vein. Gold in tissues was determined by instrumental neutron activation analysis. The tissue distribution clearly depended on the size and surface charge. For the 5-nm positive CNDs, the highest concentrations were found in blood, followed by kidney and blood. For the 5-nm negative and neutral CNDs, the order was liver>spleen>blood. For the 22-nm positive CNDs on the other hand, the order was lung>spleen>liver, whereas that of the 11-nm negative was spleen>liver>heart. The excretion also depended on size and charge, with the highest excretion for small and positive nanodevices. Thus, the amounts of 5-nm nanodevices excreted in 5 d were 46% of the dose for the positive *vs* 14% for the negative and neutral ones. With respect to size, the 5-nm positive exhibited higher excretion (46%) than the 22-nm (17%). However, the negative nanodevices showed an opposite pattern, 14% excreted for the 5 nm *vs* 6% for the 11 nm (Balogh, Nigavekar *et al* 2007).

Citrate-coated gold NPs (mainly 15, 50, 100 and 200 nm) were given *iv* to mice (1 g/kg bw) and blood and organs were analyzed after 24 h by ICP-MS. NPs of all sizes were found mainly in liver, lung and spleen. The biodistribution was size-dependent, thus the 15-nm NPs hade the most widespread distribution whereas the 200-nm particles generally had the lowest presence in blood and major organs. For example, the amounts measured in liver after 24 h were: 15 nm – 0.4%, 50 nm – 0.08%, 100 nm – 0.11%, 200 nm – 0.14%. A similar size-dependence was seen for brain (0.08%, 0.04%, 0.02% and 0.0003% of the dose after 24 h) (Sonavane, Tomoda *et al* 2008).

Gold-198 labeled monodisperse, negatively (1.4, 2.8, 5, 18, 80, and 200 nm) and positively (2.8 nm) charged gold NPs labeled with 198Au were given *iv* to rats. The biodistribution was determined by gamma-spectrometry 24 h post-injection. The size and surface charge of the NPs strongly determined the distribution. Most NPs accumulated in liver with a strong size-dependence (1.4 nm 51%, 2.8 nm 82%, 5-200 nm 92-97% of the dose at 24 h). Much smaller fractions were distributed to other organs and generally less, the larger the NP size. Notable exceptions to this trend were spleen, with the highest retention for the 2.8-nm NPs, and blood, with highest retention for the smallest and largest NPs. The biliary clearance was also strongly size-dependent (1.4 nm 5%, 2.8 nm 1%, 5 nm 0.6%, 18 nm 0.5%, 80 nm 0.4%, 200 nm 0.1% of the dose excreted in 24 h). The positively charged 2.8-nm NPs had a slightly different biodistribution profile with significantly lower retention in liver and lower excretion in urine but higher levels in spleen, heart and kidney and higher biliary clearance. The authors concluded that the size and charge-dependent differences in biokinetics are mediated by dynamic protein binding and exchange (Hirn, Semmler-Behnke *et al* 2011).

Gold NPs (25 nm, 0.36 mg/kg bw) suspensions were administered orally and *iv* to male Wistar rats. Exretion in feces and urine was followed for 10 d, whereafter the major organs were collected and analyzed for gold by ICP-MS. Following oral administration 60% of the dose was excreted in feces and urine and a total of 1.4% was recovered in the major organs, showing that only a small amount was absorbed. In contrast, after *iv* dosing the gold NPs were largely retained in the body (59%). The NPs were mainly found in liver (51% of dose), lung (5.7%) and spleen (2.0%) and only a small amount (2.9%) was excreted (Bednarski, Dudek *et al* 2015).

Female Balb/c Mice were *iv* injected with four types of functionalized gold NPs (cores 2.0, 2.1, 1.8 and 2.0 nm, hydrodynamic diameters 10, 9, 14 and 7 nm, zeta potentials +21, +17, -0.8 and -41 mV). The organ distribution was determined 24 h after dosing by quantitative imaging based on laser ablation ICP-MS. The highest concentrations of NPs were generally achieved in spleen, followed by liver and lung. However, the organ distribution pattern differed considerably with type of NP, showing that both surface charge and size affects the biokinetics. For example, the positive NPs had relatively higher concentration than the neutral and negative NPs in spleen, liver, lung and kidney, whereas neutral NPs had the highest 24-h concentration in blood. Comparative analyzes of the distribution within organs showed that the positive NPs accumulate extensively in the kidney glomeruli and in liver hepatocytes, whereas uncharged NPs accumulate to a greater extent in the white pulp and marginal zone of the spleen and in Kupffer cells in the liver (Elci, Jiang *et al* 2016; Elci, Yan *et al* 2016).

7.1.5 Iron oxide

The biokinetics of 56Cr-labeled super paramagnetic iron oxide NPs (11 nm core) and 65Zn-labeled QDs (CdSe/CdS/ZnS, 5.5 and 7 nm) were studied in mice after *iv* injection. At 2 h after dosing, the iron oxide NPs were mainly taken up by liver (90% of dose) and spleen (4%). After 4 wk, the radioactivity from 56Cr was mainly found in spleen, followed by liver. The organ distribution of 56Cr-iron oxide NPs was clearly different after a similar injection of chromium (III) ion (CrCl3). This contrasted the biokinetics of the 65Zn-Qds which were quite similar to that of zinc ion (ZnCl2) with decay curves in blood having similar half times of 41 d *vs* 35 d for the third, slowest phase (Bargheer, Giemsa *et al* 2015).

7.1.6 Polycaprolactone

The biodistribution of PEGylated poly-ε-caprolactone NPs (138 nm initially, 13 nm after 160 h of degradation in cell medium) covalently labeled with rhodamine B was studied by fluorescence spectrometry in melanoma-bearing mice. The *iv* dose was 1.5•1014 NPs per kg bw or 3•1012 NPs per mouse (dose in mg not given). The disappearance of NPs from plasma was biphasic, with half-times of 30 min and 15 h. The amounts of NPs in liver and tumor remained stable from day 1 to 7 post-injection. About 70% and 1% of the NPs were excreted in feces and urine, respectively, after 72 h, whereas 10% remained in spleen, 2% in liver, 1.5% in tumor and 0.4% in plasma (Lupi, Colombo *et al* 2014).

7.1.7 Quantum dots

Differently sized QDs (2.8-4.3 nm, CdSe core, ZnS shell) were coated with dihydrolipoic acid, dihydrolipoic acid conjugated to PEG, cysteine or cysteamine and labeled with ^{99m}Tc (hydrodynamic diameter 4.4-8.7 nm). These neutral and zwitterionic coatings were used to prevent adsorption of serum proteins and hence allow for renal excretion. The QDs were administered *iv* to ICR mice and levels in blood was followed for 4 h by tail vein sampling. Thereafter, the amounts in tissues and carcass were determined by gamma counting and radioscintigraphy. The renal excretion was clearly size-dependent with excreted amounts (as % of dose) in x h as follows: 4.4 nm 75%, 5.0 nm 65%, 5.5 nm 45%, 6.7 nm 25%, 8.7 nm 20%. The differences in excretion were reflected as different decay curves in plasma with half-times ranging from 48 min to 20 h (Choi, Liu *et al* 2007).

The blood and tissue biokinetics of QD705 (CdTe core, ZnS shell, methoxy-PEG-5000 coating, 13 nm) were studied up to 28 d in mice by ICP-MS(cadmium) and fluorescence light microscopy after single *iv* doses of 40 pmol (60 µg) revealed the localization of QD705 in tissues. The plasma half-life of cadmium was 18.5 h, meanwhile the levels persisted or continued to increase in liver (29-42% of the dose), and kidney1.5-9%) and spleen (4.8-5.2%) during the 28 d. No fecal or urinary excretion was detected. Fluorescence microscopy confirmed deposition of QDs in the liver, spleen, and kidneys. The authors concluded that QD705 has a very long half-time, potentially weeks or even months (Yang, Chang *et al* 2007).

Male ICR mice were given water-soluble, hydroxyl silica-coated CdSeS QDs by a single *iv* dose (21 nm, 5 nmol/mouse). Cadmium content in tissues was determined by

ICP-MS at different time intervals. In addition, the aggregation state in tissues was investigated by differential ultracentrifugation. The plasma half-time and clearance of QDs were 20 h and 57 ml/h/kg, respectively. Liver (48% of dose after 6 h), kidney (18%), spleen (2.4%) and lung (2.2% after 12 h) were major target organs. After 5 d, the QDs metabolized in three paths depending on their distinct aggregated states in vivo. A fraction of unbound, nonaggregated QDs, were rapidly excreted by glomerular filtration (24% of the dose in 5 d). However, 9% remained in the liver as aggregated QDs and it was difficult for this fraction to clear (Chen, Chen *et al* 2008).

The biodistribution of QDs (Ag2S, 5.4 nm) coated with dihydrolipoic acid (10 nm) and PEG (70 nm) was studied after single *iv* doses of 15 mg/kg bw in female Balb/c mice. Silver in tissues was determined by ICP-MS up to 60 d post-injection. The initial half-time in blood (first 24 h) was 3.6 h. The QDs mainly accumulated in the liver (52 µg/g day 7) and spleen a(43 µg/g day 3) and was gradually cleared, mostly by fecal excretion (Zhang, Hong *et al* 2013).

7.1.8 Silica

Near-infrared fluorescent mesoporous silica NPs were incorporated with the near-infrared fluorescent dye indocyanine green via covalent or ionic bonding, to obtain similar NPs (80 nm) but with opposite surface charge (+34 mV and -18 mV at pH 7.4, respectively). The biokinetics in *iv* injected mice were studied by in vivo fluorescence imaging and by ICP-MS. The positive NPs were quickly excreted via the biliary route (clearance onset <30 min), while the negative ones remained within the liver (clearance onset >3 d). The authors suggest that charge-dependent adsorption of serum proteins greatly facilitates the hepatobiliary excretion (Lee, Cheng *et al* 2009; Souris, Lee *et al* 2010).

The biokinetics of FITC-labeled monodisperse spherical mesoporous silica NPs (PEGylated and nonPEGylated, 80, 120, 200 and 360 nm) were investigated in ICR mice. Organs were sampled at 30 min, 1 d, 5 d and 1 month after *iv* injection in the tail vein and analyzed by fluorescence spectrometry. All types of tested NPs distributed mainly to the liver and spleen, some to lung and a few to kidney and heart. The smaller size PEGylated NPs remained in the blood circulation for a longer time, were degraded more slowly, and were to a lesser extent excreted in urine and captured by liver, spleen, and lung. When tested in S-D rats, the mean residence times (MRT) where longer for smaller NPs and for PEGylated NPs. The MRTs for PEGylated and nonPEGylated NPs, respectively, were: 2.3 and 2.0 h (80 nm), 1.9 and 1.8 h (120 nm), 1.8 and 1.3 h, and 1.5 and 1.2 nm (360 nm) (He, Zhang *et al* 2011).

The biokinetics of two differently shaped fluorescent mesoporous silica NP (aspect ratios 1:1.5 and 1:5) were investigated by ICP-OES after *iv* injection in mice. The NPs were mainly (>80% of dose) found in spleen and lung, liver and kidney, with clear differences between the two shapes. Thus, the short-rod NPs were preferentially trapped in the liver, and the long-rod NPs in the spleen. For both shapes, higher amounts were found in lung after PEGylation. Regarding excretion, the short rod had a more rapid clearance via both urine and feces (Huang, Li *et al* 2011).

The absorption, distribution, excretion and toxicity in mice of mesoporous silica NPs (110 nm) doped with FITC were compared for four different exposure routes: *iv* (50-800 mg/kg bw), hypodermic (50-1800 mg/kg bw), intramuscular (50-2400 mg/kg bw) and oral (50-5000 mg/kg bw). The NP distribution in organs was determined 1 d and 7 d after dosing by measurement of silicon with ICP-OES. However, the silicon levels in organs were only marginally increased over background after hypodermic, intramuscular and oral dosing, as only small fractions of the dose were systemically absorbed (Fu, Liu *et al* 2013).

Male Balb/c mice were *iv* injected with paramagnetic silica- iron oxide NPs (26 nm, 100 µg), whereafter the distribution to different organs was followed up to 84 d by MRI, ICP-MS, XRF and X-ray absorption near edge structure spectroscopy. The NPs mainly accumulated in the liver, and were retained there the whole observation period. The organ distribution (as per cent of the dose) at day 7 and 84 were as follows; liver – 72% and 76%, spleen – 6% and 10%, 4% and 3%, lung 1% and 0%. The NPs retained their core-shell structure during the whole observation period. (Smulders, Ketkar-Atre *et al* 2016).

7.1.9 Silver

Silver NPs (20 and 200 nm, 5 mg/kg bw) were given *iv* to male Wistar rats. Tissues, urine and feces were was sampled 24 h, 7 d and 28 d post-injection and analyzed by ICP-MS for silver and by TEM. The NPs translocated from blood to the main organs (by TEM analyzes) and silver in tissues and excreta were significantly higher in rats given 20 nm compared to 200 nm NPs. Twenty-four hours after dosing with the 20-nm NPs, the highest concentration of silver was found in liver followed by spleen, kidney, lung and brain. After 7 d, the order was lung>liver>spleen>kidney>brain, and after 28 d it was kidney>liver>lung>spleen>brain, suggesting redistribution. The silver concentration in the kidneys and brain increased during the experiment and reached the highest concentration after 28 d (Dziendzikowska, Gromadzka-Ostrowska *et al* 2012).

The biokinetics of citrate-coated 8-nm silver NPs were investigated in New Zealand White rabbits up to 28 d after a single *iv* injections of 0.5 or 5 mg/kg bw. The half-times in serum were 16 d (low dose) and 12 d (high dose). Accumulation of silver was observed in all tested organs at all days of measurement (day 1, 7, 28), with levels generally in the order liver>spleen>kidney>lung>testis> brain>thymus. Little decrease was seen in the organs from rabbits given the higher dose. Excretion via feces and urine was also monitored during the entire experimental period. Unexpectedly, much more excretion of silver occurred via feces than through urine after an *iv* injection, which suggesting biliary excretion (Lee, Kim *et al* 2013).

Male CD-1(ICR) mice were administered silver NPs of different sizes (10 nm, 40 nm, 100 nm) and coatings (citrate, PVP) and silver acetate by a single *iv* injection of 10 mg/kg bw. At 24 h after doing, silver in organs was measured by ICP-MS. For all NP types, the highest silver concentrations were found in the spleen and liver, followed by lung, kidney, and brain. The silver levels were higher in spleen, lung, kidney, brain, and blood after dosing with 10 nm, compared to 40 nm and 100 nm NPs. The different coatings had little influence on the biodistribution. Dosing with silver acetate yielded higher silver levels in kidney and lower in spleen and lung, compared to 10-nm NPs.

Dissolution of silver from the NPs may influence the biokinetics, and incubation with mouse serum for 24 h resulted in a size-dependent dissolution. However, even for the smallest NPs (10 nm) the dissolution of silver was less than 0.005% (Recordati, De Maglie *et al* 2016).

7.1.10 Titanium dioxide

Titanium dioxide NPs (20 nm, rutile) were labeled with the fluorescent marker CF680 and with iodine-125 and injected *iv* in mice or rats at doses of 10mg/kg bw. The tissue distribution and excretion were investigated up to 30 d post-injection by fluorescence imaging, gamma counting and TEM. The NPs mainly accumulated in liver (21% of dose per g tissue day 1, 12% day 30) and spleen (21%, 6.5%), followed by lung (3.4%, 0.3%) and bone (0.6%, 0.5%). Abouit 40% was excreted in urine and 7% via feces pathway (Xie, Wang *et al* 2011).

7.1.11 Zinc oxide

Gamma-ray emitting zinc oxide NPs (40-100 nm) were produced by neutron activation and injected in the tail vein of isoflurane anesthetized ICR mice (0.12 mg/animal). The distribution to various tissues was measured at 1 h and 24 h post-injection with a gamma counter. The NPs were primarily (1 h) distributed to the lungs and later on (24 h) translocated to intestines and feces (Chen, Shih *et al* 2010).

The comparative biodistribution of 18-nm zinc oxide NPs was studied in rats after single *iv* (3 mg/kg bw) and oral administration (3 and 30 mg/kg). Zinc in blood, urine and feces was monitored daily by ICP-AES for 7 d and tissue distribution was determined in liver, kidneys, lung, spleen, thymus, brain, and testes. The NPs were not readily absorbed after oral administration and were excreted mostly in feces. After the high *iv* dose, the level in blood peaked after 5 min but returned to normal after 48 h. The NPs were distributed mainly to liver, kidneys, lung, and spleen, but zinc levels were not elevated over control in thymus, brain, and testes. The fecal excretion of zinc after *iv* injection supported biliary excretion (Choi, Kim *et al* 2015).

7.2 Passage of blood-brain barrier

The biodistribution and brain concentration of uncoated and differently coated, 14C -labeled polycyanoacrylate particles (137-164 nm) were investigated by radioactivity counting 1 h after *iv* administration of 60 mg/kg bw in mice and rats. PEGylated polycyanoacrylate particles penetrated into the brain to a larger extent than the other particle formulations and reached 3-fold higher radioactivity in the brain compared to uncoated particles. Still, the amounts in brain were small compared to the liver and other major organs and were generally below 0.1% of the injected dose per g tissue. Fluorescence microscopy showed that the particles were localized in the ependymal cells of the choroid plexuses, in the epithelial cells of pia mater and ventricles, and to a lower extent in the capillary endothelial cells of BBB. Measurements of 14C-sucrose diffusion showed that the particle dosing did not disturb the blood-brain barrier (Calvo, Gouritin *et al* 2001; Calvo, Gouritin *et al* 2002).

Negatively charged 65-nm PLA NPs containing ^{125}I -labeled neurotoxin-I were administered intranasally or *iv* to male S-D rats. The latter substance was also given *iv*

in free form for comparison. Brain transport of NPs was investigated by monitoring the radioactivity for up to 4 h in microdialysis samples from the olfactory bulb. The brain uptake of neurotoxin-I was more efficient (35% shorter Tmax and 23% higher Cmax and AUC in dialysate) when given NP-encapsulated compared to the free form and also more efficient (32% shorter Tmax, 66% higher Cmax, 63% higher AUC) when administered intranasally compared to *iv*. The results indirectly show that the PLA NPs are taken up by the olfactory bulb (Cheng, Feng *et al* 2008).

Citrate- and peptide- (CLPFFD) coated 12-nm gold NPs were given *ip* to male S-D rats. The latter NPs have a higher stability and are more hydrophobic due to steric repulsion and lower negative surface charge. Gold in tissues was determined after 1, 2, 4 and 24 h by NAA. The maximum amounts of gold detected in brain were sen after 2 h and corresponded to 0.005% and 0.02% of the dose for citrate- and peptide-coated NPs, respectively. A similar difference was seen for gold in spleen (12% *vs* 16% after 4 h), but the opposite for liver (72% *vs* 37% after 4 h) (Guerrero, Araya *et al* 2010).

Male S-D rats were injected *iv* with glucose-coated 2-nm gold NPs with different additional ligands and labeled with the positron emitter gadolinium-68. The biodistribution was determined by whole body PET imaging and gamma counting of organ samples collected 4 h after dosing. The organ distribution pattern differed widely between the NP types. The uptake in brain ranged from 0.007% (no additional ligand NPs) to 0.02% (Leu-enkephalin ligand) of the injected dose (Frigell, Garcia *et al* 2014).

C57BL/6 mice were exposed to QD aerosol (QD core 1.9 nm, 15-20 nm PEG2-PE micelles 15-20 nm, aerosol droplets 1.8 um) for 1 h. Uptake of NPs in the olfactory tract and axonal transport in the olfactory bulb were (measured 3 h post-exposure) were demonstrated by fluorescence microscopy, TEM (Hopkins, Patchin *et al* 2014).

Elevated NP concentrations in brain after inhalation exposure of rodents have also been demonstrated for various NP types, including carbon (Oberdörster, Sharp *et al* 2004), copper (Bai, Zhang *et al* 2014) after inhalation exposure (see chapter 5), for gold (Sonavane, Tomoda *et al* 2008) after *iv* injection (earlier in this chapter) and for QDs (Kato, Itoh *et al* 2010) following *ip* injection (see chapter 6).

7.3 Conclusions - tissue distribution, excretion and accumulation

Although some experimental studies point in other directions, most studies show that NPs tend to concentrate in liver, followed by spleen, lymph nodes, lung and kidney. The NP distribution pattern agrees well with that of phagocytic cells, mainly Kupffer cells in the liver, monocytes and macrophages in spleen and lymph nodes, and histiocytes in various organs. All these cell types make up the mononuclear phagocytic system. The similar patterns show that phagocytosis plays a major role in the biodistribution of NPs.

As soon as the NPs have entered the body, they are rapidly circulated to different organs where they are translocated by diffusion and or endocytic processes and eventually accumulated and/or eliminated, the latter by metabolism, degradation, dissolution and/or excretion. Passage of the blood-brain barrier and uptake in various regions of the brain has been demonstrated for a variety of NP types and exposure routes. The uptake in

brain is generally small (≤0.1% of the systemic dose), but may still be of toxicological importance. To what extent the NPs are distributed to and accumulated/degraded in the organs depends on a number of NP-dependent as well as NP-independent factors. Among NP-dependent factors are (as discussed earlier) size, shape and surface charge. The NP-independent factors include organ volumes and blood flows and number of phagocytizing cells and their capacities in different organs. There are several ongoing efforts to describe these processes by PBPK modeling, see chapter 9.

8 Biokinetic/physiologically-based (PBPK) models

Physiologically-based pharmacokinetic/biokinetic (PBPK) modeling is a useful tool to describe, understand and predict the toxicokinetics (absorption, distribution, metabolism and elimination) of hazardous agents. PBPK models employ anatomical and physiological features, such as the structure of the circulatory system, organ and tissue volumes, tissue partition coefficients, and tissue blood flows, to calculate the mass flow of substance of interest is deposited in a time-dependent manner within organs and tissues PBPK models may be used *eg* to extrapolate from high dose to low dose, from animals to humans and between exposure routes, to predict the target dose for different exposure scenarios, to estimate the toxicokinetic and target dose variability in a population, and to describe the relation between exposure and biomarker level. Another valuable aspect of PBPK models is their ability to generate hypotheses, aid in the design of biodistribution studies, and identify additional research that is needed (see *eg* (Andersen, Clewell *et al* 1987; Johanson 2010; Mörk and Johanson 2010; Verner, McDougall *et al* 2012)).

PBPK approaches to address the biokinetics of NPs are described in the following sections.

8.1 Intravenous PBPK models

Fallon *et al* developed a PBPK model to describe the kinetic effects of treating drug overdoses by NPs. They departed from a previously developed PBPK modle (ref 11) with eight compartment model including blood, liver, gut, heart, brain, kidneys, muscle, and fat and modified the mass balance equations to account for NPs. The clearance of drug by the body was neglected as it was considered insignificant during the short time scales (15–30 min) that are relevant in drug overdose treatment. Different models were tested, assuming that the NPs was restrained to blood or could diffuse through the capillary walls and assuming different time scales for equilibration of drug between blood and NPs. The models did not assume diffusion limited, phagocytic or other saturable processes (Fallon, Varshney *et al* 2004).

Lin *et al* developed a blood flow limited PBPK model for quantum dots (QD705, 18.5 nm, CdSe, Tc core, ZnS shell) based on experimental toxicokinetic data from male ICR mice followed up to 6 months after a single *iv* dose (sacrificed after 1, 4, and 24 h; 3, 7, 14, and 28 d; and 6 months). The model consisted of six compartments: venous blood, arterial blood, spleen liver, kidneys and rest of body. Distribution to the organ compartments was controlled by time-dependent Hill equations with organ-specific

fitted parameters for initial and maximum organ:blood distribution coefficients, slope constants and times at half maximum. Late phase (after 28 d) metabolism was assumed to occur in the liver, this was also described by a Hill equation. The authors reported an excellent agreement between PBPK simulated and experimental data (Lin, Chen *et al* 2008). The good fit is likely a result of over-parameterization (five Hill equations, 20 fitted parameters).

Lee *et al* developed a similar flow-limited six-compartment PBPK model (blood, skin, muscle, kidney, liver, other) but with fixed fitted organ-specific blood:tissue partition coefficients (*ie* no Hill equations). The model was tested against a variety of quantum dots: QD525 (12 nm, *iv* mouse data), QD621 (37 nm nail-shaped, intradermal mouse data), QD705 (13 nm ellipsoid, *iv* mouse data), QD800 (21 nm, *iv* mouse data), QD-LM (coated with mercaptoundecanoic acid cross-linked with lysine, 7-25 nm spherical, *iv* rat data) and QD-BSA (coated with mercaptoundecanoic acid cross-linked BSA, 80 nm spherical, *iv* rat data). The model predicted the experimentally observed persistence of QDs in tissues but not early time profiles and the differences in biodistribution between quantum dots. The authors concluded that more complex models are needed to capture quantum dot biodistribution (Lee, Leavens *et al* 2009).

A PBPK model was developed and compared with experimental data on blood and organ toxicokinetics from rats *iv* dosed once daily for 5 d with silver NPs (20, 80 and 110 nm) and followed up to 16 d. The model consists of five compartments, blood, liver, spleen, kidney and remaining tissues, with NP elimination from the blood compartment. Each compartment, except remaining tissues, is divided in two sub compartments representing freely available and (quasi) irreversibly tissue incorporated NPs. Although not explicitly stated by the authors, this subdivision may be seen to represent phagocytosis, however, dose-dependent kinetics is not covered, as all processes are first-order and described by rate constants. Following both single and repeated injection, the silver NPs disappeared rapidly from the blood and distributed to all organs evaluated (liver, lungs, spleen, brain, heart, kidneys and testes) regardless of size. Although the NPs distributed different (20 nm NPs mainly to liver, followed by kidneys and spleen, 80 and 110 nm NPs mainly to spleen followed by liver and lung), there was no clear relation between fitted model parameter values (tissue partition coefficients, blood flow limiters and tissue incorporation rate constants) and NP diameter (Lankveld, Oomen *et al* 2010).

In order to analyze tumor binding data in mice of molecular imaging NPs, Opitz *et al* used a “classical PBPK” model developed by Peng *et al* (Peng, Andrews *et al* 2001) for the pharmacokinetics in rats of a phosphorothioate oligonucleotide (PS-ODN). The molecular imaging NP (size not stated) consisted of a peptide (to facilitate cellular uptake), a hydrophilic spacer, a complementary peptide nucleic acid (to bind specifically to cancer cell mRNA), a hydrophilic spacer and a metal chelator (*eg* gadolinium is used as magnetic resonance imaging contrast agent). The model was based on flow-limited, permeability restricted and partition coefficient-dependent distribution to organs. It did not include phagocytosis or other dose-dependent processes (Opitz, Wickstrom *et al* 2010).

A PBPK model was utilized to interpret the effects of nanoparticle properties on previously published biodistribution data. Biodistribution data for five PLGA NP formulations prepared with varied content of monomethoxypolyethyleneglycol (mPEG) (PLGA, PLGA-mPEG256, PLGA-mPEG153, PLGA-mPEG51, PLGA-mPEG34, all with negative zeta potential, sizes 58-134 nm) were collected in female Swiss-De mice after *iv* injection of 300 µg per mouse. A PBPK model was used to simulate mass-time profiles of NP distribution in tissues. Multivariate regression analysis was performed to investigate the relationship between NP properties (size, zeta potential, and number of PEG molecules per unit surface area) and biodistribution parameters. Based on these relationships, the PBPK model was used to predict the biodistribution of a sixth NP formulation, PLGA-mPEG495, with new physicochemical properties. The fitted biodistribution profiles of the five initial formulations as well as the predicted profile of the sixth formulation were close to experimental data (Li, Panagi *et al* 2012). The model does not separate blood flow and diffusion, as these processes are embedded in the fitted rate constants for each organ. Further, saturable phagocytosis is not addressed. Thus the applicability outside the domain *eg* other doses, other species, other sizes or positive zeta potential, is limited.

Mager *et al* developed a PBPK model to characterize the biokinetics of five gold-dendrimer composite nanodevices (CNDs) administered *iv* (dose 400 µg) to mice bearing melanoma cell lines. The gold content in plasma and tissue samples was determined by neutron activation analysis. The PBPK model was developed for 5 nm positive, negative, and neutral and for 11 nm negative NPs and extrapolated to 22 nm positive NPs. The model consists of 7 compartments (blood, liver, spleen, kidney, heart, brain, muscle and other) and is permeability limited in all compartments except live, spleen and brain where a direct uptake rate is used to describe accumulation. The negative and neutral NPs exhibited similar biodistribution profiles. The model was optimized by fitting a large number of model parameters de novo for each NP type (Mager, Mody *et al* 2012). All processes in the model are first-order. Phagocytosis in liver and spleen is accounted for as initial fractional uptake constants.

Li *et al* developed a PBPK model that includes phagocytosis of NPs and applied it to predict the biodistribution of *iv* injected polyethylene glycol-coated polyacrylamide NPs in rats. The model consist of ten compartments: venous and arterial blood, lungs, rest of body, bone marrow, brain, heart, kidneys, liver and spleen. All compartments have a sub compartment corresponding to phagocytic cells, and all organ compartments have a sub compartment reflecting the interstitium. The transfer of NPs from blood to organs is limited by both blood flow and diffusion, the distribution is in addition governed by a blood:interstitium partition coefficient. The uptake by phagocytic cells is controlled by two parameters reflecting maximum capacity and affinity. All phagocytic cells are assumed to behave the same way, only the number of cells and, hence, the overall capacity differs between organs. The model could explain 97% of the observed variation in experimentally determined NP amounts across organs. According to this model, phagocytic cells quickly captured nanoparticles until saturated. Thus, phagocytizing cells constituted the major reservoir in richly perfused organs and stored 83% of the NPs found in spleen, liver, bone marrow, lungs, heart and kidney at 120 h post-dosing. The key determinants of NP biodistribution were the uptake capacity of

phagocytizing cells in the organs, the partitioning between tissue and blood, and the permeability across the capillary endothelium (Li, Johanson *et al* 2014).

The Li *et al* model was further developed by Carlander *et al* in order to be able to apply it on widely different types of NPs given *iv* to rats. The same model and the same physiological parameters, including number of phagocytic cells, were applied to four different NPs: PEGylated and uncoated polyacrylamide (31 nm, spherical), gold (13x56 nm, rod shaped), and titanium dioxide (63 nm, spherical) NPs, whereas NP-specific parameters (blood:interstitium partition coefficient and maximum capacity and affinity of phagocytic cells) were chosen on the basis of the best fit to the experimental time-courses of NP accumulation in various tissues. The model describes the behavior of all four types of NPs adequately, despite widely different biokinetic behavior and physicochemical properties. In addition, the simulations demonstrated that the dose has a profound impact on the biokinetics; this was attributed to saturation of the phagocytic cells at higher doses. The fitted model parameters that were most dependent on NP type were the blood:tissue permeability coefficients and the rate constant for phagocytic uptake. Since only four types of NPs with several differences in characteristics (dose, size, shape and surface charge and properties) were used, the relationship between these characteristics and the NP-dependent model parameters could not be elucidated. The authors concluded that more experimental biodistribution studies are required to understand these relations (Carlander, Li *et al*).

A membrane-limited physiologically based pharmacokinetic (PBPK) model for PEGylated gold NPs was developed for mice. The model includes two important features, namely diffusion-limited transport across the capillary walls and time-dependent endocytosis of NPs in the liver, spleen, kidneys, and lungs, described by a Hill function. The model was calibrated against experimental data from mice *iv* injected with 0.85 mg/kg bw of 13-nm and 100-nm NPs. The model adequately predicted multiple external datasets for other PEGylated gold NPs of similar sizes (13-20 nm; 80-100 nm). The calibration suggested that the endocytosis of NPs is both time and size dependent, *ie* endocytosis of larger NPs occurs immediately and predominately from the blood, whereas smaller NPs diffuses through the capillary wall and their endocytosis appears mainly from the tissue with a time delay. The sensitivity analysis showed that several physiological parameters have a high influence on the model output, indicating the need to include additional species for comparison and species scaling and the need to conduct pharmacokinetic studies in species more closely related to humans (Lin, Monteiro-Riviere *et al* 2016).

Departing from the mouse PBPK model describe above, Lin and colleagues adapted the mouse PBPK model for PEGylated gold NPs to other species, namely rats and pigs, by using species-specific physiological and endocytosis parameters. The model was calibrated and evaluated with multiple independent datasets obtained with rats and pigs. The model was further scaled to humans by using human physiology parameters but keeping animal endocytosis parameters. The model output for humans was then compared with pharmacokinetic data (time courses in blood) for 27-nm gold NPs coated with PEG and recombinant human tumor necrosis factor alpha obtained in a phase I dose escalation clinical trial with advanced-stage cancer patients (Libutti, Paciotti *et al* 2010). Lin *et al* concluded that rats and pigs seem more appropriate models than mice in

animal-to-human extrapolation and that dose and age should be addressed (Lin, Monteiro-Riviere *et al* 2016).

Chen *et al* developed a PBPK model to describe the biokinetics of zinc oxide NPs in mice. The physicochemical parameters of partition coefficients and excretion/ elimination rates were estimated from previously published experimental data on the biodistribution of 10 and 71 nm NPs and of zinc nitrate in various mice tissues. Time-dependent partition coefficients and excretion/elimination rates were introduced in the model using Hill-type equations. In general, the tissue partition coefficients of zinc oxide NPs were greater than those of zinc nitrate, particularly the lung partition coefficient of 10 nm NPs. Although the partition coefficient of the brain was relative low, it increased time-dependently for (both the zinc oxide NPs and for zinc nitrate. Replacing the partition coefficients of zinc oxide NPs with those of zinc nitrate after day 7 greatly improved the goodness of fit, suggesting that the NPs decompose to zinc ions after day 7 (Chen, Cheng *et al* 2015). The model does not include diffusion limited processes or phagocytosis. The use of Hill equations and fitting of many model parameters makes the predictive capability of the model low.

A PBPK model for mice was developed to describe the biodistribution kinetics following a single *iv* dose of fluorescently labeled block polymer NPs (110 nm, assembled from amphiphilic block copolymers polyethylene glycol and poly ε-caprolactone bearing pendant cyclic ketals) used for controlled delivery of dexamethasone in acute lymphoblastic leukemia therapy. The model has four compartments (plasma, liver, spleen and kidneys) with NP excretion from kidneys). The model treats redistribution as first order organ-specific rate constants. The simulated NP concentration time courses in liver, spleen, and kidney agreed well with published experimental in vivo data. However, the initial peak seen in plasma was not captured by the PBPK model which predicted a rapid initial decline. The simulation predicted an unaccounted accumulation of about 50% of the injected dose, the lead to incorporation of a fifth, “other” compartment (Gilkey, Krishnan *et al* 2015). The model does not include permeability limited processes and phagocytosis.

8.2 Inhalation PBPK models

8.2.1 Lung deposition models

A physiology-oriented multicompartmental model was developed to describe the alveolar clearance and retention of biologically insoluble, respirable, low-toxicity particles in rats. Assuming a deposit-activated maximum macrophage recruitment rate on the alveolar epithelial surface, the model uses a theoretical derivation of an exposure-dependent distribution of particles in the alveolar macrophage population to determine the total load in mobile and immobilized macrophages. The authors used independently determined data on clearance rate coefficients, alveolar macrophage lifetime and particle turnover by phagocytosis. The model successfully simulated experimental data on alveolar and lymph node burden from fifteen subchronic or chronic experiments with Fischer 344 rats exposed to diesel soot, carbon black or xerographic toner. Experimental data were successfully simulated for sub micrometer-sized aerosols like carbon black (0.24 µm), diesel soot (0.23-0.26 µm) and titanium dioxide and for a micrometer-sized

xerographic toner aerosol (4 µm) (Stober, Morrow *et al* 1994). The model was later on expanded to more cytotoxic silica aerosols (rutile 1.1 µm, anatase 0.25 µm). As the alveolar macrophages were burdened with cytotoxic particles, the cells suffered a substantial initial decrease in mobility resulting in reduced alveolar clearance rate coefficient compared to the nontoxic aerosols (Stober 1999).

The MPPD model calculates the deposition and clearance of monodisperse and polydisperse aerosols in the respiratory tract of rat and humans for particles ranging from ultrafine (10 nm) to coarse (20 µm) sizes. The models are based on single- and multiple-path methods to track air flow and calculate aerosol deposition in the lungs. The single-path method calculates deposition in a typical path per airway generation, while the multiple-path method uses lobar- and airway-specific information. Within each airway generation, deposition is calculated from theoretically derived efficiencies for deposition by diffusion, sedimentation and impaction. Filtration of aerosols in the nose and mouth is also included by use of empirical efficiency functions (Anjilvel and Asgharian 1995; Price, Asgharian *et al* 2002). The latest version (v2.11) of MPPD allows internal exposure estimation of spherical NPs.

One example of use of the MPPD model is that of Geraets and coworkers who studied the lung deposition and biodistribution in rats of inhaled cerium oxide particles of various sizes (5-5000 nm) and at various doses (see chapter Inhalation for details). Due to aggregation, the particles ended up with similar aerodynamic diameters (1-1.4 µm) and the lung deposition was similar, 10%, as was also predicted by the MPPD model (Geraets, Oomen *et al* 2012).

Tran *et al* developed a model to describe the retention and clearance of insoluble inhaled particles in the rat lung. The model includes alveolar and lung interstitial phagocytosis of free particles, transport, sequestration, clearance to the interstitium and thoracic lymph nodes, release of phagocytized particles, and influence of particle burden on macrophage activity. The model was tuned against experimental data from a series of inhalation experiments with titanium dioxide, with exposure concentrations between 1 and 90 µg/m^3 and durations up to 2 years. During inhalation, clearance rates are affected by translocation of dust and by overloading. The particle, *ie* delayed clearance at higher doses, was well captured by the model (Tran, Jones *et al* 1999; 1999).

Kuempel *et al* developed similar but less complex particle inhalation models (one and three compartments (the latter including transport to interstitium and lymph nodes), first-order and dose-dependent alveolar clearance rate coefficients (the latter to account for particle overload) and fitted them to data of 131 U.S. coal miners. The data included workplace exposures and end-of-life particle burdens in the lungs and hilar (bronchopulmonary) lymph nodes. Uncertainty in model structure was assessed by fitting the different various models for particle clearance and sequestration and sensitivity analyzes were performed to determine which model parameters were most influential. The three-compartment model with first-order alveolar clearance (no influence of overload) provided the best fit to the coal miner data. Race and pulmonary fibrosis severity but not smoking history was statistically significant predictors of the alveolar clearance rate (Kuempel, Tran *et al* 2001).

Shelley *et al* modeled, based on experimental data, the population dynamics of rat alveolar macrophages in vitro when exposed to toxic levels of 80-nm aluminum. The model includes macrophage behavior and function (growth by cell division, phagocytosis, migration, cell death) due to NP exposures, as well as the change in free NP number over time (Shelley, Wagner *et al* 2008).

Kleinstreuer *et al* reviewed the state of knowledge regarding computer modeling of the airflows and related deposition of nano- and microsized particles in the airways. As the deposition of NPs is dominated by diffusion they deposit on the airway surfaces rather uniformly, whereas microsized particles, due to impaction and secondary flows, tend to accumulate around the carinal ridges and to form "hot spots", *ie* local high concentrations which may increase the risk of tumor development. Inhaled particles in the size range 20 nm - 3 µm may readily reach the deeper lung region. NPs below 20 nm and above 3 µm in size tend to deposit in the upper airways due to diffusion and impaction, respectively (Kleinstreuer, Zhang *et al* 2008).

Although the above models are limited to particle behavior in the lungs and were primarily developed for larger particles, they represent useful approaches that may be incorporated in whole-body PBPK models, *eg* to capture the role of particle dissolution and the link between toxicokinetics and toxicodynamics.

8.2.2 Whole-body inhalation models

MacCalman *et al* developed a "classical" rodent PBPK model, with the major organs: GI tract, liver, kidney, heart, spleen, brain and others, interconnected via the blood circulation To account for inhalation exposure, six additional compartments were added: olfactory region, upper airways, free space in alveolar region, alveolar macrophages, interstitium and lung lymph nodes. Data from two experimental rat studies, one with endotracheal instillation of iridium NPs (15-20) with 6 months follow-up, and one with inhalation exposure to silver NPs (17 nm) for 6 h and with 7 d follow-up, were used to calibrate the model by least-square fitting of the model parameters. Most of the nanoparticle mass remained in the lungs. The model described the retention and translocation of nanoparticles from the lungs reasonably well and the fit to measured particle mass by organ was good for lungs, brain, and spleen but less good for liver and kidney (MacCalman, Tran *et al* 2009). The model does not incorporate dissolution or phagocytosis.

The above PBPK model (MacCalman, Tran *et al* 2009) was modified and recalibrated by Bayesian population analysis using Markov chain Monte Carlo (MCMC) simulation. The model includes organ specific partition coefficients and NP clearance and phagocytosis rates in the alveolar region only. Experimental data from a studies with male Wistar exposed to iridium (15-20 nm, 60-100 min, single inhalation exposure) and titanium dioxide (20-30 nm, single *iv* injection) NPs were used for model calibration. When data from a second study iridium (15 nm, 60 min, single inhalation exposure) were added, the level of agreement was still acceptable. However, addition of a data set with silver NPs (20 nm, five daily *iv* injections) led to substantially lower precision in parameter estimates and large discrepancies between model predictions and experimental data for the silver NPs (Sweeney, MacCalman *et al* 2015).

Pery *et al* developed a PBPK model for 60-nm ^{99m}Tc -labeled carbon NPs (Technegas). The model includes different translocation rates and kinetics from lung to blood and urine and for clearance to urine for free technetium, and small and large ^{99m}Tc -labeled particles. The model was calibrated against imaging data from an experiment designed to assess the fate of NPs in humans after inhalation of Technegas. The experimental data consisted of time courses of radioactivity in the liver, stomach, urine, and blood. Organ distribution was accounted for by organ-specific fractions and blood-organ partition coefficients (same for all organs) for NPs and free technetium. Parameter estimation (lung translocation rates, organ fractions, partition coefficients) was performed by MCMC simulation. The percentage of small particles able to translocate after inhalation was estimated at 12.7% of total inhaled. The percentage of unbound technetium was estimated at 6.7% of total technetium (Pery, Brochot *et al* 2009). The model does neither include diffusion-limited transport, nor phagocytosis.

Kolanjiyil and Kleinstreuer developed a hybrid model for the mass transfer of inhaled NPs and their further lung clearance, uptake and systemic distribution. The fluid-particle dynamics of a dilute NP suspension was simulated for the entire respiratory tract, assuming steady inhalation and planar airways. An anatomically realistic airway configuration was considered from nose/mouth down to generation 3, for deeper lung regions repeat identical triple-bifurcations unit were assumed. The deposition of NPs in the extrathoracic, tracheobronchial, bronchiolar, and alveolar tracts was calculated. These region-specific depositions were used to estimate model parameters by best fit against experimental retention and clearance data in human lungs. The deposition model was the combined with an uptake model to describe NP from the airway linings in the different regions via the epithelium/interstitium (from the olfactory region via the olfactory bulb and brain, from tracheobronchial and bronchiolar regions also to lymph) to circulating blood. The systemic distribution following uptake in blood was modelled by a linked whole-body PBPK model (no details given except organ blood flows) (Kolanjiyil and Kleinstreuer 2013; 2013).

Bachler *et al* developed a biokinetic model for short term inhalation exposure to gold NPs in two steps. In the first step, alveolar epithelial cellular monolayers in an ALI system were exposed to aerosolized gold NPs to determine the translocation kinetics across the cell layer. In the second step, the biodistribution to various organs was predicted with a PBPK model previously developed for titanium dioxide NPs (Bachler, von Goetz *et al* 2015). Monodisperse, spherical, negatively charged gold NPs were used at various doses (25-200 ng/cm^2) and sizes (2-80 nm), and the cells were incubated post-exposure for different time periods up to 72 h. The translocation kinetics of NPs across human (A549 and mouse (MLE-12) epithelial cells was similar. Further, the translocated fraction was inversely proportional to NP size and independent of the applied dose up to 100 ng/cm^2. Supplementing the ALI system with immune cells (macrophages and dendritic cells) did not significantly affect the NP translocation. The translocation kinetic data from the cell cultures were used in combination with the previously developed PBPK model to predict the biodistribution of inhaled and instilled gold NPs in vivo. The predicted organ levels (relative to dose) compared well with experimental data obtained from female Wistar-Kyoto rats after it instillation and from

mice after 2h inhalation (Bachler, Losert *et al* 2015). The applicability of the model for predictions exceeding 24 h is limited as clearance from lung is not included.

8.2.3 Multiroute PBPK models

Li and Reineke published a general PBPK model to describe the absorption, distribution, metabolism, and elimination (ADME) of NPs humans after *iv*, oral, and inhalation exposure. The model uses mass transfer coefficients to account for NP transfer to well-mixed compartments representing different organs in the body, *ie* all mass transfer processes are first order (Li and Reineke 2011). The authors claim that their model, although not based on data from any specific NP formulation, explains very well the results from many NP biodistribution studies and that, therefore, parameters used in the model were properly estimated. However, it is not clear how the parameters were estimated and only qualitative comparisons are presented to support the authors' conclusions. Further, the model does not account for, for example, diffusion-limited processes, phagocytosis or size-dependent lung deposition. Overall, this model is not useful to understand or predict the biokinetics of NPs.

Based on toxicokinetic data from *iv* studies, Bachler and coworkers (Bachler, von Goetz *et al* 2013) developed a PBPK model for ionic and nanosized silver biokinetics in rats and humans. The model consists of eleven compartments (brain, spleen, bone marrow, testes, muscles, heart, lungs, liver, skin, kidneys, intestines) and accounts for four entry routes (*iv*, inhalation, dermal, oral) and three excretion routes (biliary, urinary, direct from intestines). Silver dissolution is assumed to occur in the liver. It is further assumed that all processes are first-order (*ie* no dose-dependence, no saturation) and size-independent (except for phagocytosis). The model was validated for both silver forms by comparing simulated and experimentally obtained organ concentrations following dermal, oral, and inhalation exposure studies in vivo. The ICRP model was used for NP inhalation exposure, this model includes size-dependent deposition in five lung compartments and movement/clearance between these compartments and the GI tract. The organ uptake of ionic silver was defined as being proportional to the organ glutathione concentration, in view of the strong silver-glutathione complex formation. The model was optimized against a variety of rat and human experimental data, namely

- daily oral dosing for 28 d with silver acetate and with 14 and 60nm silver NPs,
- single and 28 d 6-h inhalation exposure to 14 nm silver NPs,
- single intratracheal instillation of silver nitrate,
- organ silver reference values of the US population,
- organ silver levels of deceased burn victims treated with silver nitrate,
- and biomonitoring data from workers exposed to silver in air.

The model could successfully predict the biodistribution of ionic silver and 15-150 nm uncoated silver NPs. The simulations indicate that the particle size and coating had a minor influence on the biodistribution, that in vivo it is more likely that silver NPs are directly stored as insoluble salt particles than dissolve into ions, and that phagocytic compartments play a minor role at exposure levels relevant for human consumers

(Bachler, von Goetz *et al* 2013). However, the mass balances equations reported are incomplete and consequently the usability of the model limited.

A PBPK model was developed to describe the biodistribution of titanium dioxide NPs, based on the NPs' ability to cross the capillary wall of the organs and become phagocytized by the mononuclear phagocyte system in liver, spleen and lung. The model allows for three exposure routes; *iv*, oral and dermal, and three excretion routes, direct (via feces), biliary and urinary and assumes that all processes are first-order (*ie* no dose-dependence, no saturation). A deviation to other models is that clearance to bile occurs from all organs. The predictive power was evaluated by comparing simulated NP amounts in different organs with experimentally determined amounts in vivo. The simulated amounts of NPs in different organs agreed well with experimental data measure 1, 3, 7, 15 and 30 d after *iv* injection of 10 mg/kg bw of 20-nm rutile titanium dioxide NPs. The PBPK modeling indicated that the size (15-150 nm) and crystalline structure of the particles had a minor influence on the biodistribution, and that at high internal doses the particles agglomerate in vivo and are subsequently taken up by macrophages (Bachler, von Goetz *et al* 2015Bachler, von Goetz *et al* 2015).

8.3 Conclusions – PBPK modeling

A number of different PBPK models have been developed for different purposes, with different NP types and with different exposure routes (*iv*, inhalation, oral, dermal). Twenty-five of these models, deemed most relevant, are summarized in this chapter. Models have mainly been developed for rats and mice (with most experimental data) and for humans (the species of interest, but little data) and most are very similar to the classical form of PBPK models, in the sense that the mass flow of NPs is calculated over time for different organ compartments linked via the blood flow. However, many models neglect the roles of diffusion/endocytosis-limited transport across membranes and the role of capacity-limited phagocytosis. Further, model tuning (parameter fitting) against experimental data has been performed in numerous ways, mostly with many parameters fitted against limited experimental data sets. This is not surprising, as key physiological data, particularly for phagocytic process (such as number of phagocytizing cells and their capacities in different organs and in different species) are lacking. Moreover, experimental biodistribution and biokinetic studies frequently lack key information or are incomplete regarding one or several of the following aspects:

- NP characterization, including size and size distribution, specific surface area, agglomeration, zeta potential, reactivity, stability/dissolution, methods for characterization),
- dose characterization (mass, particle count, surface area),
- time course of NP mass or concentration in tissues, including short follow-up post-dosing, infrequent sampling, few tissues studied, and few samples per tissue,
- account for NP recovery in tissues (organ weights, detection limits, stability/dissolution, total recovery), and
- lack of confirmation on NP integrity in tissue.

So far, due to the variety of PBPK approaches, the lack of basic physiologic knowledge, especially with respect to phagocytosis, and the limitations of published experimental biodistribution and biokinetic data, biokinetic/PBPK modeling of NPs is still in its infancy.

9 References

Aalapati S, Ganapathy S, Manapuram S, Anumolu G, Prakya BM (2014). *Toxicity and bio-accumulation of inhaled cerium oxide nanoparticles in CD1 mice*. **Nanotoxicology** 8(7): 786-798.

Adachi K, Yamada N, Yoshida Y, Yamamoto O (2013). *Subchronic exposure of titanium dioxide nanoparticles to hairless rat skin*. **Exp Dermatol** 22(4): 278-283.

Adamcakova-Dodd A, Stebounova LV, Kim JS, Vorrink SU, Ault AP, O'Shaughnessy PT, Grassian VH, Thorne PS (2014). *Toxicity assessment of zinc oxide nanoparticles using sub-acute and sub-chronic murine inhalation models*. **Part Fibre Toxicol** 11: 15.

Alvarez-Roman R, Naik A, Kalia YN, Guy RH, Fessi H (2004). *Skin penetration and distribution of polymeric nanoparticles*. **J Control Release** 99(1): 53-62.

Andersen ME, Clewell HJ, Gargas ML, Smith FA, Reitz RH (1987). *Physiologically based pharmacokinetics and the risk assessment process for methylene chloride*. **Toxicol Appl Pharmacol** 87(2): 185-205.

Anjilvel S, Asgharian B (1995). *A multiple-path model of particle deposition in the rat lung*. **Fundam Appl Toxicol** 28(1): 41-50.

Bachler G, Losert S, Umehara Y, von Goetz N, Rodriguez-Lorenzo L, Petri-Fink A, Rothen-Rutishauser B, Hungerbuehler K (2015). *Translocation of gold nanoparticles across the lung epithelial tissue barrier: Combining in vitro and in silico methods to substitute in vivo experiments*. **Part Fibre Toxicol** 12: 18.

Bachler G, von Goetz N, Hungerbuhler K (2013). *A physiologically based pharmacokinetic model for ionic silver and silver nanoparticles*. **Int J Nanomed** 8: 3365-3382.

Bachler G, von Goetz N, Hungerbuhler K (2015). *Using physiologically based pharmacokinetic (PBPK) modeling for dietary risk assessment of titanium dioxide (TiO2) nanoparticles*. **Nanotoxicology** 9(3): 373-380.

Baek M, Chung HE, Yu J, Lee JA, Kim TH, Oh JM, Lee WJ, Paek SM, Lee JK, Jeong J, Choy JH, Choi SJ (2012). *Pharmacokinetics, tissue distribution, and excretion of zinc oxide nanoparticles*. **Int J Nanomed** 7: 3081-3097.

Bai R, Zhang L, Liu Y, Li B, Wang L, Wang P, Autrup H, Beer C, Chen C (2014). *Integrated analytical techniques with high sensitivity for studying brain translocation and potential impairment induced by intranasally instilled copper nanoparticles*. **Toxicol Lett** 226(1): 70-80.

Balasubramanian SK, Poh KW, Ong CN, Kreyling WG, Ong WY, Yu LE (2013). *The effect of primary particle size on biodistribution of inhaled gold nano-agglomerates*. **Biomaterials** 34(22): 5439-5452.

Balogh L, Nigavekar SS, Nair BM, Lesniak W, Zhang C, Sung LY, Kariapper MS, El-Jawahri A, Llanes M, Bolton B, Mamou F, Tan W, Hutson A, Minc L, Khan MK (2007). *Significant effect of size on the in vivo biodistribution of gold composite nanodevices in mouse tumor models*. **Nanomedicine** 3(4): 281-296.

Bargheer D, Giemsa A, Freund B, Heine M, Waurisch C, Stachowski GM, Hickey SG, Eychmuller A, Heeren J, Nielsen P (2015). *The distribution and degradation of radiolabeled superparamagnetic iron oxide nanoparticles and quantum dots in mice*. **Beilstein J Nanotechnol** 6: 111-123.

Baroli B, Ennas MG, Loffredo F, Isola M, Pinna R, Lopez-Quintela MA (2007). *Penetration of metallic nanoparticles in human full-thickness skin*. **J Invest Dermatol** 127(7): 1701-1712.

Bartczak D, Nitti S, Millar TM, Kanaras AG (2012). *Exocytosis of peptide functionalized gold nanoparticles in endothelial cells*. **Nanoscale** 4(15): 4470-4472.

Bednarski M, Dudek M, Knutelska J, Nowinski L, Sapa J, Zygmunt M, Nowak G, Luty-Blocho M, Wojnicki M, Fitzner K, Tesiorowski M (2015). *The influence of the route of administration of gold nanoparticles on their tissue distribution and basic biochemical parameters: In vivo studies*. **Pharmacol Rep** 67(3): 405-409.

Bennat C, Muller-Goymann CC (2000). *Skin penetration and stabilization of formulations containing microfine titanium dioxide as physical UV filter*. **Int J Cosmet Sci** 22(4): 271-283.

Bianco C, Adami G, Crosera M, Larese F, Casarin S, Castagnoli C, Stella M, Maina G (2014). *Silver percutaneous absorption after exposure to silver nanoparticles: a comparison study of three human skin graft samples used for clinical applications*. **Burns** 40(7): 1390-1396.

Bimbo LM, Sarparanta M, Santos HA, Airaksinen AJ, Makila E, Laaksonen T, Peltonen L, Lehto VP, Hirvonen J, Salonen J (2010). *Biocompatibility of thermally hydrocarbonized porous silicon nanoparticles and their biodistribution in rats*. **ACS Nano** 4(6): 3023-3032.

Bouwmeester H, Poortman J, Peters RJ, Wijma E, Kramer E, Makama S, Puspitaninganindita K, Marvin HJ, Peijnenburg AA, Hendriksen PJ (2011). *Characterization of translocation of silver nanoparticles and effects on whole-genome gene expression using an in vitro intestinal epithelium coculture model*. **ACS Nano** 5(5): 4091-4103.

Braakhuis HM, Gosens I, Krystek P, Boere J, Cassee FR, Fokkens P, Post J, van Loveren H, Park M (2014). *Particle size dependent deposition and pulmonary inflammation after short-term inhalation of silver nanoparticles*. **Part Fibre Toxicol** 11(1): 49.

Brooking J, Davis SS, Illum L (2001). *Transport of nanoparticles across the rat nasal mucosa*. **J Drug Target** 9(4): 267-279.

Brown JS, Zeman KL, Bennett WD (2002). *Ultrafine particle deposition and clearance in the healthy and obstructed lung*. **Am J Respir Crit Care Med** 166(9): 1240-1247.

Calatayud MP, Sanz B, Raffa V, Riggio C, Ibarra MR, Goya GF (2014). *The effect of surface charge of functionalized Fe3O4 nanoparticles on protein adsorption and cell uptake*. **Biomaterials** 35(24): 6389-6399.

Calvo P, Gouritin B, Chacun H, Desmaele D, D'Angelo J, Noel JP, Georgin D, Fattal E, Andreux JP, Couvreur P (2001). *Long-circulating PEGylated polycyanoacrylate nanoparticles as new drug carrier for brain delivery*. **Pharm Res** 18(8): 1157-1166.

Calvo P, Gouritin B, Villarroya H, Eclancher F, Giannavola C, Klein C, Andreux JP, Couvreur P (2002). *Quantification and localization of PEGylated polycyanoacrylate nanoparticles in brain and spinal cord during experimental allergic encephalomyelitis in the rat*. **Eur J Neurosci** 15(8): 1317-1326.

Campbell CS, Contreras-Rojas LR, Delgado-Charro MB, Guy RH (2012). *Objective assessment of nanoparticle disposition in mammalian skin after topical exposure*. **J Control Release** 162(1): 201-207.

Carlander U, Li D, Jolliet O, Emond C, Johanson G (2016). *Toward a general physiologically-based pharmacokinetic model for intravenously injected nanoparticles*. **Int J Nanomed** 11: 625-640.

Cassee FR, Muijser H, Duistermaat E, Freijer JJ, Geerse KB, Marijnissen JC, Arts JH (2002). *Particle size-dependent total mass deposition in lungs determines inhalation toxicity of cadmium chloride aerosols in rats. Application of a multiple path dosimetry model*. **Arch Toxicol** 76(5-6): 277-286.

Cedervall T, Lynch I, Lindman S, Berggard T, Thulin E, Nilsson H, Dawson KA, Linse S (2007). *Understanding the nanoparticle-protein corona using methods to quantify exchange rates and affinities of proteins for nanoparticles*. **P Natl Acad Sci USA** 104(7): 2050-2055.

Chau E, Galloway JF, Nelson A, Breysse PN, Wirtz D, Searson PC, Sidhaye VK (2013). *Effect of modifying quantum dot surface charge on airway epithelial cell uptake in vitro*. **Nanotoxicology** 7(6): 1143-1151.

Chen J, Dong X, Zhao J, Tang G (2009). *In vivo acute toxicity of titanium dioxide nanoparticles to mice after intraperitioneal injection*. **J Appl Toxicol** 29(4): 330-337.

Chen J, Tan M, Nemmar A, Song W, Dong M, Zhang G, Li Y (2006). *Quantification of extrapulmonary translocation of intratracheal-instilled particles in vivo in rats: effect of lipopolysaccharide*. **Toxicology** 222(3): 195-201.

Chen JK, Shih MH, Peir JJ, Liu CH, Chou FI, Lai WH, Chang LW, Lin P, Wang MY, Yang MH, Yang CS (2010). *The use of radioactive zinc oxide nanoparticles in determination of their tissue concentrations following intravenous administration in mice*. **Analyst** 135(7): 1742-1746.

Chen WY, Cheng YH, Hsieh NH, Wu BC, Chou WC, Ho CC, Chen JK, Liao CM, Lin P (2015). *Physiologically based pharmacokinetic modeling of zinc oxide nanoparticles and zinc nitrate in mice*. **Int J Nanomed** 10: 6277-6292.

Chen Z, Chen H, Meng H, Xing GM, Gao XY, Sun BY, Shi XL, Yuan H, Zhang CC, Liu R, Zhao F, Zhao YL, Fang XH (2008). *Bio-distribution and metabolic paths of silica coated CdSeS quantum dots*. **Toxicol Appl Pharmacol** 230(3): 364-371.

Cheng QY, Feng J, Chen JM, Zhu X, Li FZ (2008). *Brain Transport of Neurotoxin-I with PLA Nanoparticles through Intranasal Administration in Rats: A Microdialysis Study*. **Biopharm Drug Dispos** 29(8): 431-439.

Chithrani BD, Chan WC (2007). *Elucidating the mechanism of cellular uptake and removal of protein-coated gold nanoparticles of different sizes and shapes*. **Nano Lett** 7(6): 1542-1550.

Chithrani BD, Ghazani AA, Chan WC (2006). *Determining the size and shape dependence of gold nanoparticle uptake into mammalian cells*. **Nano Lett** 6(4): 662-668.

Cho WS, Kang BC, Lee JK, Jeong J, Che JH, Seok SH (2013). *Comparative absorption, distribution, and excretion of titanium dioxide and zinc oxide nanoparticles after repeated oral administration*. **Part Fibre Toxicol** 10: 9.

Choi HS, Liu W, Misra P, Tanaka E, Zimmer JP, Itty Ipe B, Bawendi MG, Frangioni JV (2007). *Renal clearance of quantum dots*. **Nat Biotechnol** 25(10): 1165-1170.

Choi J, Kim H, Kim P, Jo E, Kim HM, Lee MY, Jin SM, Park K (2015). *Toxicity of zinc oxide nanoparticles in rats treated by two different routes: single intravenous injection and single oral administration*. **J Toxicol Environ Health A** 78(4): 226-243.

Crater JS, Carrier RL (2010). *Barrier properties of gastrointestinal mucus to nanoparticle transport*. **Macromol Biosci** 10(12): 1473-1483.

Cross SE, Innes B, Roberts MS, Tsuzuki T, Robertson TA, McCormick P (2007). *Human skin penetration of sunscreen nanoparticles: in-vitro assessment of a novel micronized zinc oxide formulation*. **Skin Pharmacol Physiol** 20(3): 148-154.

Damalakiene L, Karabanovas V, Bagdonas S, Valius M, Rotomskis R (2013). *Intracellular distribution of nontargeted quantum dots after natural uptake and microinjection*. **Int J Nanomed** 8: 555-568.

Darabi Sahneh F, Scoglio C, Riviere J (2013). *Dynamics of nanoparticle-protein corona complex formation: analytical results from population balance equations*. **PLoS One** 8(5): e64690.

des Rieux A, Fievez V, Garinot M, Schneider YJ, Preat V (2006). *Nanoparticles as potential oral delivery systems of proteins and vaccines: a mechanistic approach*. **J Control Release** 116(1): 1-27.

Detoni CB, Coradini K, Back P, Oliveira CM, Andrade DF, Beck RC, Pohlmann AR, Guterres SS (2014). *Penetration, photo-reactivity and photoprotective properties of nanosized ZnO*. **Photochem Photobiol Sci** 13(9): 1253-1260.

Dombu CY, Kroubi M, Zibouche R, Matran R, Betbeder D (2010). *Characterization of endocytosis and exocytosis of cationic nanoparticles in airway epithelium cells.* **Nanotechnology** 21(35): 355102.

dos Santos T, Varela J, Lynch I, Salvati A, Dawson KA (2011). *Quantitative assessment of the comparative nanoparticle-uptake efficiency of a range of cell lines*. **Small** 7(23): 3341-3349.

Durand L, Habran N, Henschel V, Amighi K (2009). *In vitro evaluation of the cutaneous penetration of sprayable sunscreen emulsions with high concentrations of UV filters*. **Int J Cosmet Sci** 31(4): 279-292.

Dziendzikowska K, Gromadzka-Ostrowska J, Lankoff A, Oczkowski M, Krawczynska A, Chwastowska J, Sadowska-Bratek M, Chajduk E, Wojewodzka M, Dusinska M, Kruszewski M (2012). *Time-dependent biodistribution and excretion of silver nanoparticles in male Wistar rats*. **J Appl Toxicol** 32(11): 920-928.

Elci SG, Jiang Y, Yan B, Kim ST, Saha K, Moyano DF, Yesilbag Tonga G, Jackson LC, Rotello VM, Vachet RW (2016). *Surface Charge Controls the Suborgan Biodistributions of Gold Nanoparticles*. **ACS Nano** 10(5): 5536-5542.

Elci SG, Yan B, Kim ST, Saha K, Jiang Y, Klemmer GA, Moyano DF, Tonga GY, Rotello VM, Vachet RW (2016). *Quantitative imaging of 2 nm monolayer-protected gold nanoparticle distributions in tissues using laser ablation inductively-coupled plasma mass spectrometry (LA-ICP-MS)*. **Analyst** 141(8): 2418-2425.

Elder A, Gelein R, Silva V, Feikert T, Opanashuk L, Carter J, Potter R, Maynard A, Ito Y, Finkelstein J, Oberdörster G (2006). *Translocation of inhaled ultrafine*

manganese oxide particles to the central nervous system. **Environ Health Perspect** 114(8): 1172-1178.

Ellinger-Ziegelbauer H, Pauluhn J (2009). *Pulmonary toxicity of multi-walled carbon nanotubes (Baytubes) relative to alpha-quartz following a single 6h inhalation exposure of rats and a 3 months post-exposure period*. **Toxicology** 266(1-3): 16-29.

Enright HA, Bratt JM, Bluhm AP, Kenyon NJ, Louie AY (2013). *Tracking retention and transport of ultrafine polystyrene in an asthmatic mouse model using positron emission tomography*. **Exp Lung Res** 39(7): 304-313.

Fadeel B, Feliu N, Vogt C, Abdelmonem AM, Parak WJ (2013). *Bridge over troubled waters: understanding the synthetic and biological identities of engineered nanomaterials*. **Wiley Interdiscip Rev Nanomed Nanobiotechnol** 5(2): 111-129.

Fallon MS, Varshney M, Dennis DM, Chauhan A (2004). *A physiologically-based pharmacokinetic model of drug detoxification by nanoparticles*. **J Pharmacokinet Pharmacodyn** 31(5): 381-400.

Farcal LR, Uboldi C, Mehn D, Giudetti G, Nativo P, Ponti J, Gilliland D, Rossi F, Bal-Price A (2013). *Mechanisms of toxicity induced by SiO2 nanoparticles of in vitro human alveolar barrier: effects on cytokine production, oxidative stress induction, surfactant proteins A mRNA expression and nanoparticles uptake*. **Nanotoxicology** 7(6): 1095-1110.

Filipe P, Silva JN, Silva R, Cirne de Castro JL, Marques Gomes M, Alves LC, Santus R, Pinheiro T (2009). *Stratum corneum is an effective barrier to TiO2 and ZnO nanoparticle percutaneous absorption*. **Skin Pharmacol Physiol** 22(5): 266-275.

Filon FL, Crosera M, Adami G, Bovenzi M, Rossi F, Maina G (2011). *Human skin penetration of gold nanoparticles through intact and damaged skin*. **Nanotoxicology** 5(4): 493-501.

Fischer HC, Hauck TS, Gomez-Aristizabal A, Chan WC (2010). *Exploring primary liver macrophages for studying quantum dot interactions with biological systems*. **Adv Mater** 22(23): 2520-2524.

Fleischer CC, Payne CK (2014). *Nanoparticle-cell interactions: molecular structure of the protein corona and cellular outcomes*. **Acc Chem Res** 47(8): 2651-2659.

Florence AT, Hillery AM, Hussain N, Jani PU (1995). *Factors affecting the oral uptake and translocation of polystyrene nanoparticles: histological and analytical evidence*. **J Drug Target** 3(1): 65-70.

Frigell J, Garcia I, Gomez-Vallejo V, Llop J, Penades S (2014). *(68)Ga-Labeled Gold Glyconanoparticles for Exploring Blood-Brain Barrier Permeability: Preparation, Biodistribution Studies, and Improved Brain Uptake via Neuropeptide Conjugation*. **J Am Chem Soc** 136(1): 449-457.

Fu C, Liu T, Li L, Liu H, Chen D, Tang F (2013). *The absorption, distribution, excretion and toxicity of mesoporous silica nanoparticles in mice following different exposure routes*. **Biomaterials** 34(10): 2565-2575.

Furuyama A, Kanno S, Kobayashi T, Hirano S (2009). *Extrapulmonary translocation of intratracheally instilled fine and ultrafine particles via direct and alveolar macrophage-associated routes*. **Arch Toxicol** 83(5): 429-437.

Gamer AO, Leibold E, van Ravenzwaay B (2006). *The in vitro absorption of microfine zinc oxide and titanium dioxide through porcine skin*. **Toxicol in Vitro** 20(3): 301-307.

Geiser M, Rothen-Rutishauser B, Kapp N, Schurch S, Kreyling W, Schulz H, Semmler M, Hof VI, Heyder J, Gehr P (2005). *Ultrafine particles cross cellular membranes by nonphagocytic mechanisms in lungs and in cultured cells*. **Environ Health Perspect** 113(11): 1555-1560.

Geiser M, Stoeger T, Casaulta M, Chen S, Semmler-Behnke M, Bolle I, Takenaka S, Kreyling WG, Schulz H (2014). *Biokinetics of nanoparticles and susceptibility to particulate exposure in a murine model of cystic fibrosis*. **Part Fibre Toxicol** 11: 19.

Gentile F, Ferrari M, Decuzzi P (2008). *The transport of nanoparticles in blood vessels: the effect of vessel permeability and blood rheology*. **Ann Biomed Eng** 36(2): 254-261.

George R, Merten S, Wang TT, Kennedy P, Maitz P (2014). *In vivo analysis of dermal and systemic absorption of silver nanoparticles through healthy human skin*. **Australas J Dermatol** 55(3): 185-190.

Geraets L, Oomen AG, Krystek P, Jacobsen NR, Wallin H, Laurentie M, Verharen HW, Brandon EF, de Jong WH (2014). *Tissue distribution and elimination after oral and intravenous administration of different titanium dioxide nanoparticles in rats*. **Part Fibre Toxicol** 11: 30.

Geraets L, Oomen AG, Schroeter JD, Coleman VA, Cassee FR (2012). *Tissue distribution of inhaled micro- and nano-sized cerium oxide particles in rats: results from a 28-day exposure study*. **Toxicol Sci** 127(2): 463-473.

Gharbi N, Pressac M, Hadchouel M, Szwarc H, Wilson SR, Moussa F (2005). *[60]fullerene is a powerful antioxidant in vivo with no acute or subacute toxicity*. **Nano Lett** 5(12): 2578-2585.

Gilkey MJ, Krishnan V, Scheetz L, Jia X, Rajasekaran AK, Dhurjati PS (2015). *Physiologically Based Pharmacokinetic Modeling of Fluorescently Labeled Block Copolymer Nanoparticles for Controlled Drug Delivery in Leukemia Therapy*. **CPT Pharmacometrics Syst Pharmacol** 4(3): e00013.

Gopee NV, Roberts DW, Webb P, Cozart CR, Siitonen PH, Latendresse JR, Warbitton AR, Yu WW, Colvin VL, Walker NJ, Howard PC (2009). *Quantitative determination of skin penetration of PEG-coated CdSe quantum dots in dermabraded but not intact SKH-1 hairless mouse skin*. **Toxicol Sci** 111(1): 37-48.

Gopee NV, Roberts DW, Webb P, Cozart CR, Siitonen PH, Warbritton AR, Yu WW, Colvin VL, Walker NJ, Howard PC (2007). *Migration of intradermally injected quantum dots to sentinel organs in mice*. **Toxicol Sci** 98(1): 249-257.

Graf C, Meinke M, Gao Q, Hadam S, Raabe J, Sterry W, Blume-Peytavi U, Lademann J, Ruhl E, Vogt A (2009). *Qualitative detection of single submicron and nanoparticles in human skin by scanning transmission x-ray microscopy*. **J Biomed Opt** 14(2): 021015.

Gratieri T, Schaefer UF, Jing L, Gao M, Kostka KH, Lopez RF, Schneider M (2010). *Penetration of quantum dot particles through human skin*. **J Biomed Nanotechnol** 6(5): 586-595.

Gratton SE, Ropp PA, Pohlhaus PD, Luft JC, Madden VJ, Napier ME, DeSimone JM (2008). *The effect of particle design on cellular internalization pathways*. **Proc Natl Acad Sci USA** 105(33): 11613-11618.

Guarnieri D, Guaccio A, Fusco S, Netti PA (2011). *Effect of serum proteins on polystyrene nanoparticle uptake and intracellular trafficking in endothelial cells*. **J Nanopart Res** 13(9): 4295-4309.

Guerrero S, Araya E, Fiedler JL, Arias JI, Adura C, Albericio F, Giralt E, Arias JL, Fernandez MS, Kogan MJ (2010). *Improving the brain delivery of gold nanoparticles by conjugation with an amphipathic peptide*. **Nanomedicine (London UK)** 5(6): 897-913.

Gulson B, McCall M, Korsch M, Gomez L, Casey P, Oytam Y, Taylor A, McCulloch M, Trotter J, Kinsley L, Greenoak G (2010). *Small amounts of zinc from zinc oxide particles in sunscreens applied outdoors are absorbed through human skin*. **Toxicol Sci** 118(1): 140-149.

Gulson B, Wong H, Korsch M, Gomez L, Casey P, McCall M, McCulloch M, Trotter J, Stauber J, Greenoak G (2012). *Comparison of dermal absorption of zinc from different sunscreen formulations and differing UV exposure based on stable isotope tracing*. **Sci Total Environ** 420: 313-318.

Guo M, Xu X, Yan X, Wang S, Gao S, Zhu S (2013). *In vivo biodistribution and synergistic toxicity of silica nanoparticles and cadmium chloride in mice*. **J Hazard Mater** 260: 780-788.

Hack CE, Covington TR, Lawrence G, Shipp AM, Gentry R, Yager J, Clewell HJ (2007). *A pharmacokinetic model of the intracellular dosimetry of inhaled nickel*. **J Toxicol Environ Health A** 70(5): 445-464.

Han SG, Lee JS, Ahn K, Kim YS, Kim JK, Lee JH, Shin JH, Jeon KS, Cho WS, Song NW, Gulumian M, Shin BS, Yu IJ (2015). *Size-dependent clearance of gold nanoparticles from lungs of Sprague-Dawley rats after short-term inhalation exposure*. **Arch Toxicol** 89(7): 1083-1094.

He B, Lin P, Jia Z, Du W, Qu W, Yuan L, Dai W, Zhang H, Wang X, Wang J, Zhang X, Zhang Q (2013). *The transport mechanisms of polymer nanoparticles in Caco-2 epithelial cells*. **Biomaterials** 34(25): 6082-6098.

He Q, Zhang Z, Gao F, Li Y, Shi J (2011). *In vivo biodistribution and urinary excretion of mesoporous silica nanoparticles: effects of particle size and PEGylation*. **Small** 7(2): 271-280.

He X, Zhang H, Ma Y, Bai W, Zhang Z, Lu K, Ding Y, Zhao Y, Chai Z (2010). *Lung deposition and extrapulmonary translocation of nano-ceria after intratracheal instillation*. **Nanotechnology** 21(28): 285103.

Hillyer JF, Albrecht RM (2001). *Gastrointestinal persorption and tissue distribution of differently sized colloidal gold nanoparticles*. **J Pharm Sci** 90(12): 1927-1936.

Hirai T, Yoshikawa T, Nabeshi H, Yoshida T, Akase T, Yoshioka Y, Itoh N, Tsutsumi Y (2012). *Dermal absorption of amorphous nanosilica particles after topical exposure for three days*. **Pharmazie** 67(8): 742-743.

Hirn S, Semmler-Behnke M, Schleh C, Wenk A, Lipka J, Schaffler M, Takenaka S, Moller W, Schmid G, Simon U, Kreyling WG (2011). *Particle size-dependent and surface charge-dependent biodistribution of gold nanoparticles after intravenous administration*. **Eur J Pharm Biopharm** 77(3): 407-416.

Holt BD, Dahl KN, Islam MF (2012). *Cells take up and recover from protein-stabilized single-wall carbon nanotubes with two distinct rates*. **ACS Nano** 6(4): 3481-3490.

Hopkins LE, Patchin ES, Chiu PL, Brandenberger C, Smiley-Jewell S, Pinkerton KE (2014). *Nose-to-brain transport of aerosolised quantum dots following acute exposure*. **Nanotoxicology** 8(8): 885-893.

Huang J, Bu L, Xie J, Chen K, Cheng Z, Li X, Chen X (2010). *Effects of nanoparticle size on cellular uptake and liver MRI with polyvinylpyrrolidone-coated iron oxide nanoparticles*. **ACS Nano** 4(12): 7151-7160.

Huang X, Li L, Liu T, Hao N, Liu H, Chen D, Tang F (2011). *The shape effect of mesoporous silica nanoparticles on biodistribution, clearance, and biocompatibility in vivo*. **ACS Nano** 5(7): 5390-5399.

Huang X, Zhang F, Zhu L, Choi KY, Guo N, Guo J, Tackett K, Anilkumar P, Liu G, Quan Q, Choi HS, Niu G, Sun YP, Lee S, Chen X (2013). *Effect of injection routes on the biodistribution, clearance, and tumor uptake of carbon dots*. **ACS Nano** 7(7): 5684-5693.

Huang Y, Yu F, Park YS, Wang J, Shin MC, Chung HS, Yang VC (2010). *Co-administration of protein drugs with gold nanoparticles to enable percutaneous delivery*. **Biomaterials** 31(34): 9086-9091.

Huhn D, Kantner K, Geidel C, Brandholt S, De Cock I, Soenen SJ, Rivera Gil P, Montenegro JM, Braeckmans K, Mullen K, Nienhaus GU, Klapper M, Parak WJ (2013). *Polymer-coated nanoparticles interacting with proteins and cells: focusing on the sign of the net charge*. **ACS Nano** 7(4): 3253-3263.

Husain M, Wu D, Saber AT, Decan N, Jacobsen NR, Williams A, Yauk CL, Wallin H, Vogel U, Halappanavar S (2015). *Intratracheally instilled titanium dioxide nanoparticles translocate to heart and liver and activate complement cascade in the heart of C57BL/6 mice*. **Nanotoxicology** 9(8): 1013-1022.

Hussain S, Vanoirbeek JA, Haenen S, Haufroid V, Boland S, Marano F, Nemery B, Hoet PH (2013). *Prior lung inflammation impacts on body distribution of gold nanoparticles*. **Biomed Res Int** 2013: 923475.

Janer G, Mas del Molino E, Fernandez-Rosas E, Fernandez A, Vazquez-Campos S (2014). *Cell uptake and oral absorption of titanium dioxide nanoparticles*. **Toxicol Lett** 228(2): 103-110.

Jani P, Halbert GW, Langridge J, Florence AT (1989). *The uptake and translocation of latex nanospheres and microspheres after oral administration to rats*. **J Pharm Pharmacol** 41(12): 809-812.

Jani P, Halbert GW, Langridge J, Florence AT (1990). *Nanoparticle uptake by the rat gastrointestinal mucosa: quantitation and particle size dependency*. **J Pharm Pharmacol** 42(12): 821-826.

Jani PU, Mccarthy DE, Florence AT (1994). *Titanium-Dioxide (Rutile) Particle Uptake from the Rat Gi Tract and Translocation to Systemic Organs after Oral-Administration*. **Int J Pharm** 105(2): 157-168.

Jani PU, Nomura T, Yamashita F, Takakura Y, Florence AT, Hashida M (1996). *Biliary excretion of polystyrene microspheres with covalently linked FITC fluorescence after oral and parenteral administration to male Wistar rats*. **J Drug Target** 4(2): 87-93.

Jeong SH, Kim JH, Yi SM, Lee JP, Sohn KH, Park KL, Kim MK, Son SW (2010). *Assessment of penetration of quantum dots through in vitro and in vivo human skin using the human skin equivalent model and the tape stripping method*. **Biochem Biophys Res Commun** 394(3): 612-615.

Ji JH, Jung JH, Kim SS, Yoon JU, Park JD, Choi BS, Chung YH, Kwon IH, Jeong J, Han BS, Shin JH, Sung JH, Song KS, Yu IJ (2007). *Twenty-eight-day inhalation toxicity study of silver nanoparticles in Sprague-Dawley rats*. **Inhal Toxicol** 19(10): 857-871.

Jiang XE, Rocker C, Hafner M, Brandholt S, Dorlich RM, Nienhaus GU (2010). *Endo- and Exocytosis of Zwitterionic Quantum Dot Nanoparticles by Live HeLa Cells*. **ACS Nano** 4(11): 6787-6797.

Jin H, Heller DA, Sharma R, Strano MS (2009). *Size-dependent cellular uptake and expulsion of single-walled carbon nanotubes: single particle tracking and a generic uptake model for nanoparticles*. **ACS Nano** 3(1): 149-158.

Johanson G (2010) *Modeling of disposition*. In: McQueen CA, ed. **Comprehensive Toxicology**. Academic Press, Oxford UK. Vol 1, 2nd edition, pp 153-178.

Johanson G, Rauma M (2008). *Basis for skin notation. Part 1. Dermal penetration data for substances on the Swedish OEL list*. **Arbete och Hälsa** 42(2): 1-235.

Jung C, Kaul MG, Bruns OT, Ducic T, Freund B, Heine M, Reimer R, Meents A, Salmen SC, Weller H, Nielsen P, Adam G, Heeren J, Ittrich H (2014). *Intraperitoneal injection improves the uptake of nanoparticle-labeled high-density lipoprotein to atherosclerotic plaques compared with intravenous injection: a multimodal imaging study in ApoE knockout mice*. **Circ Cardiovasc Imaging** 7(2): 303-311.

Kato S, Aoshima H, Saitoh Y, Miwa N (2009). *Biological safety of LipoFullerene composed of squalane and fullerene-C60 upon mutagenesis, photocytotoxicity, and permeability into the human skin tissue*. **Basic Clin Pharmacol Toxicol** 104(6): 483-487.

Kato S, Itoh K, Yaoi T, Tozawa T, Yoshikawa Y, Yasui H, Kanamura N, Hoshino A, Manabe N, Yamamoto K, Fushiki S (2010). *Organ distribution of quantum dots after intraperitoneal administration, with special reference to area-specific distribution in the brain*. **Nanotechnology** 21(33): 335103.

Katsnelson BA, Degtyareva TD, Minigalieva, II, Privalova LI, Kuzmin SV, Yeremenko OS, Kireyeva EP, Sutunkova MP, Valamina, II, Khodos MY, Kozitsina AN, Shur VY, Vazhenin VA, Potapov AP, Morozova MV (2011). *Subchronic systemic toxicity and bioaccumulation of Fe3O4 nano- and microparticles following repeated intraperitoneal administration to rats*. **Int J Toxicol** 30(1): 59-68.

Keller J, Wohlleben W, Ma-Hock L, Strauss V, Groters S, Kuttler K, Wiench K, Herden C, Oberdorster G, van Ravenzwaay B, Landsiedel R (2014). *Time course of lung retention and toxicity of inhaled particles: short-term exposure to nano-Ceria*. **Arch Toxicol** 88(11): 2033-2059.

Kermanizadeh A, Balharry D, Wallin H, Loft S, Moller P (2015). *Nanomaterial translocation--the biokinetics, tissue accumulation, toxicity and fate of materials in secondary organs--a review*. **Crit Rev Toxicol** 45(10): 837-872.

Kertesz Z, Szikszai Z, Gontier E, Moretto P, Surleve-Bazeille JE, Kiss B, Juhasz I, Hunyadi J, Kiss AZ (2005). *Nuclear microprobe study of TiO2-penetration in the epidermis of human skin xenografts*. **Nucl Instrum Meth B** 231: 280-285.

Kim B, Han G, Toley BJ, Kim CK, Rotello VM, Forbes NS (2010). *Tuning payload delivery in tumour cylindroids using gold nanoparticles*. **Nat Nanotechnol** 5(6): 465-472.

Kim S, Lim YT, Soltesz *EG*, De Grand AM, Lee J, Nakayama A, Parker JA, Mihaljevic T, Laurence RG, Dor DM, Cohn LH, Bawendi MG, Frangioni JV (2004). *Near-infrared fluorescent type II quantum dots for sentinel lymph node mapping*. **Nat Biotechnol** 22(1): 93-97.

Kim Y, Lobatto ME, Kawahara T, Chung BL, Mieszawska AJ, Sanchez-Gaytan BL, Fay F, Senders ML, Calcagno C, Becraft J, Saung MT, Gordon RE, Stroes ESG, Ma MM, Farokhzad OC, Fayad ZA, Mulder WJM, Langer R (2014). *Probing nanoparticle translocation across the permeable endothelium in experimental atherosclerosis*. **Proc Natl Acad Sci USA** 111(3): 1078-1083.

Kim YS, Kim JS, Cho HS, Rha DS, Kim JM, Park JD, Choi BS, Lim R, Chang HK, Chung YH, Kwon IH, Jeong J, Han BS, Yu IJ (2008). *Twenty-eight-day oral toxicity, genotoxicity, and gender-related tissue distribution of silver nanoparticles in Sprague-Dawley rats*. **Inhal Toxicol** 20(6): 575-583.

Kim YS, Song MY, Park JD, Song KS, Ryu HR, Chung YH, Chang HK, Lee JH, Oh KH, Kelman BJ, Hwang IK, Yu IJ (2010). *Subchronic oral toxicity of silver nanoparticles*. **Part Fibre Toxicol** 7: 20.

Kiss B, Biro T, Czifra G, Toth BI, Kertesz Z, Szikszai Z, Kiss AZ, Juhasz I, Zouboulis CC, Hunyadi J (2008). *Investigation of micronized titanium dioxide penetration in human skin xenografts and its effect on cellular functions of human skin-derived cells*. **Exp Dermatol** 17(8): 659-667.

Kleinstreuer C, Zhang Z, Li Z (2008). *Modeling airflow and particle transport/deposition in pulmonary airways*. **Resp Physiol Neurobiol** 163(1-3): 128-138.

Kobayashi H, Kawamoto S, Saga T, Sato N, Ishimori T, Konishi J, Ono K, Togashi K, Brechbiel MW (2001). *Avidin-dendrimer-(1B4M-Gd)(254): a tumor-targeting therapeutic agent for gadolinium neutron capture therapy of intraperitoneal disseminated tumor which can be monitored by MRI*. **Bioconjug Chem** 12(4): 587-593.

Kohli AK, Alpar HO (2004). *Potential use of nanoparticles for transcutaneous vaccine delivery: effect of particle size and charge*. **Int J Pharm** 275(1-2): 13-17.

Kolanjiyil AV, Kleinstreuer C (2013). *Nanoparticle mass transfer from lung airways to systemic regions--Part I: Whole-Lung Aerosol Dynamics*. **J Biomech Eng** 135(12): 121003.

Kolanjiyil AV, Kleinstreuer C (2013). *Nanoparticle mass transfer from lung airways to systemic regions--Part II: Multi-compartmental modeling*. **J Biomech Eng** 135(12): 121004.

Konduru NV, Murdaugh KM, Sotiriou GA, Donaghey TC, Demokritou P, Brain JD, Molina RM (2014). *Bioavailability, distribution and clearance of tracheally-instilled and gavaged uncoated or silica-coated zinc oxide nanoparticles*. **Part Fibre Toxicol** 11: 44.

Konduru NV, Murdaugh KM, Swami A, Jimenez RJ, Donaghey TC, Demokritou P, Brain JD, Molina RM (2015). *Surface modification of zinc oxide nanoparticles with amorphous silica alters their fate in the circulation*. **Nanotoxicology**: 1-8.

Korani M, Rezayat SM, Arbabi Bidgoli S (2013). *Sub-chronic Dermal Toxicity of Silver Nanoparticles in Guinea Pig: Special Emphasis to Heart, Bone and Kidney Toxicities*. **Iran J Pharm Res** 12(3): 511-519.

Korani M, Rezayat SM, Gilani K, Arbabi Bidgoli S, Adeli S (2011). *Acute and subchronic dermal toxicity of nanosilver in guinea pig*. **Int J Nanomed** 6: 855-862.

Kreyling WG, Fertsch-Gapp S, Schaffler M, Johnston BD, Haberl N, Pfeiffer C, Diendorf J, Schleh C, Hirn S, Semmler-Behnke M, Epple M, Parak WJ (2014). *In vitro and in vivo interactions of selected nanoparticles with rodent serum proteins and their consequences in biokinetics*. **Beilstein J Nanotechnol** 5: 1699-1711.

Kreyling WG, Hirn S, Moller W, Schleh C, Wenk A, Celik G, Lipka J, Schaffler M, Haberl N, Johnston BD, Sperling R, Schmid G, Simon U, Parak WJ, Semmler-Behnke M (2014). *Air-blood barrier translocation of tracheally instilled gold nanoparticles inversely depends on particle size*. **ACS Nano** 8(1): 222-233.

Kreyling WG, Semmler-Behnke M, Seitz J, Scymczak W, Wenk A, Mayer P, Takenaka S, Oberdörster G (2009). *Size dependence of the translocation of inhaled iridium and carbon nanoparticle aggregates from the lung of rats to the blood and secondary target organs*. **Inhal Toxicol** 21 Suppl 1: 55-60.

Kreyling WG, Semmler M, Erbe F, Mayer P, Takenaka S, Schulz H, Oberdörster G, Ziesenis A (2002). *Translocation of ultrafine insoluble iridium particles from lung epithelium to extrapulmonary organs is size dependent but very low*. **J Toxicol Environ Health A** 65(20): 1513-1530.

Kubota R, Tahara M, Shimizu K, Sugimoto N, Hirose A, Nishimura T (2011). *Time-dependent variation in the biodistribution of C(6)(0) in rats determined by liquid chromatography-tandem mass spectrometry*. **Toxicol Lett** 206(2): 172-177.

Kuempel ED, Tran CL, Bailer AJ, Smith RJ, Dankovic DA, Stayner LT (2001). *Methodological issues of using observational human data in lung dosimetry models for particulates*. **Sci Total Environ** 274(1-3): 67-77.

Kumari M, Kumari SI, Grover P (2014). *Genotoxicity analysis of cerium oxide micro and nanoparticles in Wistar rats after 28 days of repeated oral administration*. **Mutagenesis** 29(6): 467-479.

Kuo TR, Wu CL, Hsu CT, Lo W, Chiang SJ, Lin SJ, Dong CY, Chen CC (2009). *Chemical enhancer induced changes in the mechanisms of transdermal delivery of zinc oxide nanoparticles*. **Biomaterials** 30(16): 3002-3008.

Kwon JT, Hwang SK, Jin H, Kim DS, Minai-Tehrani A, Yoon HJ, Choi M, Yoon TJ, Han DY, Kang YW, Yoon BI, Lee JK, Cho MH (2008). *Body distribution of inhaled fluorescent magnetic nanoparticles in the mice*. **J Occup Health** 50(1): 1-6.

Kwon JT, Minai-Tehrani A, Hwang SK, Kim JE, Shin JY, Yu KN, Chang SH, Kim DS, Kwon YT, Choi IJ, Cheong YH, Kim JS, Cho MH (2012). *Acute pulmonary toxicity and body distribution of inhaled metallic silver nanoparticles*. **Toxicological Res** 28(1): 25-31.

Labouta HI, Liu DC, Lin LL, Butler MK, Grice JE, Raphael AP, Kraus T, El-Khordagui LK, Soyer HP, Roberts MS, Schneider M, Prow TW (2011). *Gold nanoparticle penetration and reduced metabolism in human skin by toluene*. **Pharm Res** 28(11): 2931-2944.

Lademann J, Weigmann H, Rickmeyer C, Barthelmes H, Schaefer H, Mueller G, Sterry W (1999). *Penetration of titanium dioxide microparticles in a sunscreen formulation into the horny layer and the follicular orifice*. **Skin Pharmacol Appl Skin Physiol** 12(5): 247-256.

Lai SK, Wang YY, Hanes J (2009). *Mucus-penetrating nanoparticles for drug and gene delivery to mucosal tissues*. **Adv Drug Deliv Rev** 61(2): 158-171.

Langston Suen WL, Chau Y (2014). *Size-dependent internalisation of folate-decorated nanoparticles via the pathways of clathrin and caveolae-mediated endocytosis in ARPE-19 cells*. **J Pharm Pharmacol** 66(4): 564-573.

Lankveld DP, Oomen AG, Krystek P, Neigh A, Troost-de Jong A, Noorlander CW, Van Eijkeren JC, Geertsma RE, De Jong WH (2010). *The kinetics of the tissue distribution of silver nanoparticles of different sizes*. **Biomaterials** 31(32): 8350-8361.

Larese F, Gianpietro A, Venier M, Maina G, Renzi N (2007). *In vitro percutaneous absorption of metal compounds*. **Toxicol Lett** 170(1): 49-56.

Larese FF, D'Agostin F, Crosera M, Adami G, Renzi N, Bovenzi M, Maina G (2009). *Human skin penetration of silver nanoparticles through intact and damaged skin*. **Toxicology** 255(1-2): 33-37.

Larese Filon F, Crosera M, Timeus E, Adami G, Bovenzi M, Ponti J, Maina G (2013). *Human skin penetration of cobalt nanoparticles through intact and damaged skin*. **Toxicol In Vitro** 27(1): 121-127.

Larese Filon F, Mauro M, Adami G, Bovenzi M, Crosera M (2015). *Nanoparticles skin absorption: New aspects for a safety profile evaluation*. **Reg Toxicol Pharmacol** 72: 310-322.

Lasagna-Reeves C, Gonzalez-Romero D, Barria MA, Olmedo I, Clos A, Sadagopa Ramanujam VM, Urayama A, Vergara L, Kogan MJ, Soto C (2010). *Bioaccumulation and toxicity of gold nanoparticles after repeated administration in mice*. **Biochem Biophys Res Commun** 393(4): 649-655.

Lee CH, Cheng SH, Wang YJ, Chen YC, Chen NT, Souris J, Chen CT, Mou CY, Yang CS, Lo LW (2009). *Near-Infrared Mesoporous Silica Nanoparticles for Optical Imaging: Characterization and In Vivo Biodistribution*. **Adv Funct Mater** 19(2): 215-222.

Lee CM, Jeong HJ, Kim DW, Sohn MH, Lim ST (2012). *The effect of fluorination of zinc oxide nanoparticles on evaluation of their biodistribution after oral administration*. **Nanotechnology** 23(20).

Lee CM, Jeong HJ, Yun KN, Kim DW, Sohn MH, Lee JK, Jeong J, Lim ST (2012). *Optical imaging to trace near infrared fluorescent zinc oxide nanoparticles following oral exposure*. **Int J Nanomed** 7: 3203-3209.

Lee HA, Leavens TL, Mason SE, Monteiro-Riviere NA, Riviere JE (2009). *Comparison of quantum dot biodistribution with a blood-flow-limited physiologically based pharmacokinetic model*. **Nano Lett** 9(2): 794-799.

Lee JA, Kim MK, Paek HJ, Kim YR, Lee JK, Jeong J, Choi SJ (2014). *Tissue distribution and excretion kinetics of orally administered silica nanoparticles in rats*. **Int J Nanomed** 9 Suppl 2: 251-260.

Lee JH, Kim YS, Song KS, Ryu HR, Sung JH, Park JD, Park HM, Song NW, Shin BS, Marshak D, Ahn K, Lee JE, Yu IJ (2013). *Biopersistence of silver nanoparticles in tissues from Sprague-Dawley rats*. **Part Fibre Toxicol** 10: 36.

Lee O, Jeong SH, Shin WU, Lee G, Oh C, Son SW (2013). *Influence of surface charge of gold nanorods on skin penetration*. **Skin Res Technol** 19(1): e390-396.

Lee Y, Kim P, Yoon J, Lee B, Choi K, Kil KH, Park K (2013). *Serum kinetics, distribution and excretion of silver in rabbits following 28 days after a single intravenous injection of silver nanoparticles*. **Nanotoxicology** 7(6): 1120-1130.

Lesniak A, Salvati A, Santos-Martinez MJ, Radomski MW, Dawson KA, Aberg C (2013). *Nanoparticle adhesion to the cell membrane and its effect on nanoparticle uptake efficiency*. **J Am Chem Soc** 135(4): 1438-1444.

Li CH, Shen CC, Cheng YW, Huang SH, Wu CC, Kao CC, Liao JW, Kang JJ (2011). *Organ biodistribution, clearance, and genotoxicity of orally administered zinc oxide nanoparticles in mice*. **Nanotoxicology**.

Li CH, Shen CC, Cheng YW, Huang SH, Wu CC, Kao CC, Liao JW, Kang JJ (2012). *Organ biodistribution, clearance, and genotoxicity of orally administered zinc oxide nanoparticles in mice*. **Nanotoxicology** 6(7): 746-756.

Li D, Johanson G, Emond C, Carlander U, Philbert M, Jolliet O (2014). *Physiologically based pharmacokinetic modeling of polyethylene glycol-coated polyacrylamide nanoparticles in rats*. **Nanotoxicology** 8 Suppl 1: 128-137.

Li M, Al-Jamal KT, Kostarelos K, Reineke J (2010). *Physiologically based pharmacokinetic modeling of nanoparticles*. **ACS Nano** 4(11): 6303-6317.

Li M, Panagi Z, Avgoustakis K, Reineke J (2012). *Physiologically based pharmacokinetic modeling of PLGA nanoparticles with varied mPEG content*. **Int J Nanomed** 7: 1345-1356.

Li M, Reineke J (2011). *Mathemathical modelling of nanoparticle biodistribution: extrapolation among intravenous, oral and pulmonary administration routes*. **Int J Nano Biomater** 3(3): 222-238.

Libutti SK, Paciotti GF, Byrnes AA, Alexander HR, Jr., Gannon WE, Walker M, Seidel GD, Yuldasheva N, Tamarkin L (2010). *Phase I and pharmacokinetic studies of CYT-6091, a novel PEGylated colloidal gold-rhTNF nanomedicine*. **Clin Cancer Res** 16(24): 6139-6149.

Lin P, Chen JW, Chang LW, Wu JP, Redding L, Chang H, Yeh TK, Yang CS, Tsai MH, Wang HJ, Kuo YC, Yang RS (2008). *Computational and ultrastructural toxicology of a nanoparticle, Quantum Dot 705, in mice*. **Environ Sci Technol** 42(16): 6264-6270.

Lin Z, Monteiro-Riviere NA, Kannan R, Riviere JE (2016). *A computational framework for interspecies pharmacokinetics, exposure and toxicity assessment of gold nanoparticles*. **Nanomedicine (Lond)** 11(2): 107-119.

Lin Z, Monteiro-Riviere NA, Riviere JE (2015). *Pharmacokinetics of metallic nanoparticles*. **Wiley Interdiscip Rev Nanomed Nanobiotechnol** 7(18): 189-217.

Lin Z, Monteiro-Riviere NA, Riviere JE (2016). *A physiologically based pharmacokinetic model for polyethylene glycol-coated gold nanoparticles of different sizes in adult mice*. **Nanotoxicology** 10(2): 162-172.

Lipka J, Semmler-Behnke M, Sperling RA, Wenk A, Takenaka S, Schleh C, Kissel T, Parak WJ, Kreyling WG (2010). *Biodistribution of PEG-modified gold nanoparticles following intratracheal instillation and intravenous injection*. **Biomaterials** 31(25): 6574-6581.

Liu S, Jones L, Gu FX (2012). *Nanomaterials for ocular drug delivery*. **Macromol Biosci** 12(5): 608-620.

Loeschner K, Hadrup N, Hansen M, Pereira SA, Gammelgaard B, Moller LH, Mortensen A, Lam HR, Larsen EH (2014). *Absorption, distribution, metabolism and excretion of selenium following oral administration of elemental selenium nanoparticles or selenite in rats*. **Metallomics** 6(2): 330-337.

Loeschner K, Hadrup N, Qvortrup K, Larsen A, Gao X, Vogel U, Mortensen A, Lam HR, Larsen EH (2011). *Distribution of silver in rats following 28 days of repeated oral exposure to silver nanoparticles or silver acetate*. **Part Fibre Toxicol** 8: 18.

Longmire M, Choyke PL, Kobayashi H (2008). *Clearance properties of nano-sized particles and molecules as imaging agents: considerations and caveats*. **Nanomedicine** 3(5): 703-717.

Luciani N, Gazeau F, Wilhelm C (2009). *Reactivity of the monocyte/macrophage system to superparamagnetic anionic nanoparticles*. **J Mater Chem** 19(35): 6373-6380.

Lundqvist M, Stigler J, Cedervall T, Berggard T, Flanagan MB, Lynch I, Elia G, Dawson K (2011). *The evolution of the protein corona around nanoparticles: a test study*. **ACS Nano** 5(9): 7503-7509.

Lunov O, Zablotskii V, Syrovets T, Rocker C, Tron K, Nienhaus GU, Simmet T (2011). *Modeling receptor-mediated endocytosis of polymer-functionalized iron oxide nanoparticles by human macrophages*. **Biomaterials** 32(2): 547-555.

Lupi M, Colombo C, Frapolli R, Ferrari R, Sitia L, Dragoni L, Bello E, Licandro SA, Falcetta F, Ubezio P, Bigini P, Salmona M, D'Incalci M, Morbidelli M, Moscatelli D (2014). *A biodistribution study of PEGylated PCL-based nanoparticles in C57BL/6 mice bearing B16/F10 melanoma*. **Nanotechnology** 25(33): 335706.

Ma-Hock L, Brill S, Wohlleben W, Farias PM, Chaves CR, Tenorio DP, Fontes A, Santos BS, Landsiedel R, Strauss V, Treumann S, Ravenzwaay B (2012). *Short term inhalation toxicity of a liquid aerosol of CdS/Cd(OH)(2) core shell quantum dots in male Wistar rats*. **Toxicol Lett** 208(2): 115-124.

Ma-Hock L, Farias PM, Hofmann T, Andrade AC, Silva JN, Arnaud TM, Wohlleben W, Strauss V, Treumann S, Chaves CR, Groters S, Landsiedel R, van Ravenzwaay B (2014). *Short term inhalation toxicity of a liquid aerosol of glutaraldehyde-coated CdS/Cd(OH)2 core shell quantum dots in rats*. **Toxicol Lett** 225(1): 20-26.

MacCalman L, Tran CL, Kuempel E (2009). *Development of a bio-mathematical model in rats to describe clearance, retention and translocation of inhaled nano particles throughout the body*. **Inhaled Particles X, J Phys Conf Ser** 151.

Mager DE, Mody V, Xu C, Forrest A, Lesniak WG, Nigavekar SS, Kariapper MT, Minc L, Khan MK, Balogh LP (2012). *Physiologically based pharmacokinetic model for composite nanodevices: effect of charge and size on in vivo disposition*. **Pharm Res** 29(9): 2534-2542.

Mahe B, Vogt A, Liard C, Duffy D, Abadie V, Bonduelle O, Boissonnas A, Sterry W, Verrier B, Blume-Peytavi U, Combadiere B (2009). *Nanoparticle-based targeting of vaccine compounds to skin antigen-presenting cells by hair follicles and their transport in mice*. **J Invest Dermatol** 129(5): 1156-1164.

Maincent P, Thouvenot P, Amicabile C, Hoffman M, Kreuter J, Couvreur P, Devissaguet JP (1992). *Lymphatic targeting of polymeric nanoparticles after intraperitoneal administration in rats*. **Pharm Res** 9(12): 1534-1539.

Maiolo D, Del Pino P, Metrangolo P, Parak WJ, Baldelli Bombelli F (2015). *Nanomedicine delivery: does protein corona route to the target or off road?* **Nanomedicine (London UK)** 10(21): 3231-3247.

Martina MS, Wilhelm C, Lesieur S (2008). *The effect of magnetic targeting on the uptake of magnetic-fluid-loaded liposomes by human prostatic adenocarcinoma cells*. **Biomaterials** 29(30): 4137-4145.

Mavon A, Miquel C, Lejeune O, Payre B, Moretto P (2007). *In vitro percutaneous absorption and in vivo stratum corneum distribution of an organic and a mineral sunscreen*. **Skin Pharmacol Physiol** 20(1): 10-20.

McClean S, Prosser E, Meehan E, O'Malley D, Clarke N, Ramtoola Z, Brayden D (1998). *Binding and uptake of biodegradable poly-DL-lactide micro- and nanoparticles in intestinal epithelia*. **Eur J Pharm Sci** 6(2): 153-163.

McDevitt MR, Chattopadhyay D, Jaggi JS, Finn RD, Zanzonico PB, Villa C, Rey D, Mendenhall J, Batt CA, Njardarson JT, Scheinberg DA (2007). *PET imaging of soluble yttrium-86-labeled carbon nanotubes in mice*. **PLoS One** 2(9): e907.

Menzel F, Reinert T, Vogt J, Butz T (2004). *Investigations of percutaneous uptake of ultrafine TiO2 particles at the high energy ion nanoprobe LIPSION*. **Nucl Instrum Meth B** 219: 82-86.

Mercer RR, Scabilloni JF, Hubbs AF, Wang L, Battelli LA, McKinney W, Castranova V, Porter DW (2013). *Extrapulmonary transport of MWCNT following inhalation exposure*. **Part Fibre Toxicol** 10: 38.

Michel CC, Curry FE (1999). *Microvascular permeability*. **Physiol Rev** 79(3): 703-761.

Midander K, Pan J, Wallinder IO, Heim K, Leygraf C (2007). *Nickel release from nickel particles in artificial sweat*. **Contact Dermatitis** 56(6): 325-330.

Midander K, Pan J, Wallinder IO, Leygraf C (2007). *Metal release from stainless steel particles in vitro-influence of particle size*. **J Environ Monit** 9(1): 74-81.

Midander K, Wallinder IO, Leygraf C (2007). *In vitro studies of copper release from powder particles in synthetic biological media*. **Environ Pollut** 145(1): 51-59.

Moghimi SM, Hunter AC, Murray JC (2001). *Long-circulating and target-specific nanoparticles: theory to practice*. **Pharmacol Rev** 53(2): 283-318.

Monteiro-Riviere NA, Wiench K, Landsiedel R, Schulte S, Inman AO, Riviere JE (2011). *Safety evaluation of sunscreen formulations containing titanium dioxide and zinc oxide nanoparticles in UVB sunburned skin: an in vitro and in vivo study*. **Toxicol Sci** 123(1): 264-280.

Morsy GM, El-Ala KS, Ali AA (2016). *Studies on fate and toxicity of nanoalumina in male albino rats: Lethality, bioaccumulation and genotoxicity*. **Toxicol Ind Health** 32(2): 344-359.

Mortensen LJ, Jatana S, Gelein R, De Benedetto A, De Mesy Bentley KL, Beck LA, Elder A, Delouise LA (2013). *Quantification of quantum dot murine skin penetration with UVR barrier impairment*. **Nanotoxicology** 7(8): 1386-1398.

Mortensen LJ, Oberdörster G, Pentland AP, Delouise LA (2008). *In vivo skin penetration of quantum dot nanoparticles in the murine model: the effect of UVR*. **Nano Lett** 8(9): 2779-2787.

Moussa F, Pressac M, Genin E, Roux S, Trivin F, Rassat A, Ceolin R, Szwarc H (1997). *Quantitative analysis of C60 fullerene in blood and tissues by high-performance liquid chromatography with photodiode-array and mass spectrometric detection*. **J Chromatogr B Biomed Sci Appl** 696(1): 153-159.

Mühlfeld C, Geiser M, Kapp N, Gehr P, Rothen-Rutishauser B (2007). *Re-evaluation of pulmonary titanium dioxide nanoparticle distribution using the "relative deposition index": Evidence for clearance through microvasculature*. **Part Fibre Toxicol** 4: 7.

Mörk AK, Johanson G (2010). *Chemical-specific adjustment factors for intraspecies variability of acetone toxicokinetics using a probabilistic approach*. **Toxicol Sci** 116(1): 336-348.

Nabeshi H, Yoshikawa T, Matsuyama K, Nakazato Y, Matsuo K, Arimori A, Isobe M, Tochigi S, Kondoh S, Hirai T, Akase T, Yamashita T, Yamashita K, Yoshida T, Nagano K, Abe Y, Yoshioka Y, Kamada H, Imazawa T, Itoh N, Nakagawa S, Mayumi T, Tsunoda S, Tsutsumi Y (2011). *Systemic distribution, nuclear entry and cytotoxicity of amorphous nanosilica following topical application*. **Biomaterials** 32(11): 2713-2724.

Nemmar A, Hoet PH, Vanquickenborne B, Dinsdale D, Thomeer M, Hoylaerts MF, Vanbilloen H, Mortelmans L, Nemery B (2002). *Passage of inhaled particles into the blood circulation in humans*. **Circulation** 105(4): 411-414.

Nemmar A, Vanbilloen H, Hoylaerts MF, Hoet PH, Verbruggen A, Nemery B (2001). *Passage of intratracheally instilled ultrafine particles from the lung into the systemic circulation in hamster*. **Am J Respir Crit CAre Med** 164(9): 1665-1668.

Oberdörster G, Ferin J, Lehnert BE (1994). *Correlation between Particle-Size, in-Vivo Particle Persistence, and Lung Injury*. **Environ Health Perspect** 102: 173-179.

Oberdörster G, Sharp Z, Atudorei V, Elder A, Gelein R, Kreyling W, Cox C (2004). *Translocation of inhaled ultrafine particles to the brain*. **Inhal Toxicol** 16(6-7): 437-445.

Oberdörster G, Sharp Z, Atudorei V, Elder A, Gelein R, Lunts A, Kreyling W, Cox C (2002). *Extrapulmonary translocation of ultrafine carbon particles following whole-body inhalation exposure of rats*. **J Toxicol Environ Health A** 65(20): 1531-1543.

Ohta S, Inasawa S, Yamaguchi Y (2012). *Real time observation and kinetic modeling of the cellular uptake and removal of silicon quantum dots*. **Biomaterials** 33(18): 4639-4645.

Opitz AW, Wickstrom E, Thakur ML, Wagner NJ (2010). *Physiologically based pharmacokinetics of molecular imaging nanoparticles for mRNA detection determined in tumor-bearing mice*. **Oligonucleotides** 20(3): 117-125.

Osmond-McLeod MJ, Oytam Y, Kirby JK, Gomez-Fernandez L, Baxter B, McCall MJ (2014). *Dermal absorption and short-term biological impact in hairless mice from sunscreens containing zinc oxide nano- or larger particles*. **Nanotoxicology** 8 Suppl 1: 72-84.

Ostrowski A, Nordmeyer D, Boreham A, Brodwolf R, Mundhenk L, Fluhr JW, Lademann J, Graf C, Ruhl E, Alexiev U, Gruber AD (2014). *Skin barrier disruptions in tape stripped and allergic dermatitis models have no effect on dermal penetration and systemic distribution of AHAPS-functionalized silica nanoparticles*. **Nanomedicine** 10(7): 1571-1581.

Paek HJ, Lee YJ, Chung HE, Yoo NH, Lee JA, Kim MK, Lee JK, Jeong J, Choi SJ (2013). *Modulation of the pharmacokinetics of zinc oxide nanoparticles and their fates in vivo*. **Nanoscale** 5(23): 11416-11427.

Palko HA, Fung JY, Louie AY (2010). *Positron emission tomography: a novel technique for investigating the biodistribution and transport of nanoparticles*. **Inhal Toxicol** 22(8): 657-688.

Panyam J, Labhasetwar V (2003). *Dynamics of endocytosis and exocytosis of poly(D,L-lactide-co-glycolide) nanoparticles in vascular smooth muscle cells*. **Pharm Res** 20(2): 212-220.

Park EJ, Bae E, Yi J, Kim Y, Choi K, Lee SH, Yoon J, Lee BC, Park K (2010). *Repeated-dose toxicity and inflammatory responses in mice by oral administration of silver nanoparticles*. **Environ Toxicol Pharmacol** 30(2): 162-168.

Park EJ, Park YK, Park K (2009). *Acute Toxicity and Tissue Distribution of Cerium Oxide Nanoparticles by a Single Oral Administration in Rats* **Toxicological Res KSOT** 25(2): 79-84

Park K (2013). *Toxicokinetic differences and toxicities of silver nanoparticles and silver ions in rats after single oral administration*. **J Toxicol Environ Health A** 76(22): 1246-1260.

Park K, Park EJ, Chun IK, Choi K, Lee SH, Yoon J, Lee BC (2011). *Bioavailability and toxicokinetics of citrate-coated silver nanoparticles in rats*. **Arch Pharm Res** 34(1): 153-158.

Pauluhn J (2009). *Retrospective analysis of 4-week inhalation studies in rats with focus on fate and pulmonary toxicity of two nanosized aluminum oxyhydroxides (boehmite) and pigment-grade iron oxide (magnetite): the key metric of dose is particle mass and not particle surface area*. **Toxicology** 259(3): 140-148.

Peng B, Andrews J, Nestorov I, Brennan B, Nicklin P, Rowland M (2001). *Tissue distribution and physiologically based pharmacokinetics of antisense phosphorothioate oligonucleotide ISIS 1082 in rat*. **Antisense Nucleic Acid Drug Dev** 11(1): 15-27.

Pery AR, Brochot C, Hoet PH, Nemmar A, Bois FY (2009). *Development of a physiologically based kinetic model for 99m-technetium-labelled carbon nanoparticles inhaled by humans*. **Inhal Toxicol** 21(13): 1099-1107.

Petersen LK, Huntimer L, Walz K, Ramer-Tait A, Wannemuehler MJ, Narasimhan B (2013). *Combinatorial evaluation of in vivo distribution of polyanhydride particle-based platforms for vaccine delivery*. **Int J Nanomed** 8: 2213-2225.

Petitot F, Lestaevel P, Tourlonias E, Mazzucco C, Jacquinot S, Dhieux B, Delissen O, Tournier BB, Gensdarmes F, Beaunier P, Dublineau I (2013). *Inhalation of uranium nanoparticles: respiratory tract deposition and translocation to secondary target organs in rats*. **Toxicol Lett** 217(3): 217-225.

Pfeiffer C, Rehbock C, Huhn D, Carrillo-Carrion C, de Aberasturi DJ, Merk V, Barcikowski S, Parak WJ (2014). *Interaction of colloidal nanoparticles with their local environment: the (ionic) nanoenvironment around nanoparticles is different from bulk and determines the physico-chemical properties of the nanoparticles*. **J R Soc Interface** 11(96): 20130931.

Pflucker F, Wendel V, Hohenberg H, Gartner E, Will T, Pfeiffer S, Wepf R, Gers-Barlag H (2001). *The human stratum corneum layer: an effective barrier against dermal uptake of different forms of topically applied micronised titanium dioxide*. **Skin Pharmacol Appl Skin Physiol** 14 Suppl 1: 92-97.

Poland CA, Read SAK, Varet J, Carse G, Christensen FM, Hankin SM (2013) *Dermal absorption of nanomaterials*. Copenhagen, The Danish Environmental Protection Agency. ISBN 978-87-93026-50-6.

Price OT, Asgharian B, Miller FJ, Cassee FR, de Winter-Sorkina R (2002) *Multiple Path Particle Dosimetry Model (MPPD v 1.0): A Model for Human and Rat Airway Particle Dosimetry*. Bilthoven, The Netherlands, National Institute for Public Health and the Environment (RIVM). RIVA Report 650010030.

Prow TW, Monteiro-Riviere NA, Inman AO, Grice JE, Chen X, Zhao X, Sanchez WH, Gierden A, Kendall MA, Zvyagin AV, Erdmann D, Riviere JE, Roberts MS (2012). *Quantum dot penetration into viable human skin*. **Nanotoxicology** 6(2): 173-185.

Rancan F, Gao Q, Graf C, Troppens S, Hadam S, Hackbarth S, Kembuan C, Blume-Peytavi U, Ruhl E, Lademann J, Vogt A (2012). *Skin penetration and cellular uptake of amorphous silica nanoparticles with variable size, surface functionalization, and colloidal stability*. **ACS Nano** 6(8): 6829-6842.

Rancan F, Vogt A (2014). *Getting under the skin: what is the potential of the transfollicular route in drug delivery?* **Ther Deliv** 5(8): 875-877.

Recordati C, De Maglie M, Bianchessi S, Argentiere S, Cella C, Mattiello S, Cubadda F, Aureli F, D'Amato M, Raggi A, Lenardi C, Milani P, Scanziani E (2016). *Tissue distribution and acute toxicity of silver after single intravenous administration in mice: nano-specific and size-dependent effects*. **Part Fibre Toxicol** 13: 12.

Rehberg M, Nekolla K, Sellner S, Praetner M, Mildner K, Zeuschner D, Krombach F (2016). *Intercellular Transport of Nanomaterials is Mediated by Membrane Nanotubes In Vivo*. **Small** 12(14): 1882-1890.

Rinaldo M, Andujar P, Lacourt A, Martinon L, Canal Raffin M, Dumortier P, Pairon JC, Brochard P (2015). *Perspectives in Biological Monitoring of Inhaled Nanosized Particles*. **Ann Occup Hyg** 59(6): 669-680.

Roberts JR, Antonini JM, Porter DW, Chapman RS, Scabilloni JF, Young SH, Schwegler-Berry D, Castranova V, Mercer RR (2013). *Lung toxicity and*

biodistribution of Cd/Se-ZnS quantum dots with different surface functional groups after pulmonary exposure in rats. **Part Fibre Toxicol** 10: 5.

Rouse JG, Yang J, Ryman-Rasmussen JP, Barron AR, Monteiro-Riviere NA (2007). *Effects of mechanical flexion on the penetration of fullerene amino acid-derivatized peptide nanoparticles through skin*. **Nano Lett** 7(1): 155-160.

Ryman-Rasmussen JP, Riviere JE, Monteiro-Riviere NA (2006). *Penetration of intact skin by quantum dots with diverse physicochemical properties*. **Toxicol Sci** 91(1): 159-165.

Ryu HJ, Seo MY, Jung SK, Maeng EH, Lee SY, Jang DH, Lee TJ, Jo KY, Kim YR, Cho KB, Kim MK, Lee BJ, Son SW (2014). *Zinc oxide nanoparticles: a 90-day repeated-dose dermal toxicity study in rats*. **Int J Nanomed** 9 Suppl 2: 137-144.

Sadauskas E, Jacobsen NR, Danscher G, Stoltenberg M, Vogel U, Larsen A, Kreyling W, Wallin H (2009). *Biodistribution of gold nanoparticles in mouse lung following intratracheal instillation*. **Chem Cent J** 3: 16.

Sadauskas E, Wallin H, Stoltenberg M, Vogel U, Doering P, Larsen A, Danscher G (2007). *Kupffer cells are central in the removal of nanoparticles from the organism*. **Part Fibre Toxicol** 4: 10.

Sadrieh N, Wokovich AM, Gopee NV, Zheng J, Haines D, Parmiter D, Siitonen PH, Cozart CR, Patri AK, McNeil SE, Howard PC, Doub WH, Buhse LF (2010). *Lack of significant dermal penetration of titanium dioxide from sunscreen formulations containing nano- and submicron-size TiO2 particles*. **Toxicol Sci** 115(1): 156-166.

Sahneh FD, Scoglio CM, Monteiro-Riviere NA, Riviere JE (2015). *Predicting the impact of biocorona formation kinetics on interspecies extrapolations of nanoparticle biodistribution modeling*. **Nanomedicine (London UK)** 10(1): 25-33.

Sakhtianchi R, Minchin RF, Lee KB, Alkilany AM, Serpooshan V, Mahmoudi M (2013). *Exocytosis of nanoparticles from cells: role in cellular retention and toxicity*. **Adv Colloid Interface Sci** 201-202: 18-29.

Salvati A, Åberg C, dos Santos T, Varela J, Pinto P, Lynch I, Dawson KA (2011). *Experimental and theoretical comparison of intracellular import of polymeric nanoparticles and small molecules: toward models of uptake kinetics*. **Nanomedicine** 7(6): 818-826.

Sarin H (2010). *Physiologic upper limits of pore size of different blood capillary types and another perspective on the dual pore theory of microvascular permeability*. **J Angiogenes Res** 2: 14.

Schleh C, Holzwarth U, Hirn S, Wenk A, Simonelli F, Schaffler M, Moller W, Gibson N, Kreyling WG (2013). *Biodistribution of inhaled gold nanoparticles in mice and the influence of surfactant protein D*. **J Aerosol Med Pulm Drug Deliv** 26(1): 24-30.

Schleh C, Semmler-Behnke M, Lipka J, Wenk A, Hirn S, Schaffler M, Schmid G, Simon U, Kreyling WG (2012). *Size and surface charge of gold nanoparticles determine absorption across intestinal barriers and accumulation in secondary target organs after oral administration*. **Nanotoxicology** 6(1): 36-46.

Schulz J, Hohenberg H, Pflucker F, Gartner E, Will T, Pfeiffer S, Wepf R, Wendel V, Gers-Barlag H, Wittern KP (2002). *Distribution of sunscreens on skin*. **Adv Drug Deliv Rev** 54 Suppl 1: S157-163.

Semmler-Behnke M, Kreyling WG, Lipka J, Fertsch S, Wenk A, Takenaka S, Schmid G, Brandau W (2008). *Biodistribution of 1.4- and 18-nm gold particles in rats*. **Small** 4(12): 2108-2111.

Semmler-Behnke M, Takenaka S, Fertsch S, Wenk A, Seitz J, Mayer P, Oberdörster G, Kreyling WG (2007). *Efficient elimination of inhaled nanoparticles from the alveolar region: evidence for interstitial uptake and subsequent reentrainment onto airways epithelium*. **Environ Health Perspect** 115(5): 728-733.

Semmler M, Seitz J, Erbe F, Mayer P, Heyder J, Oberdörster G, Kreyling WG (2004). *Long-term clearance kinetics of inhaled ultrafine insoluble iridium particles from the rat lung, including transient translocation into secondary organs*. **Inhal Toxicol** 16(6-7): 453-459.

Senzui M, Tamura T, Miura K, Ikarashi Y, Watanabe Y, Fujii M (2010). *Study on penetration of titanium dioxide (TiO(2)) nanoparticles into intact and damaged skin in vitro*. **J Toxicol Sci** 35(1): 107-113.

Shelley ML, Wagner AJ, Hussain SM, Bleckmann C (2008). *Modeling the in vivo case with in vitro nanotoxicity data*. **Int J Toxicol** 27(5): 359-367.

Shim KH, Hulme J, Maeng EH, Kim MK, An SS (2014). *Analysis of zinc oxide nanoparticles binding proteins in rat blood and brain homogenate*. **Int J Nanomed** 9 Suppl 2: 217-224.

Shinohara N, Nakazato T, Tamura M, Endoh S, Fukui H, Morimoto Y, Myojo T, Shimada M, Yamamoto K, Tao H, Yoshida Y, Nakanishi J (2010). *Clearance kinetics of fullerene C(6)(0) nanoparticles from rat lungs after intratracheal C(6)(0) instillation and inhalation C(6)(0) exposure*. **Toxicol Sci** 118(2): 564-573.

Shinohara N, Oshima Y, Kobayashi T, Imatanaka N, Nakai M, Ichinose T, Sasaki T, Zhang GH, Fukui H, Gamo M (2014). *Dose-dependent clearance kinetics of intratracheally administered titanium dioxide nanoparticles in rat lung*. **Toxicology** 325: 1-11.

Singh SP, Rahman MF, Murty US, Mahboob M, Grover P (2013). *Comparative study of genotoxicity and tissue distribution of nano and micron sized iron oxide in rats after acute oral treatment*. **Toxicol Appl Pharmacol** 266(1): 56-66.

Sinnecker H, Krause T, Koelling S, Lautenschlager I, Frey A (2014). *The gut wall provides an effective barrier against nanoparticle uptake*. **Beilstein J Nanotechnol** 5: 2092-2101.

Smulders S, Ketkar-Atre A, Luyts K, Vriens H, De Sousa Nobre S, Rivard C, Van Landuyt K, Baken S, Smolders E, Golanski L, Ghosh M, Vanoirbeek J, Himmelreich U, Hoet PH (2016). *Body distribution of SiO2-Fe3O4 core-shell nanoparticles after intravenous injection and intratracheal instillation*. **Nanotoxicology** 10(5): 567-574.

Smulders S, Luyts K, Brabants G, Landuyt KV, Kirschhock C, Smolders E, Golanski L, Vanoirbeek J, Hoet PH (2014). *Toxicity of nanoparticles embedded in paints compared with pristine nanoparticles in mice*. **Toxicol Sci** 141(1): 132-140.

Snipes MB, Boecker BB, McClellan RO (1983). *Retention of monodisperse or polydisperse aluminosilicate particles inhaled by dogs, rats, and mice*. **Toxicol Appl Pharmacol** 69(3): 345-362.

Sonavane G, Tomoda K, Makino K (2008). *Biodistribution of colloidal gold nanoparticles after intravenous administration: effect of particle size*. **Colloids Surf B Biointerfaces** 66(2): 274-280.

Sonavane G, Tomoda K, Sano A, Ohshima H, Terada H, Makino K (2008). *In vitro permeation of gold nanoparticles through rat skin and rat intestine: Effect of particle size*. **Colloids Surface B Biointerfaces** 65(1): 1-10.

Song KS, Sung JH, Ji JH, Lee JH, Lee JS, Ryu HR, Lee JK, Chung YH, Park HM, Shin BS, Chang HK, Kelman B, Yu IJ (2013). *Recovery from silver-nanoparticle-exposure-induced lung inflammation and lung function changes in Sprague Dawley rats*. **Nanotoxicology** 7(2): 169-180.

Souris JS, Lee CH, Cheng SH, Chen CT, Yang CS, Ho JA, Mou CY, Lo LW (2010). *Surface charge-mediated rapid hepatobiliary excretion of mesoporous silica nanoparticles*. **Biomaterials** 31(21): 5564-5574.

Stayton I, Winiarz J, Shannon K, Ma Y (2009). *Study of uptake and loss of silica nanoparticles in living human lung epithelial cells at single cell level*. **Anal Bioanal Chem** 394(6): 1595-1608.

Stober W (1999). *POCK model simulations of pulmonary quartz dust retention data in extended inhalation exposures of rats*. **Inhal Toxicol** 11(4): 269-292.

Stober W, Morrow PE, Koch W, Morawietz G (1994). *Alveolar Clearance and Retention of Inhaled Insoluble Particles in Rats Simulated by a Model Inferring Macrophage Particle Load Distributions*. **J Aerosol Sci** 25(5): 975-1002.

Sung JH, Ji JH, Park JD, Song MY, Song KS, Ryu HR, Yoon JU, Jeon KS, Jeong J, Han BS, Chung YH, Chang HK, Lee JH, Kim DW, Kelman BJ, Yu IJ (2011). *Subchronic inhalation toxicity of gold nanoparticles*. **Part Fibre Toxicol** 8: 16.

Sung JH, Ji JH, Park JD, Yoon JU, Kim DS, Jeon KS, Song MY, Jeong J, Han BS, Han JH, Chung YH, Chang HK, Lee JH, Cho MH, Kelman BJ, Yu IJ (2009). *Subchronic inhalation toxicity of silver nanoparticles*. **Toxicol Sci** 108(2): 452-461.

Sweeney LM, MacCalman L, Haber LT, Kuempel ED, Tran CL (2015). *Bayesian evaluation of a physiologically-based pharmacokinetic (PBPK) model of long-term kinetics of metal nanoparticles in rats*. **Regul Toxicol Pharmacol** 73(1): 151-163.

Takenaka S, Karg E, Kreyling WG, Lentner B, Moller W, Behnke-Semmler M, Jennen L, Walch A, Michalke B, Schramel P, Heyder J, Schulz H (2006). *Distribution pattern of inhaled ultrafine gold particles in the rat lung*. **Inhal Toxicol** 18(10): 733-740.

Takenaka S, Karg E, Roth C, Schulz H, Ziesenis A, Heinzmann U, Schramel P, Heyder J (2001). *Pulmonary and systemic distribution of inhaled ultrafine silver particles in rats*. **Environ Health Perspect** 109 Suppl 4: 547-551.

Tan MH, Commens CA, Burnett L, Snitch PJ (1996). *A pilot study on the percutaneous absorption of microfine titanium dioxide from sunscreens*. **Australas J Dermatol** 37(4): 185-187.

Tang L, Zhang C, Song G, Jin X, Xu Z (2013). *In vivo skin penetration and metabolic path of quantum dots*. **Sci China Life Sci** 56(2): 181-188.

Tenzer S, Docter D, Kuharev J, Musyanovych A, Fetz V, Hecht R, Schlenk F, Fischer D, Kiouptsi K, Reinhardt C, Landfester K, Schild H, Maskos M, Knauer SK,

Stauber RH (2013). *Rapid formation of plasma protein corona critically affects nanoparticle pathophysiology*. **Nat Nanotechnol** 8(10): 772-781.
Tenzer S, Docter D, Rosfa S, Wlodarski A, Kuharev J, Rekik A, Knauer SK, Bantz C, Nawroth T, Bier C, Sirirattanapan J, Mann W, Treuel L, Zellner R, Maskos M, Schild H, Stauber RH (2011). *Nanoparticle size is a critical physicochemical determinant of the human blood plasma corona: a comprehensive quantitative proteomic analysis*. **ACS Nano** 5(9): 7155-7167.
Tinkle SS, Antonini JM, Rich BA, Roberts JR, Salmen R, DePree K, Adkins EJ (2003). *Skin as a route of exposure and sensitization in chronic beryllium disease*. **Environ Health Perspect** 111(9): 1202-1208.
Tran CL, Jones AD, Cullen RT, Donaldson K (1999). *Exploration of the mechanisms of retention and clearance of low-toxicity particles in the rat lung using a mathematical model*. **Inhal Toxicol** 11(12): 1077-1108.
Tran CL, Jones AD, Cullen RT, Donaldson K (1999). *Mathematical modeling of the retention and clearance of low-toxicity particles in the lung*. **Inhal Toxicol** 11(12): 1059-1076.
Walczak AP, Fokkink R, Peters R, Tromp P, Herrera Rivera ZE, Rietjens IM, Hendriksen PJ, Bouwmeester H (2013). *Behaviour of silver nanoparticles and silver ions in an in vitro human gastrointestinal digestion model*. **Nanotoxicology** 7(7): 1198-1210.
Walczak AP, Kramer E, Hendriksen PJ, Helsdingen R, van der Zande M, Rietjens IM, Bouwmeester H (2015). *In vitro gastrointestinal digestion increases the translocation of polystyrene nanoparticles in an in vitro intestinal co-culture model*. **Nanotoxicology** 9(7): 886-894.
van der Merwe D, Tawde S, Pickrell JA, Erickson LE (2009). *Nanocrystalline titanium dioxide and magnesium oxide in vitro dermal absorption in human skin*. **Cutan Ocul Toxicol** 28(2): 78-82.
van der Zande M, Vandebriel RJ, Van Doren E, Kramer E, Herrera Rivera Z, Serrano-Rojero CS, Gremmer ER, Mast J, Peters RJ, Hollman PC, Hendriksen PJ, Marvin HJ, Peijnenburg AA, Bouwmeester H (2012). *Distribution, elimination, and toxicity of silver nanoparticles and silver ions in rats after 28-day oral exposure*. **ACS Nano** 6(8): 7427-7442.
van Ravenzwaay B, Landsiedel R, Fabian E, Burkhardt S, Strauss V, Ma-Hock L (2009). *Comparing fate and effects of three particles of different surface properties: nano-TiO(2), pigmentary TiO(2) and quartz*. **Toxicol Lett** 186(3): 152-159.
Wang B, Feng WY, Wang M, Shi JW, Zhang F, Ouyang H, Zhao YL, Chai ZF, Huang YY, Xie YN, Wang HF, Wang J (2007). *Transport of intranasally instilled fine Fe2O3 particles into the brain: Micro-distribution, chemical states, and histopathological observation*. **Biol Trace Elem Res** 118(3): 233-243.
Wang B, Feng WY, Wang M, Wang TC, Gu YQ, Zhu MT, Ouyang H, Shi JW, Zhang F, Zhao YL, Chai ZF, Wang HF, Wang J (2008). *Acute toxicological impact of nano- and submicro-scaled zinc oxide powder on healthy adult mice*. **J Nanopart Res** 10(2): 263-276.
Wang J, Liu Y, Jiao F, Lao F, Li W, Gu Y, Li Y, Ge C, Zhou G, Li B, Zhao Y, Chai Z, Chen C (2008). *Time-dependent translocation and potential impairment on*

central nervous system by intranasally instilled TiO(2) nanoparticles. **Toxicology** 254(1-2): 82-90.

Wang J, Zhou G, Chen C, Yu H, Wang T, Ma Y, Jia G, Gao Y, Li B, Sun J, Li Y, Jiao F, Zhao Y, Chai Z (2007). *Acute toxicity and biodistribution of different sized titanium dioxide particles in mice after oral administration*. **Toxicol Lett** 168(2): 176-185.

Wang X, Ji Z, Chang CH, Zhang H, Wang M, Liao YP, Lin S, Meng H, Li R, Sun B, Winkle LV, Pinkerton KE, Zink JI, Xia T, Nel AE (2014). *Use of coated silver nanoparticles to understand the relationship of particle dissolution and bioavailability to cell and lung toxicological potential*. **Small** 10(2): 385-398.

Wang X, Sun K, Tan Y, Wu S, Zhang J (2014). *Efficacy and safety of selenium nanoparticles administered intraperitoneally for the prevention of growth of cancer cells in the peritoneal cavity*. **Free Radic Biol Med** 72: 1-10.

Wang Y, Chen Z, Ba T, Pu J, Chen T, Song Y, Gu Y, Qian Q, Xu Y, Xiang K, Wang H, Jia G (2013). *Susceptibility of young and adult rats to the oral toxicity of titanium dioxide nanoparticles*. **Small** 9(9-10): 1742-1752.

Wang Y, Wu Q, Sui K, Chen XX, Fang J, Hu X, Wu M, Liu Y (2013). *A quantitative study of exocytosis of titanium dioxide nanoparticles from neural stem cells*. **Nanoscale** 5(11): 4737-4743.

Wang Z, Qu G, Su L, Wang L, Yang Z, Jiang J, Liu S, Jiang G (2013). *Evaluation of the biological fate and the transport through biological barriers of nanosilver in mice*. **Curr Pharm Design** 19(37): 6691-6697.

Watkinson AC, Bunge AL, Hadgraft J, Lane ME (2013). *Nanoparticles do not penetrate human skin--a theoretical perspective*. **Pharm Res** 30(8): 1943-1946.

Verner MA, McDougall R, Johanson G (2012). *Using population physiologically based pharmacokinetic modeling to determine optimal sampling times and to interpret biological exposure markers: The example of occupational exposure to styrene*. **Toxicol Lett** 213(2): 299-304.

Wiebert P, Sanchez-Crespo A, Falk R, Philipson K, Lundin A, Larsson S, Moller W, Kreyling WG, Svartengren M (2006). *No significant translocation of inhaled 35-nm carbon particles to the circulation in humans*. **Inhal Toxicol** 18(10): 741-747.

Wiebert P, Sanchez-Crespo A, Seitz J, Falk R, Philipson K, Kreyling WG, Moller W, Sommerer K, Larsson S, Svartengren M (2006). *Negligible clearance of ultrafine particles retained in healthy and affected human lungs*. **Eur Respir J** 28(2): 286-290.

Vila M, Portoles MT, Marques PA, Feito MJ, Matesanz MC, Ramirez-Santillan C, Goncalves G, Cruz SM, Nieto A, Vallet-Regi M (2012). *Cell uptake survey of pegylated nanographene oxide*. **Nanotechnology** 23(46): 465103.

Wilhelm C, Gazeau F, Roger J, Pons JN, Bacri JC (2002). *Interaction of anionic superparamagnetic nanoparticles with cells: Kinetic analyses of membrane adsorption and subsequent internalization*. **Langmuir** 18(21): 8148-8155.

Win KY, Feng SS (2005). *Effects of particle size and surface coating on cellular uptake of polymeric nanoparticles for oral delivery of anticancer drugs*. **Biomaterials** 26(15): 2713-2722.

Vlachou E, Chipp E, Shale E, Wilson YT, Papini R, Moiemen NS (2007). *The safety of nanocrystalline silver dressings on burns: A study of systemic silver absorption*. **Burns** 33(8): 979-985.

Wu J, Liu W, Xue C, Zhou S, Lan F, Bi L, Xu H, Yang X, Zeng FD (2009). *Toxicity and penetration of TiO2 nanoparticles in hairless mice and porcine skin after subchronic dermal exposure*. **Toxicol Lett** 191(1): 1-8.

Wu J, Wang C, Sun J, Xue Y (2011). *Neurotoxicity of silica nanoparticles: brain localization and dopaminergic neurons damage pathways*. **ACS Nano** 5(6): 4476-4489.

Wu X, Landfester K, Musyanovych A, Guy RH (2010). *Disposition of charged nanoparticles after their topical application to the skin*. **Skin Pharmacol Physiol** 23(3): 117-123.

Wu X, Price GJ, Guy RH (2009). *Disposition of Nanoparticles and an Associated Lipophilic Permeant following Topical Application to the Skin*. **Mol Pharm** 6(5): 1441-1448.

Xia XR, Monteiro-Riviere NA, Riviere JE (2010). *Skin penetration and kinetics of pristine fullerenes (C60) topically exposed in industrial organic solvents*. **Toxicol Appl Pharmacol** 242(1): 29-37.

Xie G, Wang C, Sun J, Zhong G (2011). *Tissue distribution and excretion of intravenously administered titanium dioxide nanoparticles*. **Toxicol Lett** 205(1): 55-61.

Xu A, Yao M, Xu G, Ying J, Ma W, Li B, Jin Y (2012). *A physical model for the size-dependent cellular uptake of nanoparticles modified with cationic surfactants*. **Int J Nanomed** 7: 3547-3554.

Yamago S, Tokuyama H, Nakamura E, Kikuchi K, Kananishi S, Sueki K, Nakahara H, Enomoto S, Ambe F (1995). *In vivo biological behavior of a water-miscible fullerene: 14C labeling, absorption, distribution, excretion and acute toxicity*. **Chem Biol** 2(6): 385-389.

Yang K, Gong H, Shi X, Wan J, Zhang Y, Liu Z (2013). *In vivo biodistribution and toxicology of functionalized nano-graphene oxide in mice after oral and intraperitoneal administration*. **Biomaterials** 34(11): 2787-2795.

Yang RS, Chang LW, Wu JP, Tsai MH, Wang HJ, Kuo YC, Yeh TK, Yang CS, Lin P (2007). *Persistent tissue kinetics and redistribution of nanoparticles, quantum dot 705, in mice: ICP-MS quantitative assessment*. **Environ Health Perspect** 115(9): 1339-1343.

Yu LE, Yung LYL, Ong CN, Tan YL, Balasubramaniam KS, Hartono D, Shui GH, Wenk MR, Ong WY (2007). *Translocation and effects of gold nanoparticles after inhalation exposure in rats*. **Nanotoxicology** 1(3): 235-242.

Yu SS, Lau CM, Thomas SN, Jerome WG, Maron DJ, Dickerson JH, Hubbell JA, Giorgio TD (2012). *Size- and charge-dependent non-specific uptake of PEGylated nanoparticles by macrophages*. **Int J Nanomed** 7: 799-813.

Zhang C, Qu G, Sun Y, Yang T, Yao Z, Shen W, Shen Z, Ding Q, Zhou H, Ping Q (2008). *Biological evaluation of N-octyl-O-sulfate chitosan as a new nano-carrier of intravenous drugs*. **Eur J Pharm Sci** 33(4-5): 415-423.

Zhang J, Li B, Zhang Y, Li A, Yu X, Huang Q, Fan C, Cai X (2013). *Synchrotron radiation X-ray fluorescence analysis of biodistribution and pulmonary toxicity of nanoscale titanium dioxide in mice*. **Analyst** 138(21): 6511-6516.

Zhang L, Bai R, Li B, Ge C, Du J, Liu Y, Le Guyader L, Zhao Y, Wu Y, He S, Ma Y, Chen C (2011). *Rutile TiO(2) particles exert size and surface coating dependent retention and lesions on the murine brain*. **Toxicol Lett** 207(1): 73-81.

Zhang L, Bai R, Liu Y, Meng L, Li B, Wang L, Xu L, Le Guyader L, Chen C (2012). *The dose-dependent toxicological effects and potential perturbation on the neurotransmitter secretion in brain following intranasal instillation of copper nanoparticles*. **Nanotoxicology** 6(5): 562-575.

Zhang LW, Monteiro-Riviere NA (2008). *Assessment of quantum dot penetration into intact, tape-stripped, abraded and flexed rat skin*. **Skin Pharmacol Physiol** 21(3): 166-180.

Zhang LW, Yu WW, Colvin VL, Monteiro-Riviere NA (2008). *Biological interactions of quantum dot nanoparticles in skin and in human epidermal keratinocytes*. **Toxicol Appl Pharmacol** 228(2): 200-211.

Zhang M, Tahara Y, Yang M, Zhou X, Iijima S, Yudasaka M (2014). *Quantification of whole body and excreted carbon nanohorns intravenously injected into mice*. **Adv Healthc Mater** 3(2): 239-244.

Zhang Y, Hong G, He W, Zhou K, Yang K, Li F, Chen G, Liu Z, Dai H, Wang Q (2013). *Biodistribution, pharmacokinetics and toxicology of Ag2S near-infrared quantum dots in mice*. **Biomaterials** 34(14): 3639-3646.

Zhu Y, Choe CS, Ahlberg S, Meinke MC, Alexiev U, Lademann J, Darvin ME (2015). *Penetration of silver nanoparticles into porcine skin ex vivo using fluorescence lifetime imaging microscopy, Raman microscopy, and surface-enhanced Raman scattering microscopy*. **J Biomed Opt** 20(5): 051006.

Zvyagin AV, Zhao X, Gierden A, Sanchez W, Ross JA, Roberts MS (2008). *Imaging of zinc oxide nanoparticle penetration in human skin in vitro and in vivo*. **J Biomed Opt** 13(6): 064031.

KEMI
Swedish Chemicals Agency

Box 2, SE-172 13 Sundbyberg
+46 8 519 41 100

Visitors' and delivery address
Esplanaden 3A, Sundbyberg

kemi@kemi.se
www.kemikalieinspektionen.se